

Modular Program Development
For Vehicle Crash Simulation,
Vol. 1: Summary Report, Test Results
and Theory

Prepared By:

I. K. McIvor
W. J. Anderson
A. S. Wineman

Of:

College of Engineering
The University of Michigan
Ann Arbor, Michigan 48109

For:

National Highway Traffic Safety Administration
U.S. Department of Transportation
Trans Point Building
2100 Second Street S.W.
Washington, D.C., 20590

Under:

Contract No. DOT-HS-4-00855

November 30, 1976

1. Report No.		2. Government Accession No.		3. Recipient's Catalog No.	
4. Title and Subtitle Modular Program Development for Vehicle Crash Simulation, Vol. 1: Summary Report, Test Results, and Theory				5. Report Date	
7. Author(s) I. K. McIvor, W. J. Anderson, A.S. Wineman				6. Performing Organization Code	
9. Performing Organization Name and Address The University of Michigan Ann Arbor, Michigan 48109				8. Performing Organization Report No. UM-HSRI-76-4-1	
12. Sponsoring Agency Name and Address National Highway Traffic Safety Admini- stration - U.S. Department of Transpor- tation - Trans Point Bldg Washington, D.C. 20590				10. Work Unit No. (TRIS)	
				11. Contract or Grant No. DOT-HS-4-00855	
15. Supplementary Notes				13. Type of Report and Period Covered Final Report March, 1974-Nov. 1976	
				14. Sponsoring Agency Code	
16. Abstract This report is the first of three volumes of the final report on the project "Modular Program for Vehicle Crash Simulation." The objective of the project was to develop a computer simulation for vehicle structures under general crash conditions. The program has an user oriented modular structure designed for maximum flexibility in the synthesis of vehicle models. This volume contains: <ol style="list-style-type: none"> 1. Recommendations for Future Development of Vehicle Simulations, 2. A Description of the General Program Structure, Modeling Capability, and Solution Procedure for the Simulation Program UMVCS-1, 3. The Experimental and Predicted Results for Static and Dynamic Validation Tests, 4. A Modeling Study of an Actual Vehicle Dynamic Frame Test 5. The Analytical Studies on Which the Modeling Elements of UMVCS-1 are Based. 					
17. Key Words			18. Distribution Statement		
19. Security Classif. (of this report)		20. Security Classif. (of this page)		21. No. of Pages	22. Price

The opinions, findings, and conclusions expressed in this publication are those of the authors and not necessarily those of the National Highway Traffic Safety Administration.

Acknowledgments

The authors gratefully acknowledge the contributions of the Contract Technical Manager, Mr. James Hackney. His cooperation and advice were very helpful. We would also like to thank Mr. William Liu and Mr. Tom Hollowell for their interest in the project.

Final Report

Contract No. DOT-HS-4-00855

Modular Program Development for Vehicle Crash Simulation: Vol. 1 - Summary Report, Test Results, and Theory

Table of Contents

Chapter 1: Summary and Recommendations

- 1.1 Introduction
- 1.2 Summary of Results
- 1.3 Recommendations

Chapter 2: University of Michigan Vehicle Crash Simulation

- 2.1 General Description of Program
- 2.2 Simulation Procedure
- 2.3 Numerical Integration Procedure

Chapter 3: Static Validation Tests

- 3.1 Introduction
- 3.2 Combined Loading Hinge Validation Test
- 3.3 Static Crush of Space Frame

Chapter 4: Dynamic Validation Tests

- 4.1 Introduction
- 4.2 Test Procedure
- 4.3 Comparison of Simulation
and Experimental Results
- 4.4 Discussion

Chapter 5: Modeling Study of Dynamic Frame Test

- 5.1 Introduction
- 5.2 Simulation Model
- 5.3 Comparison of Simulation & Test Results

Appendix A: A Structural Theory for the Large
Plastic Deformation of Beams

- A.1 Introduction
- A.2 Notation
- A.3 Kinematics of Deformation
- A.4 Equilibrium
- A.5 Constitutive Equations for Generalized
Plastic Hinges
- A.6 Elastic Deformation Rate Equations
- A.7 Element Stiffness Matrix
- A.8 Global Equations
- A.9 Summary of Equations

Appendix B: Incremental Equations for Rigid Body
Component

- B.1 Introduction
- B.2 Linear Momentum
- B.3 Angular Momentum
- B.4 Incremental Equations of Motion

Appendix C: Mechanism Stiffness Matrices

- C.1 Introduction
- C.2 Extensional Spring
- C.3 Torsional Spring
- C.4 Bending Connector
- C.5 Shear Connector
- C.6 Connection to Rigid Body Nodes
- C.7 Superposition of Mechanisms

Appendix D: Plastic Hinge Tests

- D.1 Experimental Hinge Tests
- D.2 Test Results
- D.3 Hinge Constitutive Parameters

List of Figures

1. UMVCS-1 General Program Structure
2. Combined Loading Experiment
3. Initial Geometry - Combined Loading Experiment
4. Computed and Experimental Force Deformation Curve
5. Final Deformed Shape - Combined Loading Experiment
6. Space Frame Before Deformation
7. Space Frame After Deformation
8. Frame Model
9. Experimental and Computed Force Deformation Curve
10. Experimental Transverse vs. Longitudinal Displacement
11. Scale Model Mounted on Mini-Sled
12. Schematic of Impact Test
13. Model Orientation for Symmetric and Unsymmetric Tests
14. Simulation Model
15. Final Deformed Shape
Symmetric Test
16. Final Deformed Shape
Unsymmetric Test
17. Barrier Force
Symmetric Test
18. Barrier Force
Unsymmetric Test
19. Top Plate Acceleration
Symmetric Test
20. Bottom Plate Acceleration
Symmetric Test
21. Top Plate Acceleration
Unsymmetric Test

List of Figures
(Continued)

22. Bottom Plate Acceleration
Unsymmetric Test
23. Comparison of Frequency Resolution
for Different Time Steps
24. Schematic of Dynamic Frame Test
25. Simulation Model
26. Bumper Support Static Crush Test
27. Barrier Force and Vehicle Acceleration
28. Vehicle Velocity
29. Vehicle Velocity for First 40 ms.
30. Vehicle Acceleration for First 40 ms.
31. Acceleration with Elastic Component
- A.1 Kinematics of Deformation
- D.1 Tensile Test for 1"x1"x0.075" Tubing
- D.2 Plastic Hinge Rotation - Pure Bending
- D.3 Hinge Deformation - Pure Bending
- D.4 Plastic Hinge Rotation - Torsion
- D.5 Computed and Experimental Plastic Hinge
Rotation in Bending
- D.6 Computed and Experimental Plastic Hinge
Rotation in Torsion

List of Tables

1. Data Input Levels
 2. Available Modeling Elements
 3. Beam and Hinge Properties
- D.1 Hinge Parameters for Square Tubing

1. Summary and Recommendations

1.1 Introduction

The objective of this project was to develop a computer simulation program for vehicle impact meeting the following criteria:

1. Ability to compute three dimensional structural response under general crash conditions.
2. Flexibility for user to specify arbitrary structural configurations using modeling elements appropriate for realistic vehicle structures.
3. Modular structure for input data representing actual sub-assemblies of the vehicle.
4. Prediction of appropriate crashworthiness variables including energy dissipation, impact forces, relative displacement of components, and acceleration and velocity time histories of all significant points.
5. Cost effective numerical integration procedure.

The activities undertaken to accomplish this objective can be grouped into three major categories. They are:

- (i) the theoretical development of modeling elements for the large plastic deformation of structures.
- (ii) the development and programming of the computer simulation.
- (iii) an experimental program including validation tests of the basic theory, dynamic impact tests for validation of the computer simulation, and a test program to obtain data for modeling the large deformation of plastic hinges.

The Final Report describing these activities is organized into three separate volumes. They are:

Vol. 1: Summary Report, Test Results and Theory

Vol. 2: Plastic Hinge Experiments

Vol. 3: User's Guide - University of Michigan Vehicle
Crash Simulation - Version 1

In the next section a summary of the major results of the project is given followed by our recommendations for future investigations. Chapter 2 presents a description of the structure and modeling capabilities of the computer simulation program. It includes a discussion of the overall simulation procedure and the numerical integration method employed in the program. Chapter 3-5 contain a discussion of the various validation tests and comparison of the results with simulation predictions. In addition to demonstrating the predictive ability of the simulation, the discussion also illustrates the range of modeling capabilities. Results for static tests involving combined loading and crush of space frames are given in Chapter 3. The results of the dynamic validation tests conducted on the HSRI Impact Sled are given in Chapter 4. Chapter 5 presents the results of a modeling study for a dynamic frame test conducted by Dynamic Science on a '68 Plymouth Fury. Finally the major analytical results obtained during the contract are presented in the Appendices.

1.2 Summary of Results

The major results and conclusions of the project are:

A. Analytical Studies

1. A new structural theory for dynamic large plastic deformations of three dimensional frame structures was derived. The theory is based on the generalization of the concept of a plastic hinge.
2. As part of this analysis a nonlinear constitutive theory for generalized plastic hinges was developed which includes the effect of localized deformation. The theory requires constitutive data from standardized tests. Such data has been obtained for box and channel sections over a range of sizes appropriate for vehicle structures.
3. An incremental form of the equations of motion for general rigid bodies has been derived. The formulation permits interaction of the rigid body with structural elements at an arbitrary number and location of points on the body.
4. The concept of generalized springs used in one dimensional mechanical simulations has been extended to three dimensions. Incremental stiffness matrices have been derived for a variety of mechanisms

transmitting vector force and moment couples. Each mechanism is characterized by a "load-stroke" curve which may be arbitrarily specified. These mechanisms provide modeling elements for non-frame components of the vehicle. They may also be used for modeling a variety of connections between components.

Details of the above analytical studies are given in Appendices A, B, C.

B. Simulation Program

1. Based on the above studies a computer program has been developed satisfying the basic objective of the project. This program, University of Michigan Vehicle Crash Simulation (UMVCS-1), is an operating version which meets the criteria specified above. A description of the program structure, details of the numerical integration procedure, and a discussion of cost effectiveness is given in Chapter 2. A complete User's Guide including a detailed example problem is contained in Volume 3.
2. The Executive System of UMVCS-1 has an open-end design, i.e. additional modeling elements (mechanisms) can be added without any structural changes in the simulation program.

C. Validation Studies

1. Two dynamic validation tests involving symmetric and unsymmetric configurations were conducted on the HSRI Impact Sled. The structure was a combination of a space frame and rigid body masses similar to those used in previous scale modeling vehicle impact tests. The results validated the predictive capability of the simulation program for such structures under conditions characteristic of vehicle impact. Details of the test and comparison with predicted results are given in Chapter 4.
2. A modeling study of a dynamic frame test conducted by Dynamic Science on a '68 Plymouth Fury was carried out. The study did not rigorously demonstrate the predictive validity of the simulation since much of the input data and interpretation of the test conditions were speculative. Nevertheless sufficiently good agreement was obtained on the basis of reasonable assumptions to demonstrate the applicability of the simulation to actual vehicle structures. Details of the study are given in Chapter 5.

D. Constitutive Tests to Obtain Hinge Properties

1. Biaxial bending, torsion, and axial tests were performed on 10 different box and 14 different channel sections. Section sizes and material properties

span the range of interest in vehicle structures. Test results are presented as force-deformation (moment-rotation) curves.

2. The constitutive parameters for the plastic hinge theory were obtained from an analysis of the data for each test.
3. This set of test parameters was used to establish scaling laws for computing the constitutive parameters for other box and channel sections. Dimensional analysis was used to obtain the analytical form of the scaling law. Numerical coefficients were determined by least square fit of the test data.

A description of the hinge properties tests and the detailed experimental results are given in Volume 2.

1.3 Recommendations

A. Program Improvements

1. The basic mechanism algorithm needs to be generalized to include unsymmetric behavior, i.e. different characteristic curve in tension and compression, and unloading hysteresis behavior. Also the present version of the simulation program does not explicitly compute the energy dissipation in mechanisms.
2. In the present version all input data must be specified with respect to the global initial reference frame.

For convenience in data preparation the program should be modified to accept data in a modular reference frame. Also the output processor should be modified to permit user specification of reference frame for output quantities.

3. The versatility of the program could be increased by the development and incorporation of additional mechanisms. In particular there is a need for "friction mechanisms" for use in regions of contact, and "hydraulic mechanisms" for modeling components where force transmission depends upon the deformation rates.
4. The current version has no provision to account for fracture. Procedures for incorporating jump discontinuities in forces should be included in the program.
5. Data input could be simplified by the addition of default modes and the internal calculation of some direction cosine matrices now required as input.

B. Numerical Integration Studies

As discussed in detail in the next Chapter, UMVCS-1 employs a variable step implicit integration procedure. The acceleration increment is approximated by backward differences. Current step size is chosen on the basis

of the yield function error in the previous step. Our results demonstrate that the procedure is efficient and sufficiently accurate for the applications of interest. Nevertheless there is a need for additional numerical studies to establish the optional integration strategy. Two suggested studies are:

1. Step size is controlled by user specified upper and lower bounds on the incremental yield function error. In general wide bounds increase step size and efficiency at the sacrifice of accuracy. There is a need for numerical studies to determine in detail the accuracy-efficiency tradeoff as a function of error bounds.
2. The backward difference approximation for the acceleration increment was chosen because of previous studies indicating its stability properties in plasticity applications. There may be, however, more accurate representations which would retain the essential stable character. Thus an optimal integration study requires some comparative studies between results obtained with different acceleration approximations.

C. Modeling Studies and Additional Research

The simulation program UMVCS-1 is a special purpose program since the available modeling elements and modular

input structure are directed specifically towards vehicle impact. In many respects, however, it provides the user with the generality associated with more conventional finite element programs. The flexibility of the program permits the user to employ the available structural elements to model specific vehicle sub-assemblies in a variety of ways appropriate to the particular problem under consideration. The physical validity of the results is of course dependent upon the appropriateness of the assumed model.

Under the present contract we have gained considerable experience in modeling frame type components of the vehicle, but only limited experience in employing three dimensional mechanisms for modeling non-frame components. Thus we recommend that the simulation be employed in a variety of modeling and sensitivity studies. In particular these studies should include:

1. Crash configurations involving interaction between frame and non-frame components.
2. Crash configurations (e.g. side impact) for which the passenger compartment should be modeled as a deformable body.
3. Vehicle to vehicle impact involving relative motion of the impact point.

It is expected that such studies would both identify new mechanisms to be incorporated in the simulation and develop a methodology for determining mechanism parameters from more detailed studies of specific components.

2. University of Michigan Vehicle Crash Simulation

2.1 General Description of Program

The program UMVCS-1 is designed to facilitate the synthesis of vehicle structures from a variety of modeling concepts. Within the context of a single program it allows the creation of essentially different vehicle models that are appropriate for a particular crash situation or design purpose. This flexibility is achieved through a modular concept. The program views the vehicle as a collection of modules, each representing a particular physical sub-assembly such as passenger compartment, stub frame, drive-train, suspension system, etc. The user may specify each module independently both in modeling concept and detailed numerical description. Any number of modules may be employed in a given simulation. Moreover a particular sub-assembly may be characterized differently in different applications. For example the passenger compartment may be modeled as a rigid body in one simulation and a deformable frame in another. The user need only change the input data for the particular module. It should be noted that storage requirements, internal designation of variables, and dimensioning are all handled automatically within the program. Thus the user may use any number and type of modules without specifying any additional information or making any changes in program instructions.

Input to the program is organized in three levels as summarized in Table 1. Each module is specified in terms of structural components and the connections between components. In the present

Table 1: Data Input Levels

Vehicle:	Position and Orientation Connections Between Modules
Module:	Position and Orientation Connections Between Components Within Module
Component:	Position and Orientation Component Parameter Specifications Nodal Location and Parameter Specification Element Orientation and Parameter Specification

version of the program components may be either a general deformable frame or a rigid body. The frame components are defined by a set of nodal points connected by elements which are described in more detail in the next section. Connections between components or modules may either be idealized connectors like ball and socket and rigid joints or by any of the deformable elements employed in components. At each level of input the description is in terms of user specified alphanumeric names which need only be unique within a given level. Thus the input format is directed toward model synthesis. The resulting data set is essentially a literal physical description of the vehicle.

The program structure which implements the above concepts consists of two main processors. These are illustrated schematically in Fig. 1. The Input Processor transforms the input data set into a binary data file for the Computation Processor. In the process storage requirements are computed and storage tables established. An identification index variable is established which locates all variables required in the Computation Processor. Finally the Input Processor writes a dummy main program with the correct dimension statements for exercising the computation phase. A complete description of the program and an example of the modular input is given in Vol. 3.

2.2 Simulation Procedure

As indicated above two component types are available in the present version of the program. The rigid body component is used

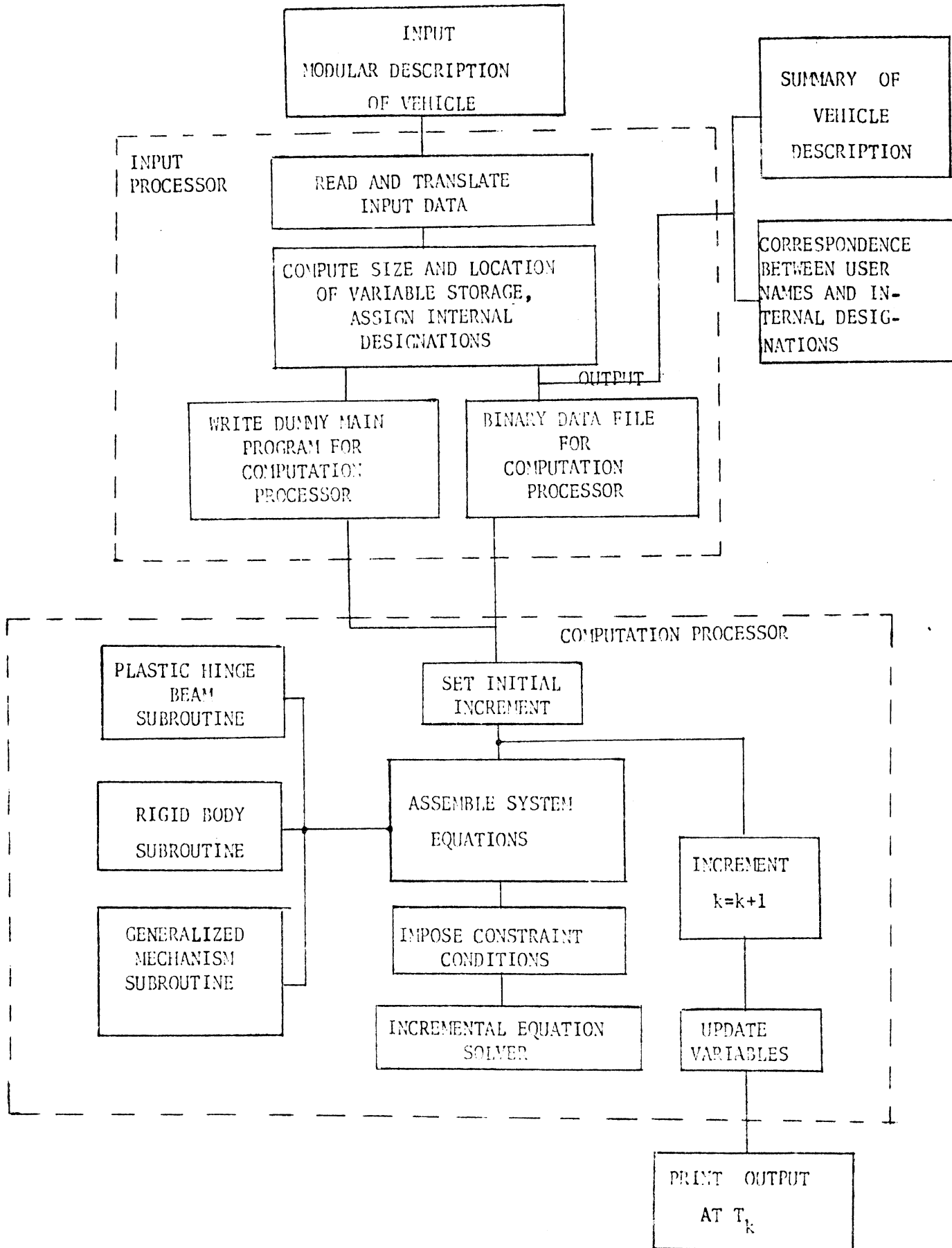


Fig. 1 UMVCS-1 General Program Structure

to model masses whose finite dimensions and rotational inertia cannot be neglected. This component permits the mass to interact with other structural components at any number of nodes arbitrarily located on the mass.

The deformable frame component may consist of an arbitrary number of elements connected at node points. Three translational and three rotational degrees of freedom are associated with each node. The modeling elements available for use in frame components are summarized in Table 2.

The basic beam element is based on a structural plasticity theory which generalizes the concept of a plastic hinge to large three dimensional rotations. This theory is given in detail in Appendix A. The theory accounts for local deformation at the hinge. The remaining elements are three dimensional extensions of the nonlinear "resistances" used in one dimensional crash simulations. Each mechanism is characterized by a "force" curve (or curves) which may be arbitrarily specified in tabular form as a function of an appropriate kinematic variable. When the four elements of this type are used together, they transmit a force and couple vector characterized by six "force-deformation" curves.

For both the beam element and generalized mechanisms we have in incremental form

$$\begin{bmatrix} \Delta R^i \\ \Delta \tilde{R}^j \\ \Delta \tilde{R}^j \end{bmatrix}_{k+1} = KE(t_k) \begin{bmatrix} \Delta D^i \\ \Delta \tilde{D}^j \\ \Delta \tilde{D}^j \end{bmatrix}_{k+1} \quad (1)$$

where i and j denote the node points connected by the element, \tilde{R} is

Table 2: Available Modeling Elements

<u>Element</u>	<u>Type</u>	<u>Specification</u>
Plastic Hinge Beam	Finite Element	Beam and Hinge Properties
Extensional Spring	Generalized Mechanism	Tabular Force Deformation Curve
Shear Connector	Generalized Mechanism	Two Tabular Force Deformation Curves
Bending Connector	Generalized Mechanism	Two Tabular Force Deformation Curves
Torsional Spring	Generalized Mechanism	Tabular Force Deformation Curve

the generalized force vector (three force and three couple components), and \tilde{D} is the generalized nodal displacements. The element stiffness matrix depends upon the current state. The derivation of KE for a beam element may be found in Appendix A. The results for the generalized mechanisms are given in Appendix C. The notation $\Delta\tilde{U}_{k+1}$ denotes

$$\Delta\tilde{U}_{k+1} = \tilde{U}(t_{k+1}) - \tilde{U}(t_k) \quad (2)$$

The first step in assembling the system equations is done by the Input Processor. It identifies all frame components and sequentially assigns internal node numbers. Likewise it identifies all rigid body components and sequentially assigns a rigid body identification number. Thus the input data specified by the user in terms of a physical description of the vehicle model is translated to a data set for a single frame module and several rigid bodies. In terms of this description the Input Processor sets up connector arrays which identifies the type of connector (beam element, mechanism, or ideal connector) between each frame and rigid body node.

With the input in this format the Computation Processor assembles the system matrices from the nodal and rigid body equations of motion. The equations of motion for the i th frame node are in incremental form

$$M^i \ddot{\Delta\tilde{D}}_{k+1}^i = -\sum_{m=1}^{n^i} (\Delta\tilde{R}_{k+1}^i)_m + \Delta\tilde{F}_{k+1}^i \quad (3)$$

where D^i are the generalized nodal displacements of the i th node and M^i is the nodal mass matrix. The summation on the right hand side denotes the sum of internal connector force increments, and $\Delta \tilde{F}_{k+1}^i$ is the increment in external force. The external forces are specified by the user in tabular form. The program computes the appropriate increment at each time step.

In incremental form the rigid body equations of motion have the form (see Appendix B)

$$M^R \ddot{\Delta \tilde{D}}_{k+1}^R + C^R \dot{\Delta \tilde{D}}_{k+1}^R + K^R \Delta \tilde{D}_{k+1}^R = \sum_{m=1}^N T_m \left(\Delta \tilde{F}_{k+1}^m - \Delta \tilde{R}_{k+1}^m \right) \quad (4)$$

where $\Delta \tilde{D}^R$ denotes the displacement increments of the center of gravity and the rigid body rotation increments, \tilde{F}^m are the external generalized forces (force and couple) acting on the rigid body nodes, R^m are the connector forces, and T_m are appropriate transformation matrices depending on the location of the node relative to the rigid body c.g.

Eq. (1) is used to eliminate the internal forces from (3) and (4). If a node is a rigid body node, the corresponding generalized displacement increment on the right hand side of (1) is expressed in terms of $\Delta \tilde{D}^R$ through an approximate transformation matrix. For ideal connectors the unknown connector force is eliminated between the appropriate i th and j th node equations. The i th equations are then replaced by the constraint conditions

implied by the connector (for example $\Delta \tilde{D}^i - \Delta \tilde{D}^j = 0$ for a rigid connector). The resulting global equations have the form

$$M \ddot{\tilde{U}}_{k+1} + C \dot{\tilde{U}}_{k+1} + K \tilde{U}_{k+1} = \Delta \tilde{F}_{k+1} \quad (5)$$

where the coefficient matrices are functions of the current state and $\Delta \tilde{F}$ is a known vector.

Displacement boundary conditions or imposed displacements are treated by contraction of the matrix equations. In UMVCS-1 the displacement time history of a node may be specified arbitrarily in tabular form. In addition nodes may be stopped in a specified time or stopping distance. The stopping distance may be either with respect to the inertial frame or relative to a second node. Details are given in Vol. 3. An example of the use of such conditions is described in Chapter 5. After contraction the system equation retain the form (5), the right hand side now containing the imposed displacement increments as well as the increments in external forces.

2.3 Numerical Integration Procedure

To integrate (5), the acceleration and velocity increments are replaced by the backward differences

$$\dot{\tilde{U}}_{k+1} = (\Delta t_{k+1})^{-1} \Delta \tilde{U}_{k+1} - (\Delta t_k)^{-1} \Delta \tilde{U}_k \quad (6)$$

$$\ddot{\tilde{U}}_{k+1} = h_1 \Delta \tilde{U}_{k+1} - h_2 \Delta \tilde{U}_k + h_3 \Delta \tilde{U}_{k-1}$$

where Δt_{k+1} denotes $(t_{k+1} - t_k)$ and

$$h_1 = (\Delta t_{k+1})^{-2}, \quad h_2 = (\Delta t_k + \Delta t_{k+1})(\Delta t_{k+1} \Delta t_k^2)^{-1} \quad (7)$$

$$h_3 = (\Delta t_k \Delta t_{k-1})^{-1}$$

Introducing (7) into (5) gives

$$H \Delta U_{\sim k+1} = P_{\sim} \quad (8)$$

where

$$H = \left[h_1 M + (\Delta t_{k+1})^{-1} C + K \right] \quad (9)$$

$$P_{\sim} = \left[h_2 M + (\Delta t_k)^{-1} C \right] \Delta U_{\sim k} - h_3 M \Delta U_{\sim k-1} + \Delta F_{\sim k+1}$$

Eq. 8 is solved by a modified Gaussian elimination procedure.

There are a number of reasons for this particular choice of integration procedure. For linear operators backward differences are inherently stable. From our experience it appears that they are also stable for the nonlinear problem of interest here. Numerical stability is an essential requirement in the modeling of vehicle crash. In structural crashworthiness applications the dynamic plastic collapse is of prime interest. The inherent time scale of this phenomenon is generally much longer than the time scale of elastic wave propagation and high frequency oscillations. For efficient integration we would like to choose a time step which suppresses these effects. In general this is possible only if stability is not an issue.

The use of variable step size is also important in the present application. The form of the element stiffness matrix

depends upon whether a plastic hinge has formed at one or both of the element boundaries. An inherent difficulty with the plastic hinge concept is that a given increment may cause the solution to "overshoot" the generalized yield function which governs the hinge behavior. Since the yield function depends nonlinearly on the increment, an iterative scaling procedure is required for which the variable step form is convenient.

The variable step procedure is also a major factor in integration efficiency. We have found that during the initial stage of motion, which is the period of active hinge formation, relatively small time steps are required. Once a collapse mode has formed, however, the response may be followed employing much larger steps. The error measure used to control step size in the present program is the incremental change in the yield function. Denoting the yield function by f , the exact solution satisfies

$$\dot{f} = 0 \quad (10)$$

We define

$$\epsilon = |f(t_k) - f(t_{k-1})| \quad (11)$$

If ϵ exceeds a specified upper bound, the time increment for the next step is reduced. Conversely if ϵ is less than a specified lower bound, the step size is increased. In addition a maximum step size is imposed which insures that the rotation increments are sufficiently small for accurate updating of the deformed geometry.

The simulations discussed in the next three Chapters illustrate the use of this procedure and demonstrate its characteristic features with respect to efficiency and accuracy.

3. Static Validation Tests

3.1 Introduction

One of the advantages of the present formulation is its direct applicability to static crush problems. A static solution is obtained by setting all mass terms to zero. In this case time is simply a parameter which is used to specify the increment in external force or imposed displacement. In this Chapter we compare experimental and predicted results for two static tests. The first is a combined bending-torsion test of a single beam specimen. The test was designed as a preliminary validation of the plastic hinge theory including the effects of local deformation.* The second test is the static crush of a frame structure.

The frame elements for both tests were 1"x1"x.075" 1040 mechanical steel tubing. Tensile test data (see Appendix D) indicated the material could be considered as an elastic-perfectly plastic with an elastic modulus of 20×10^6 psi and a yield stress of 61,500 psi. The required plastic hinge properties were obtained from the tests described in Appendix D.

* Additional combined loading tests are described in Volume 2 in connection with the determination of hinge properties for a variety of cross section shapes.

3.2 Combined Loading Hinge Validation Test

The test configuration for the combined load test is shown in Fig. 2. It consists of a double cantilever specimen, each specimen 5.5 inches in length. The ends of the cantilevers are attached to rigid bars at right angles. The system is loaded through high strength cables and a system of universal joints that approximate a ball and socket joint. Symmetry insures a zero slope at the root of the cantilever. The initial geometry is shown in Figure 3.

The cable used in loading was standard 1/8 inch diameter stranded cable commonly used in aircraft control systems with breaking strength of 2000 lbs. The cable was loaded and unloaded seven times in order to align the fibers in the most inextensible position. After five cycles the load displacement curve was repeatable with a stiffness of 5,830 #/in.

Test results are shown in Figure 4 as the vertical force component in the cable versus the vertical displacement of the upper end of the cable. At low loads the system is elastic. A hinge then forms at the root of the cantilever under essentially combined bending and torsion. Torsional rotation dominated early in the hinging action with bending becoming more pronounced with increasing deformation. At very large displacements the load becomes more aligned with the tube axis accounting for the rapid hardening of the system for displacements greater than five inches. Throughout the test, changes in geometry tend to harden the system. Over most of the test this is counteracted

by the decrease in the load carrying capacity of the hinge. The final deformed shape is shown in Figure 5. The rotation in both bending and torsion exceeded 45 degrees.

The computed force-deformation curve is compared with the test result in Figure 4. Agreement is good over the entire deformation range.

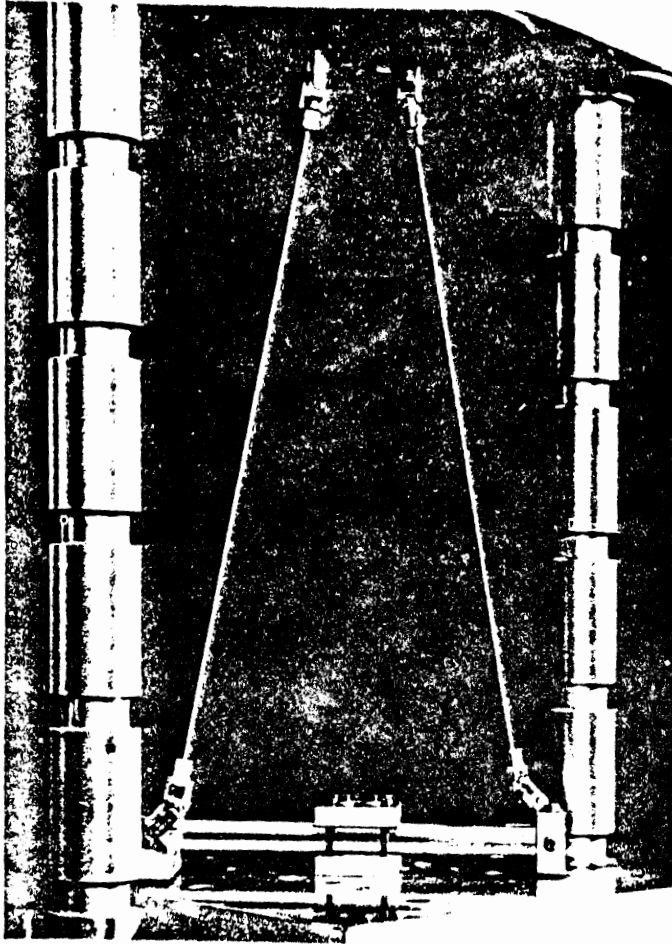


FIG. 2 COMBINED LOADING EXPERIMENT

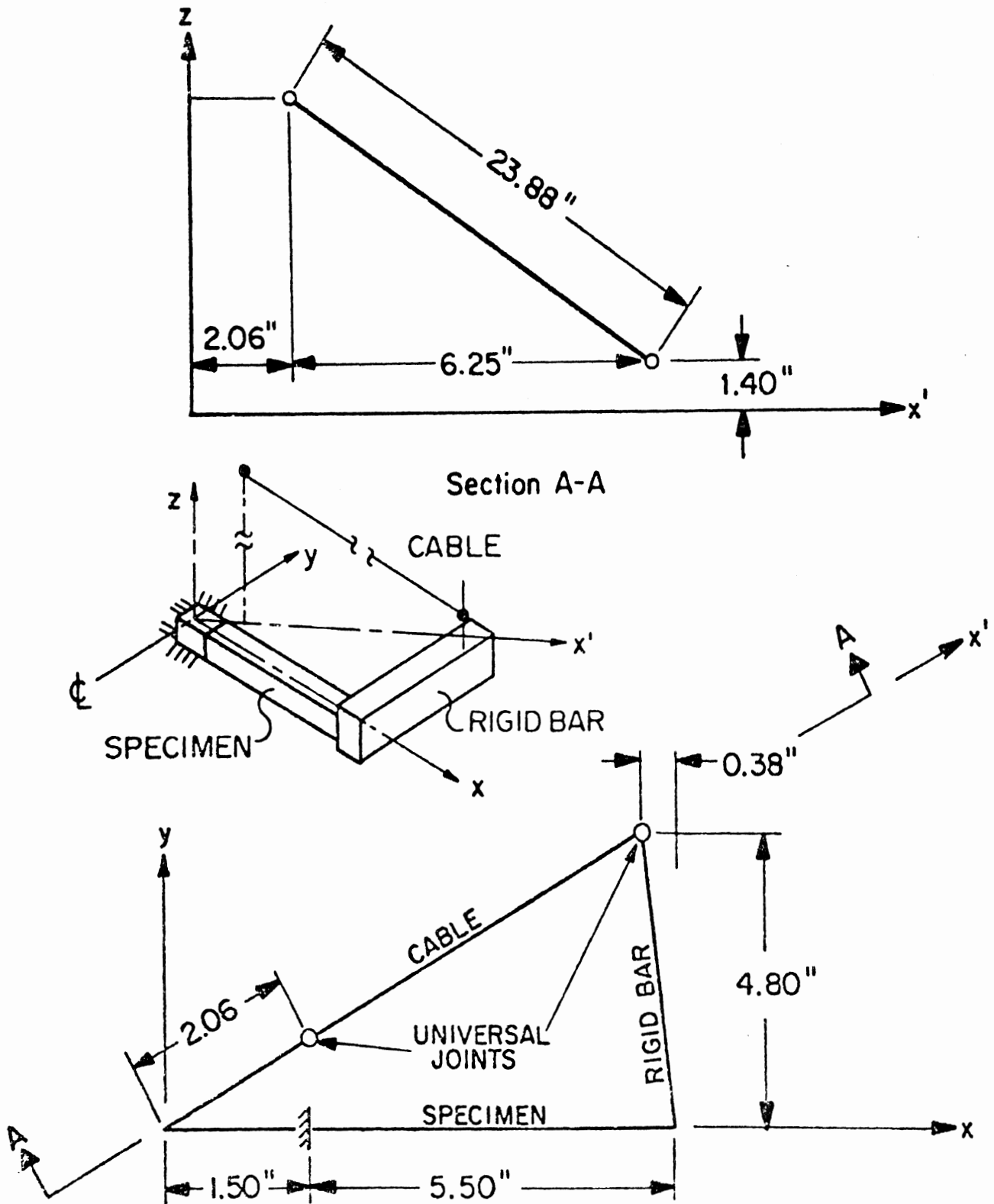


FIG. 3 INITIAL GEOMETRY-COMBINED LOADING EXPERIMENT

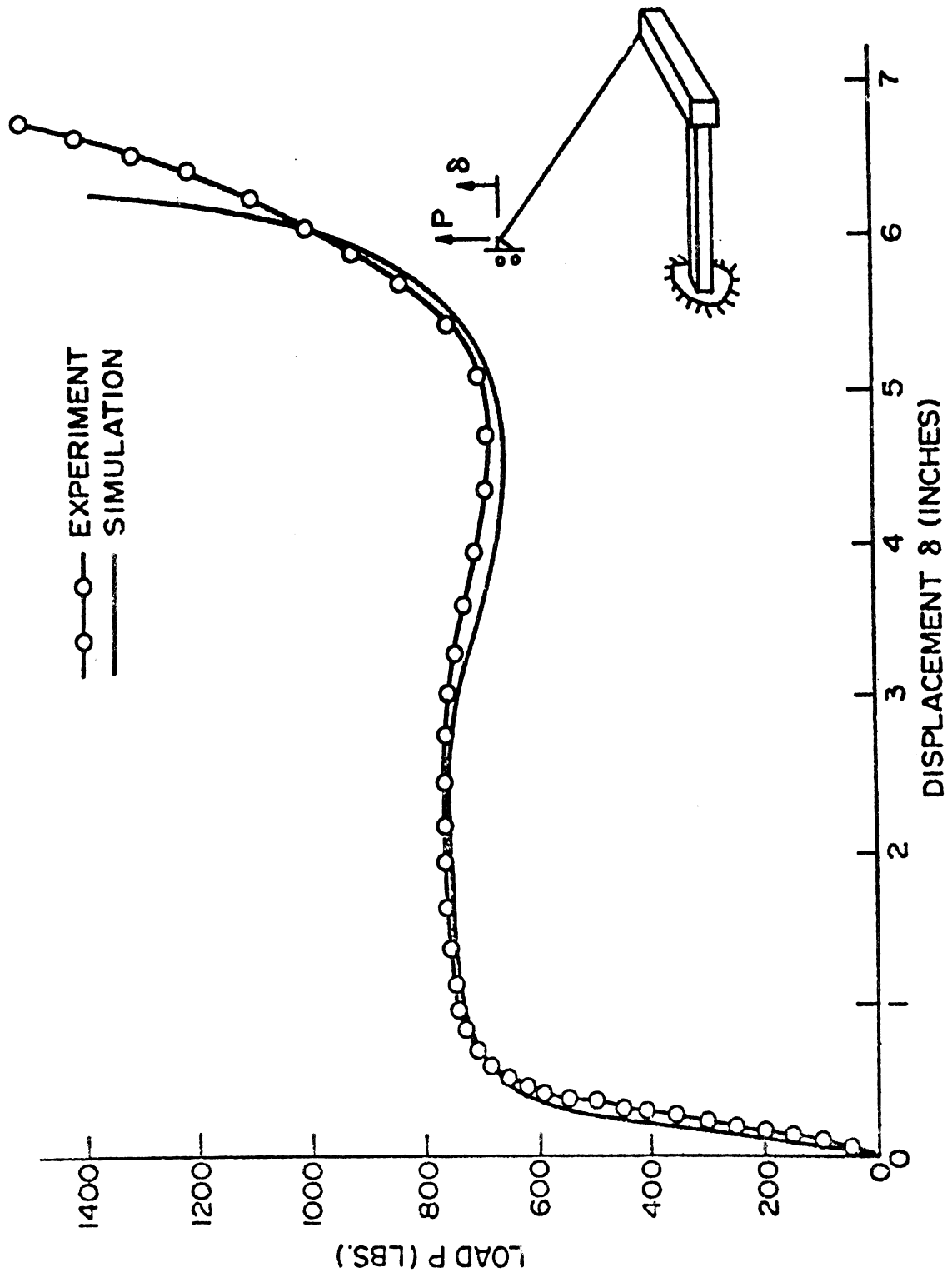


FIG. 4 COMPUTED AND EXPERIMENTAL FORCE DEFORMATION CURVE

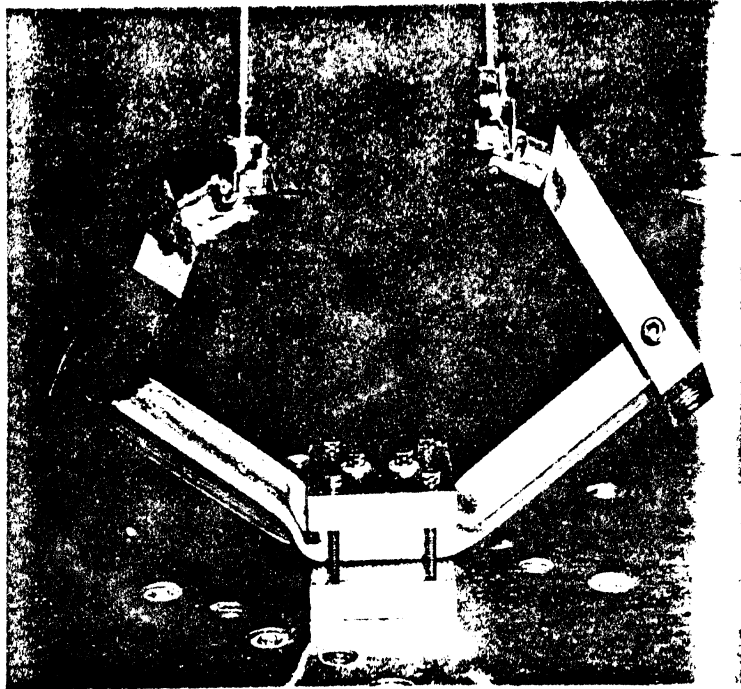


FIG. 5 FINAL DEFORMED SHAPE-COMBINED LOADING EXPERIMENT

3.3 Static Crush of Space Frame

The welded space frame is shown in Fig. 6. It consists of a forestructure welded to a rigid plate which is connected to a second plate through a rear structure. The rear plate was clamped to the bed of the testing machine, and the frame was moved in the negative X_2 direction (see Fig. 8) against a rigid pole indenter. The rear structure remained elastic, but the forestructure was crushed longitudinal about 4.8 inches which is over 50% of the original forestructure dimensions. The final deformed configuration is shown in Fig.7.

The model employed for the computer simulation is shown in Fig. 8. It consists of 15 nodes, 12 beam elements and 2 rigid plate elements. Beam properties were computed from cross sectional dimensions.

The experimental force-deformation curve is given by the circled points in Fig. 9. The anomalous behavior of the test in the region of maximum load is best explained by Fig. 10 which shows the transverse displacement of the contact node U_1 versus the longitudinal displacement U_2 . Initially the transverse displacement was evidently constrained. A sudden slipping of the contact node along the indenter occurred at about 3/4 inches of longitudinal displacement. This sudden slip is accompanied by a sharp drop in load. The transverse displacement then increases monotonically as the deformation proceeds. It should be noted that the experimental transverse displacement is subject to a fairly large relative error. Due to severe local deformation at the

contact node, accurate measurement of the nodal displacement was difficult.

It is clear that the test boundary conditions at the contact node are complex. To examine the effect of boundary conditions, preliminary computations were made for two different cases:

(i) Transverse Force $F_1 = 0$

(ii) Transverse Displacement $U_1 = 0$

In both cases the contact node was assumed free to rotate. The computed results for the first two inches of crush are shown in Fig. 9. As anticipated these limiting cases bracket the experimental result.

As a more severe test of the theory, a third case was considered in which the transverse displacement U_1 was specified by the piece-wise linear approximation to the experimentally observed curve shown in Fig. 10. It was again assumed that the contact node was free to rotate. The predicted force-deformation curve is shown as the dashed curve in Fig. 9. The most pronounced discrepancy is that the computed result shows a greater softening rate for displacements in the range of 1.5 to 2.5 inches. In general, however, the overall agreement is good.

Computations were carried out on The University of Michigan IBM 370/74 computer. The 4.8 inches of crush required 125 steps. Total CPU time was 87 seconds.

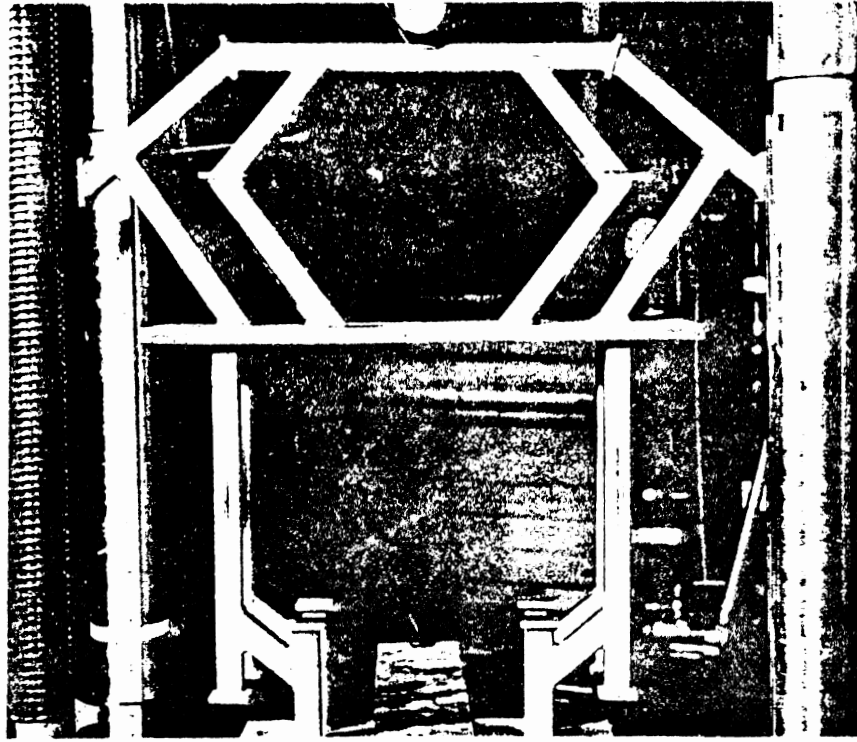


FIG. 6 SPACE FRAME BEFORE DEFORMATION

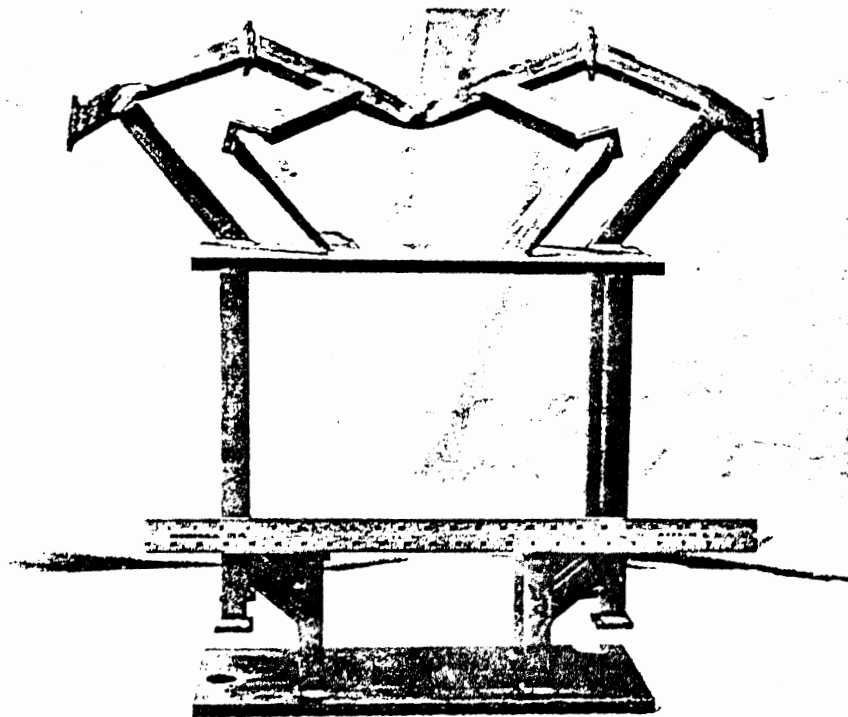


FIG. 7 SPACE FRAME AFTER DEFORMATION

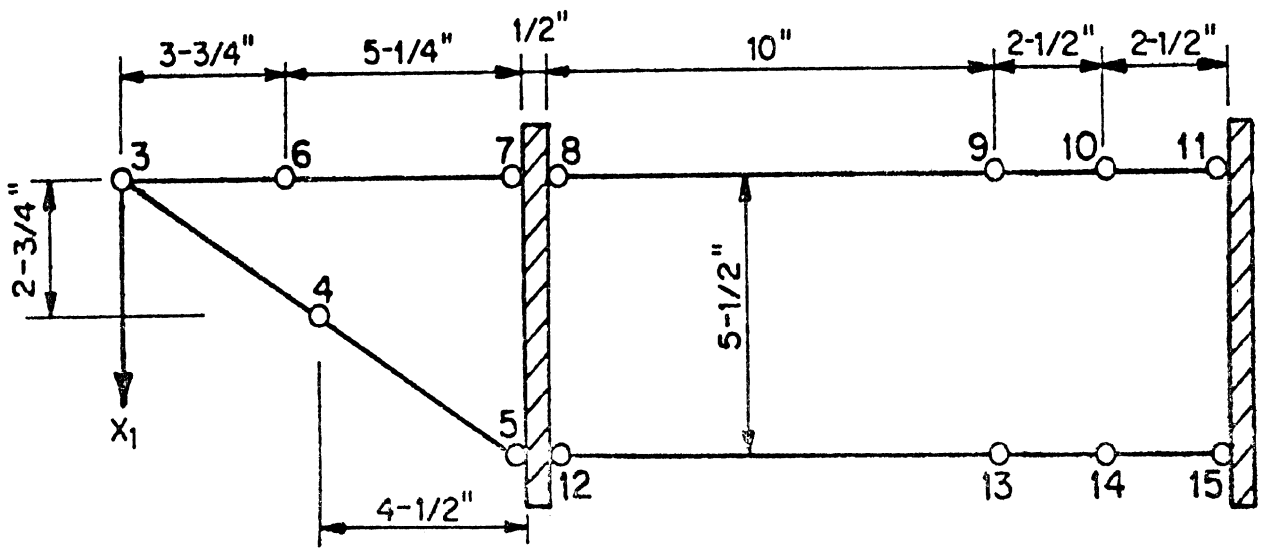
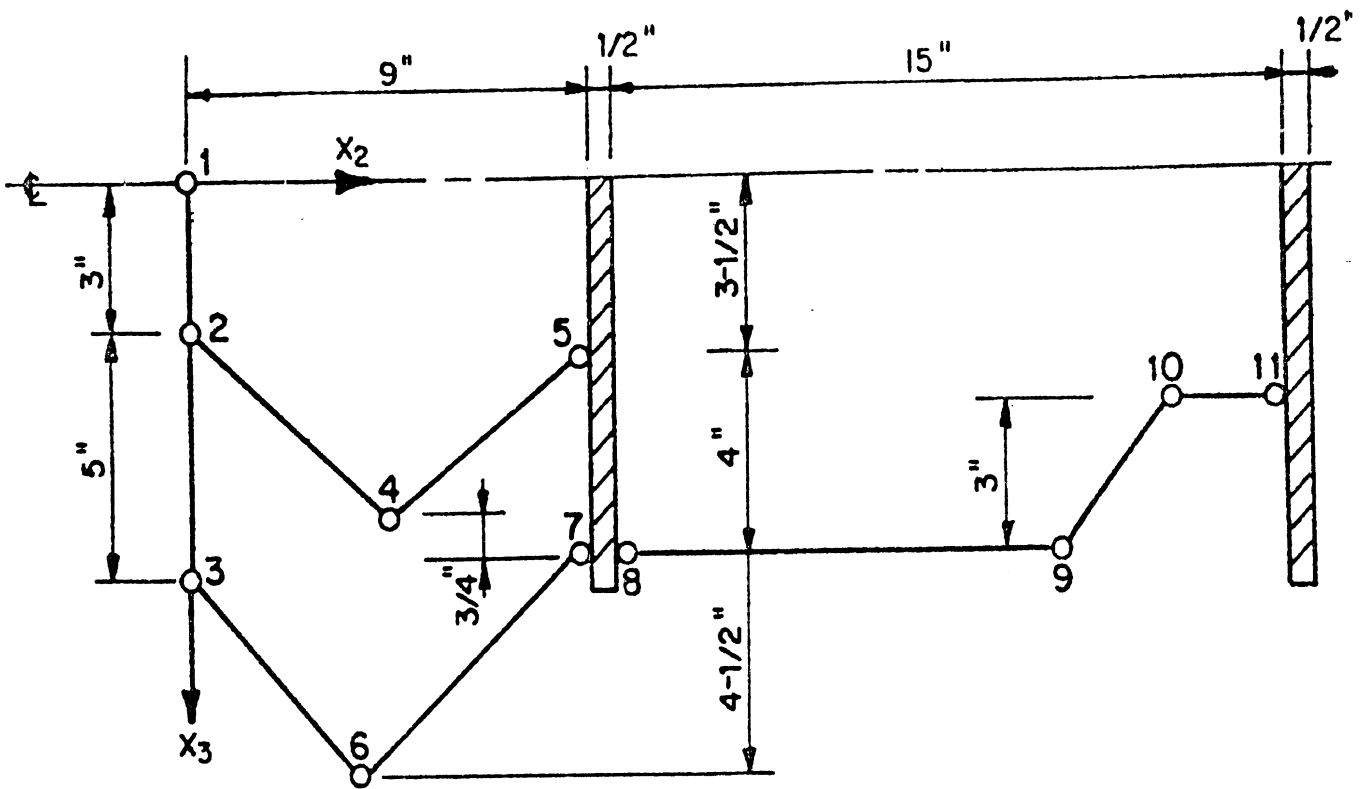


FIG. 8 FRAME MODEL

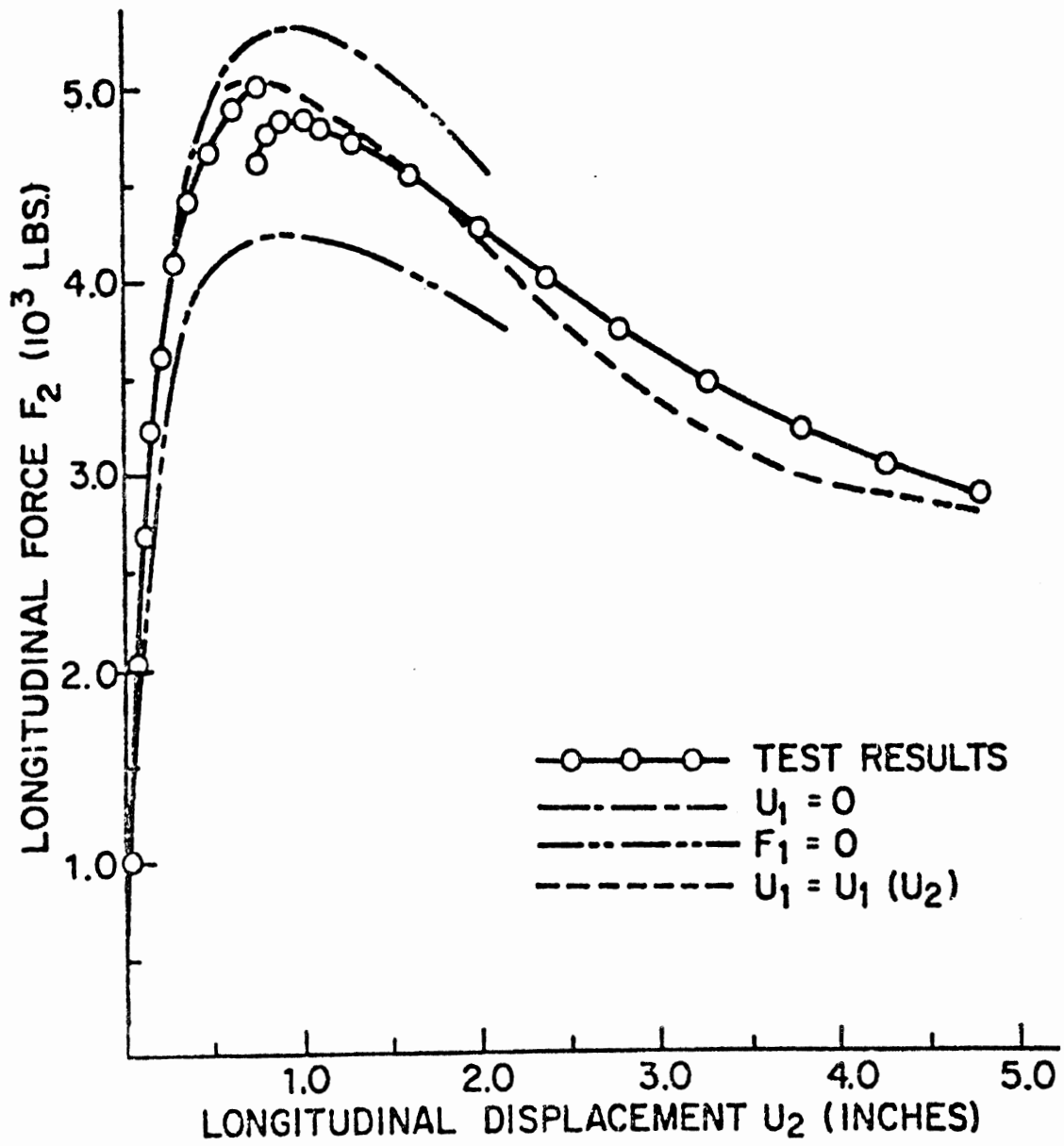


FIG. 9 EXPERIMENTAL AND COMPUTED FORCE-DEFORMATION CURVE

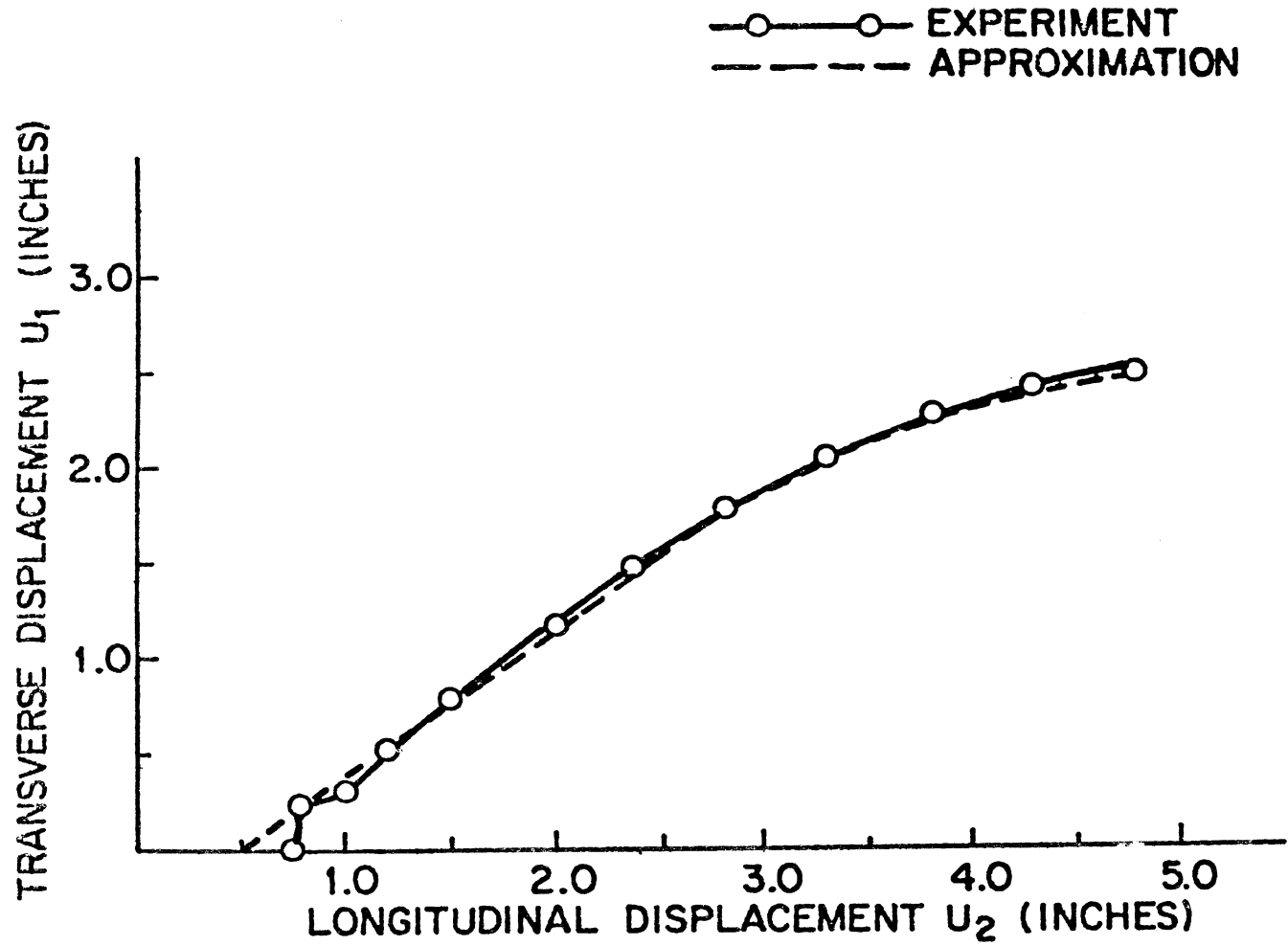


FIG. 10 EXPERIMENTAL TRANSVERSE
VS LONGITUDINAL DISPLACE-
MENT

4. Dynamic Validation Tests

4.1 Introduction

This Chapter presents the results of two experimental crash tests designed to validate the computer simulation. The test structures were idealized quarter scale models consisting of frame and rigid body elements. The model is shown in Fig. 11. Similar structures have been previously used in scale modeling studies.* In both tests the models were impacted against a pole obstacle at 30 MPH. The first test was a direct symmetric impact. In the second test the frame was rotated 18° to the direction of travel. The test procedure and instrumentation are described in a later section.

For the purpose of validating the simulation program attention is focused on response variables of importance to crashworthiness applications. In particular detailed comparison is made of predicted and experimental results for the collapsed shape of the structure, accelerations at two locations on the rear (passenger compartment) plate, and the impact force at the pole barrier. For the symmetric test agreement is good for all variables. In addition the simulation accurately predicted the duration of the crash event. The results for the unsymmetric test are not as uniformly good. The collapse mode is qualitatively correct, but quantitative differences are observed. The actual crash duration was about 25%

* B. S. Holmes, G. Sliter, "Scale Modeling of Vehicle Crashes", SAE Paper No. 740586, 1974.

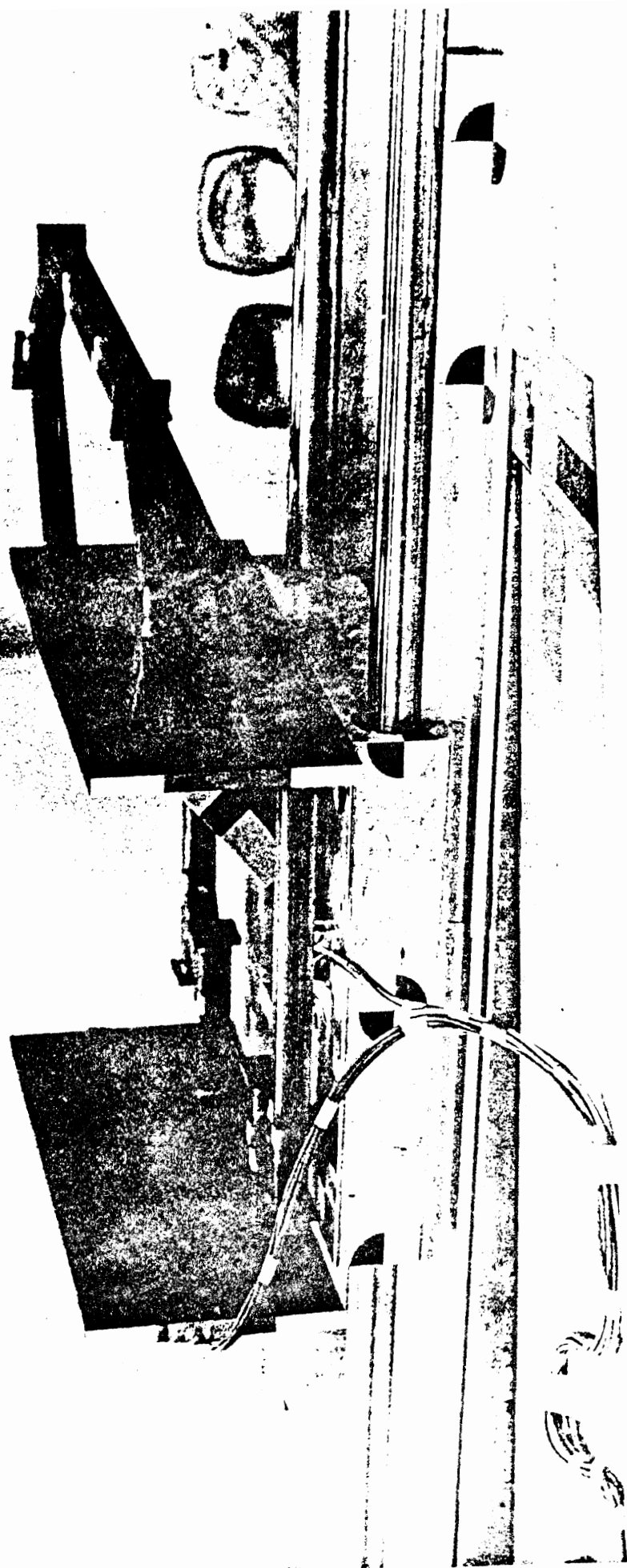


FIG. 11 SCALE MODEL MOUNTED
ON MINI-SLED

longer than predicted. Accelerations and the barrier force show reasonable agreement over most of the test event but in general are less accurate than the symmetric case. In the unsymmetric test a partial fracture occurred in the front beam in the contact region. Fracture is not accounted for in the simulation, and this is the probable reason for the discrepancies observed.

The comparison of predicted and observed accelerations requires some additional comment. The raw acceleration data contained considerable high frequency content due to elastic ringing of the plates. The simulation necessarily modeled the plates as rigid bodies which precludes comparison with the raw signals. Thus the comparison of simulation and experiment is sensitive to the filtering of the raw test data as well as to the method of numerical integration.

In this paper the simulation results are compared to the experimental signal at three different filtering frequencies (350 Hz, 150 Hz, 60 Hz). The upper frequency for comparison was chosen on the basis of the predicted signal. As discussed in Chapter 2 the program uses an implicit, variable step integration procedure which determines the step size appropriate for following the dynamic plastic collapse. For the simulated tests the frequency content of the computed signal was approximately 300 Hz. Thus 350 Hz was chosen as an appropriate frequency for comparison.

4.2 Test Procedure

The test structures (Fig.11) are idealized quarter scale models made from one inch square mechanical steel tubing with 0.075 inch wall thickness. The material stress-strain curve is given in Appendix D. Over the strain range indicated it can be approximated by an elastic-perfectly plastic material with an elastic modulus of 20×10^6 psi and yield stress of 61,500 psi. Characteristic features of the formation of plastic hinges in this tubing are discussed in Appendix D. Two half-inch thick steel plates each weighing 20 lbs. act as rigid body masses. The structures were Heli-arc'd, and no welds failed during the tests.

A schematic of the experimental set-up is shown in Fig. 12. The frame models were mounted on a "mini-sled" on rails. The two models were essentially identical, except that the oblique model was mounted differently on the mini-sled and required different gussets. The orientation of the models for the two tests is shown in Fig.13. The mini-sled was made from solid 3" square bar. It was lightened by boring each piece to remove as much material as possible. Thomson split ball-bushing bearings were inserted at four places. The total weight was 25.5 lbs. The track on which the mini-sled rides was made of 1-1/2" diameter steel rod supported by commercial aluminum rails. The rail system was in turn supported by a steel framework welded from 3" square tubing. This framework was bolted to The University of Michigan's impact sled using special shims to insure a horizontal surface. The purpose of mounting a "sled upon a sled" was to increase the relative velocity between mini-sled and pole and yet work at lower impact sled speeds.

The mini-sled was restrained to prevent relative motion during the acceleration of the impact sled. During the rebound of

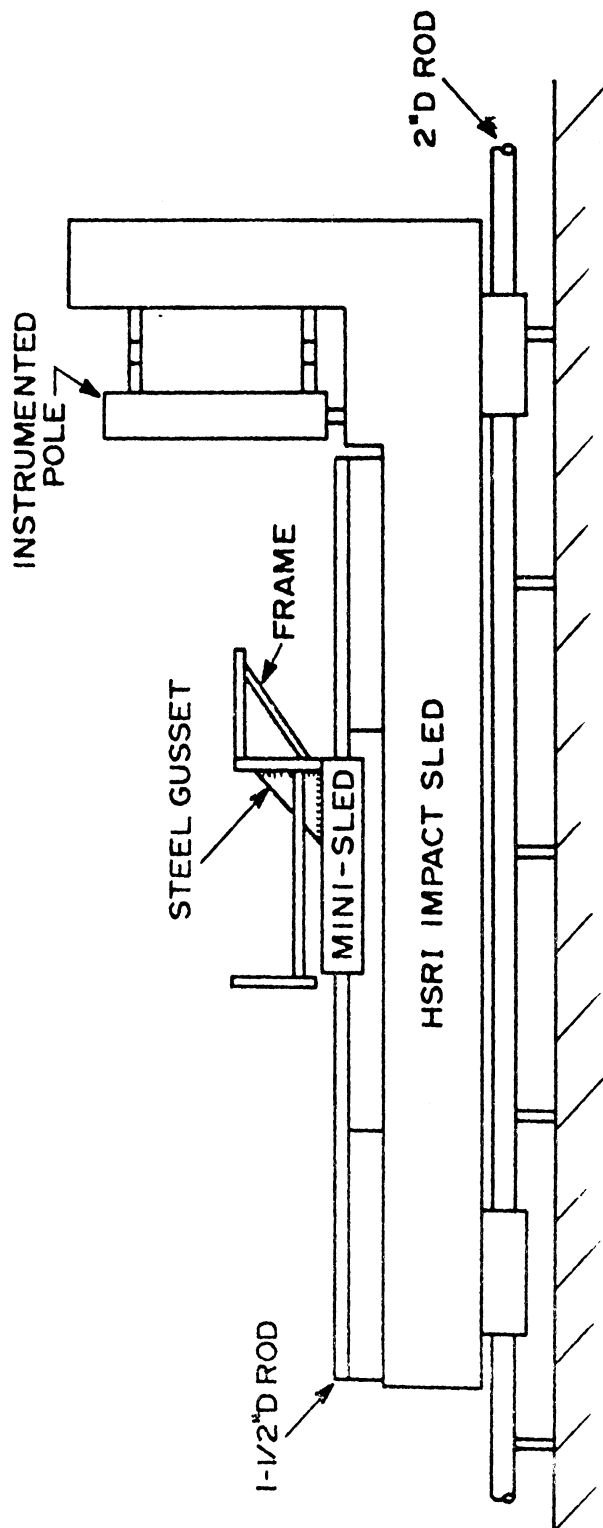
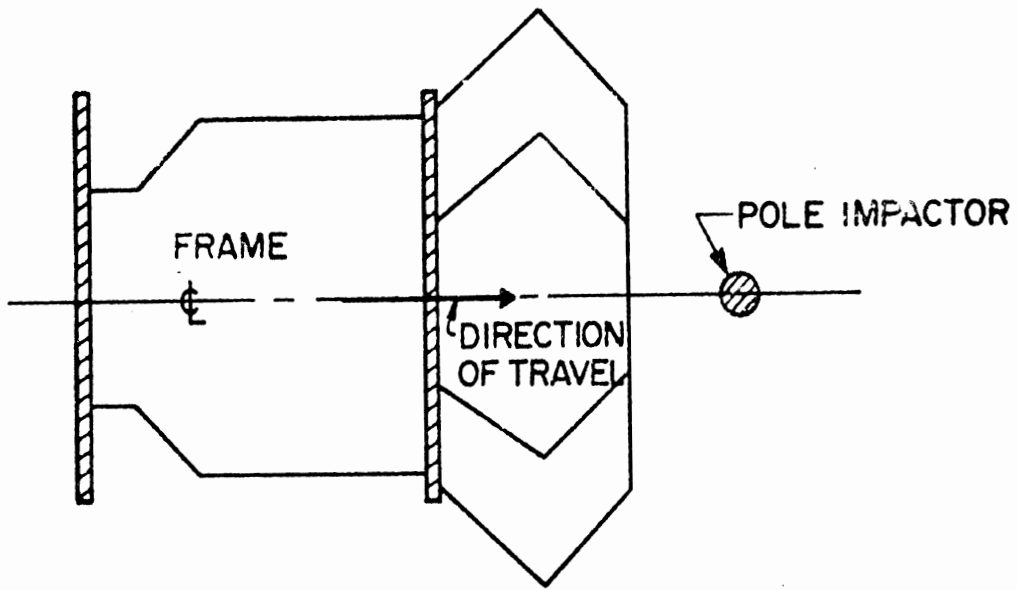
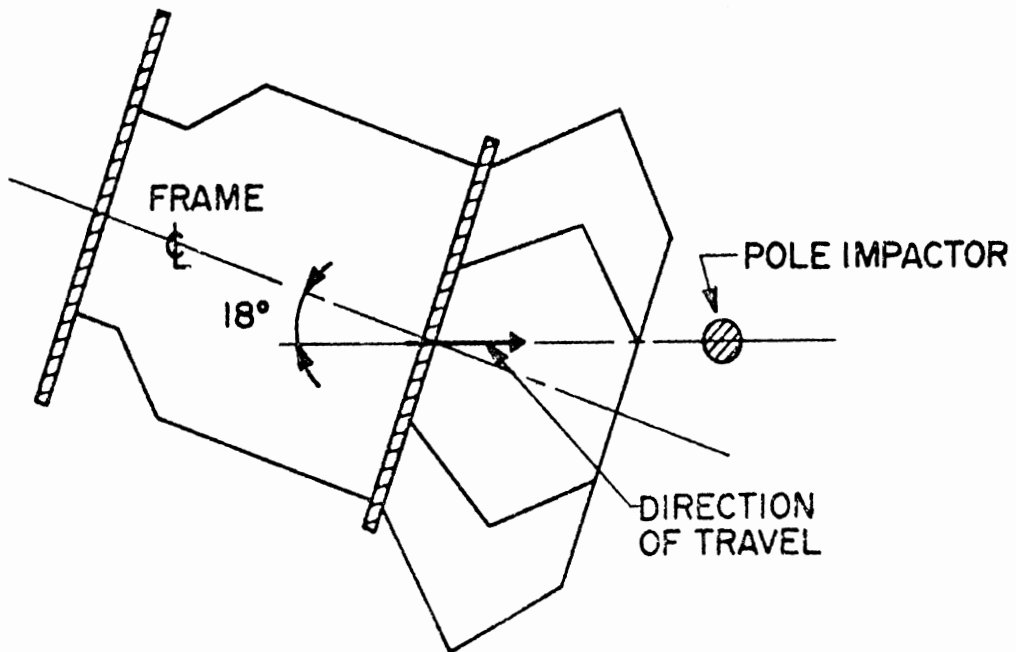


FIG. 12 SCHEMATIC OF IMPACT TEST



(a) SYMETRIC TEST



(b) UNSYMMETRIC TEST

FIG. 13 MODEL ORIENTATION FOR SYMMETRIC AND UNSYMMETRIC TESTS

the sled from an air spring, the mini-sled was free to move to the right and collide with the pole barrier. In both tests the differential impact velocity was 30 ± 0.1 MPH.

The pole barrier was a 3-1/2 inch diameter steel pole bored out 2 inches to save weight and improve frequency response. The pole was connected to a rigid box by four Kistler piezoelectric load links in the horizontal direction and one such link in the vertical direction. This allows resolution of all force components on the pole with 1 millisecond response time. The pole was statically tested to obtain calibration factors to account for the bending stiffness of the load links.

Acceleration data for the rear plate (passenger compartment mass) were obtained from four Setra ± 250 g accelerometers placed on the back side of the plate. Two were located on the vertical plate axis one inch from the top and bottom of the plate. The accelerometer axis was oriented normal to the plate. The other two were located on the horizontal plate axis and were oriented in the vertical and transverse direction in the plane of the plate. The latter two accelerations were small compared to the top and bottom normal accelerations and are not reported here. The electric signals from the accelerometers and load cells were carried from the mini-sled in an umbilical bundle of cables, fed to a control room and magnetically recorded.

To obtain the barrier force the load cell signals needed to be corrected for bending effects and vectorially summed. To facilitate this data reduction, the signal was digitized at 11,300 Hz and then digitally filtered with a cutoff frequency of 1000 Hz. The

raw accelerometer signals were filtered by electronic (Kronhite) filters at three different frequencies (350 Hz, 150 Hz, 60 Hz).

4.3 Comparison of Simulation and Experimental Results

The simulation program was exercised on the model shown in Fig. 14. It consists of 21 nodes, 18 beam elements, and two rigid bodies for a total of 138 degrees of freedom. For the direct test symmetry of the model was exploited reducing the size to 78 degrees of freedom. It was assumed that the front plate was rigidly connected to the mini-sled. Thus the front mass was constrained except for translation in the direction of travel. The only other boundary condition was imposed on the contact node. Instantaneous stopping of the contact node is an overly severe approximation of the complex local conditions in the impact region. To account for this the contact node was brought to rest in the direction of travel in a stopping distance of 0.25 inches. The associated stopping time was one millisecond. Rotations and motion normal to the direction of travel were unconstrained.

Plastic Collapse

The deformed shape of the collapsed forestructure was measured after the test relative to the front plate. For comparative purposes the simulation was exercised until the relative displacement between the nodes and the front plate was constant giving the predicted crush after rebound. A comparison of the predicted and test results for the symmetric test is shown in Fig. 15. The scales of the undeformed and deformed frame are the same indicating

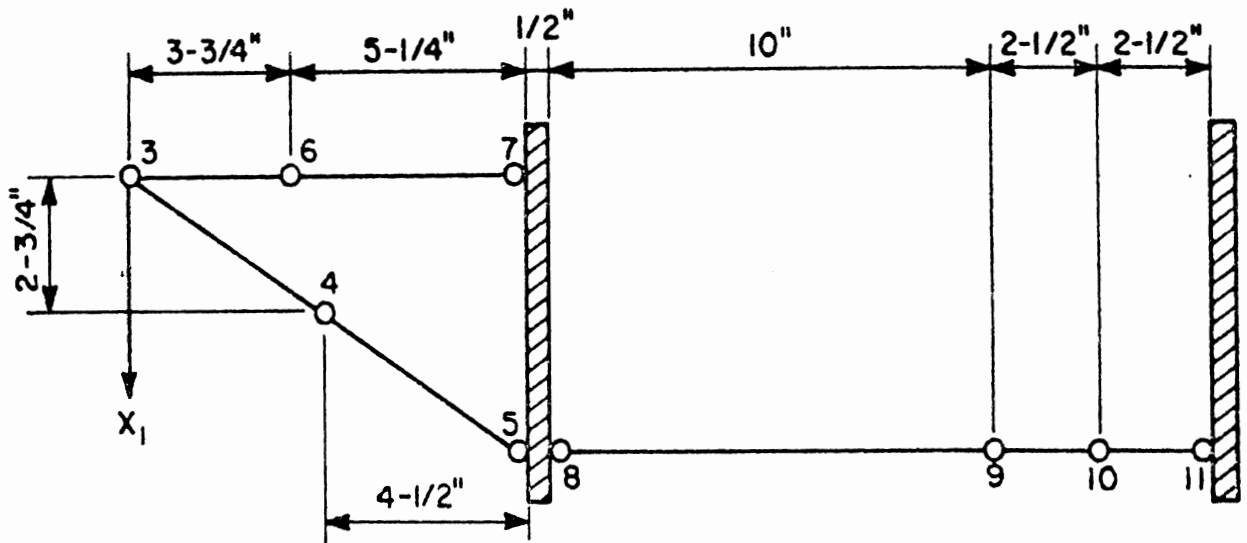
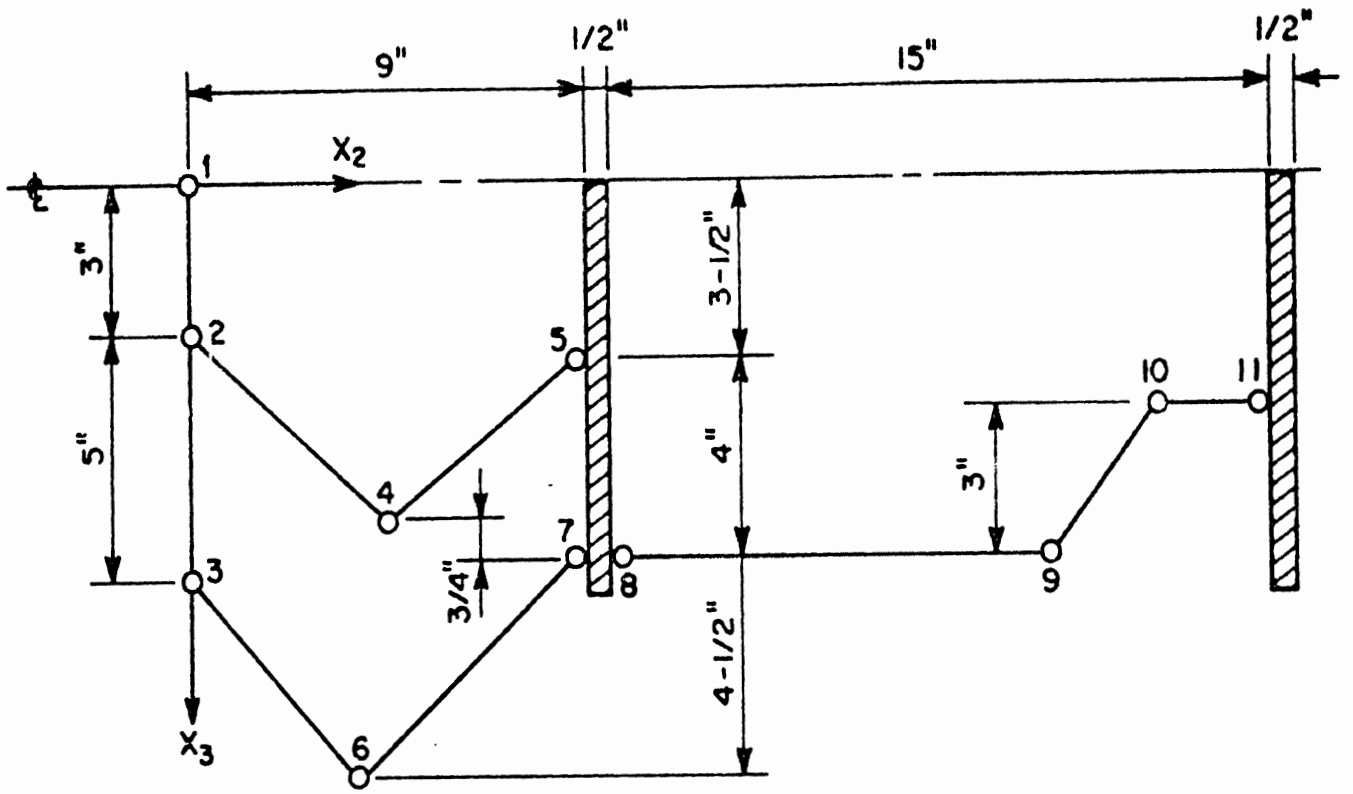


FIG. 14 SIMULATION MODEL

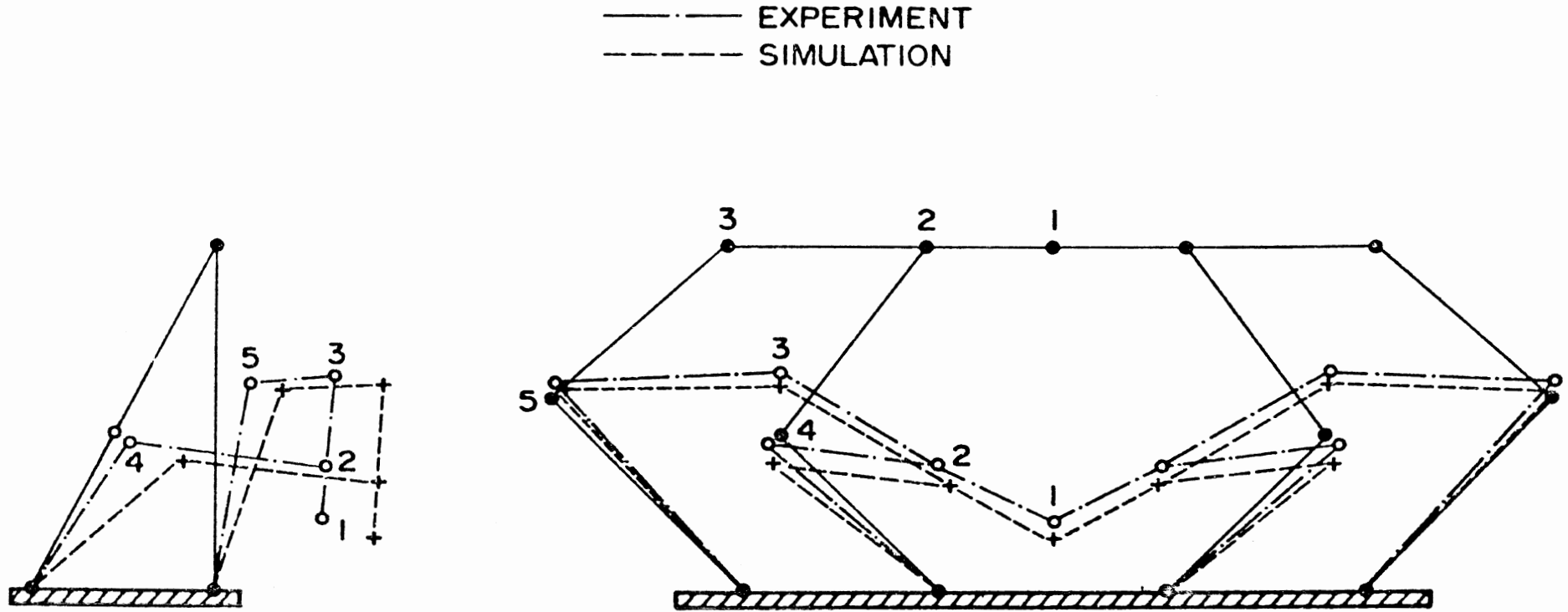


FIG. 15 FINAL DEFORMED SHAPE
SYMMETRIC TEST

the severity of the crush. The crush displacement of node 1 was 7.2 inches or 80% of the original clearance. The side view illustrates the pronounced upward rotation of the structure during crush. In general the predicted and experimental results are in good agreement. The largest discrepancy is the somewhat larger predicted rotation of node 4.

Analogous results for the unsymmetric test are shown in Fig. 16. Although showing qualitative agreement, the comparison is considerably less satisfactory. The predicted structure is overly stiff. Consequently rebound occurs too soon (as will be evident from the acceleration results). Also the prediction indicates greater plastic rotation at the left plate nodes than exhibited by the test.

The interpretation of the unsymmetric test is complicated by the fracture that occurred about 1-1/2 inches to the right of node 1. (Node 1 was the initial contact point but in the test slid to the left of the post). Such a fracture would certainly reduce the stiffness of the structure. Moreover it would lead to a greater "hinging action" in the vicinity of the fracture. Both factors are consistent with the differences observed. Thus the lack of detailed agreement can probably be attributed to this cause.

Barrier Force

As discussed earlier the load cell signals were digitized and filtered with a digital filter with a band pass of 1000 Hz. The resulting individual signals were combined to give force components. The result for the longitudinal force in the symmetric test is shown

— EXPERIMENT
 - - - SIMULATION

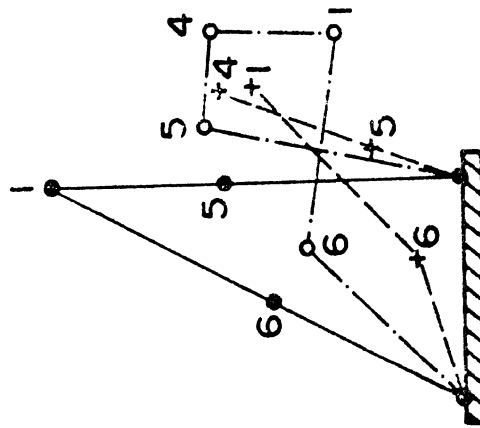
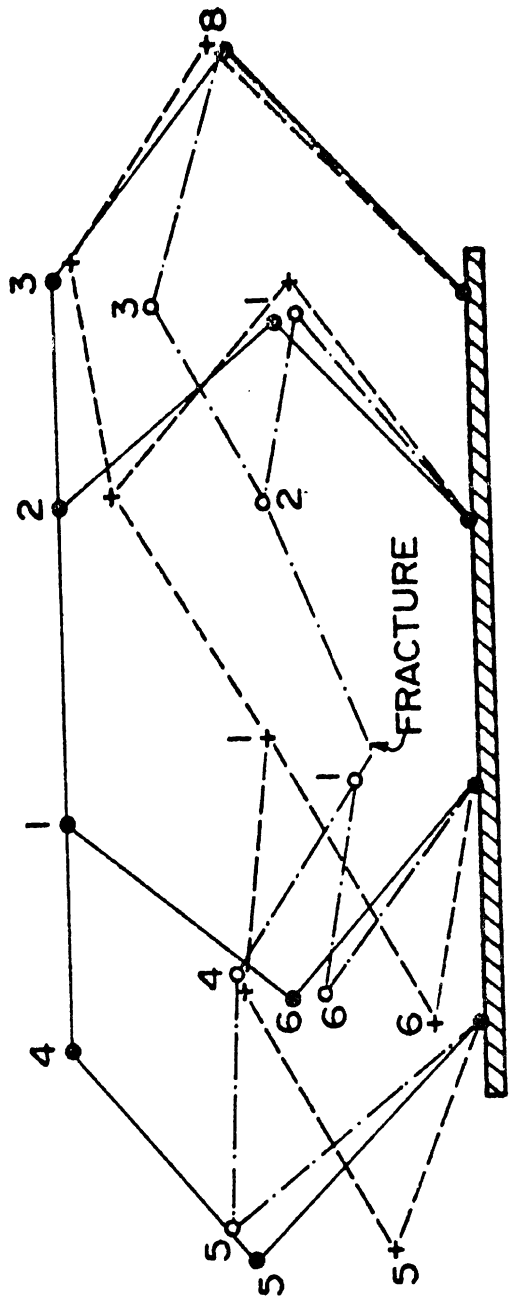


FIG. 16 FINAL DEFORMED SHAPE
 UNSYMMETRIC TEST

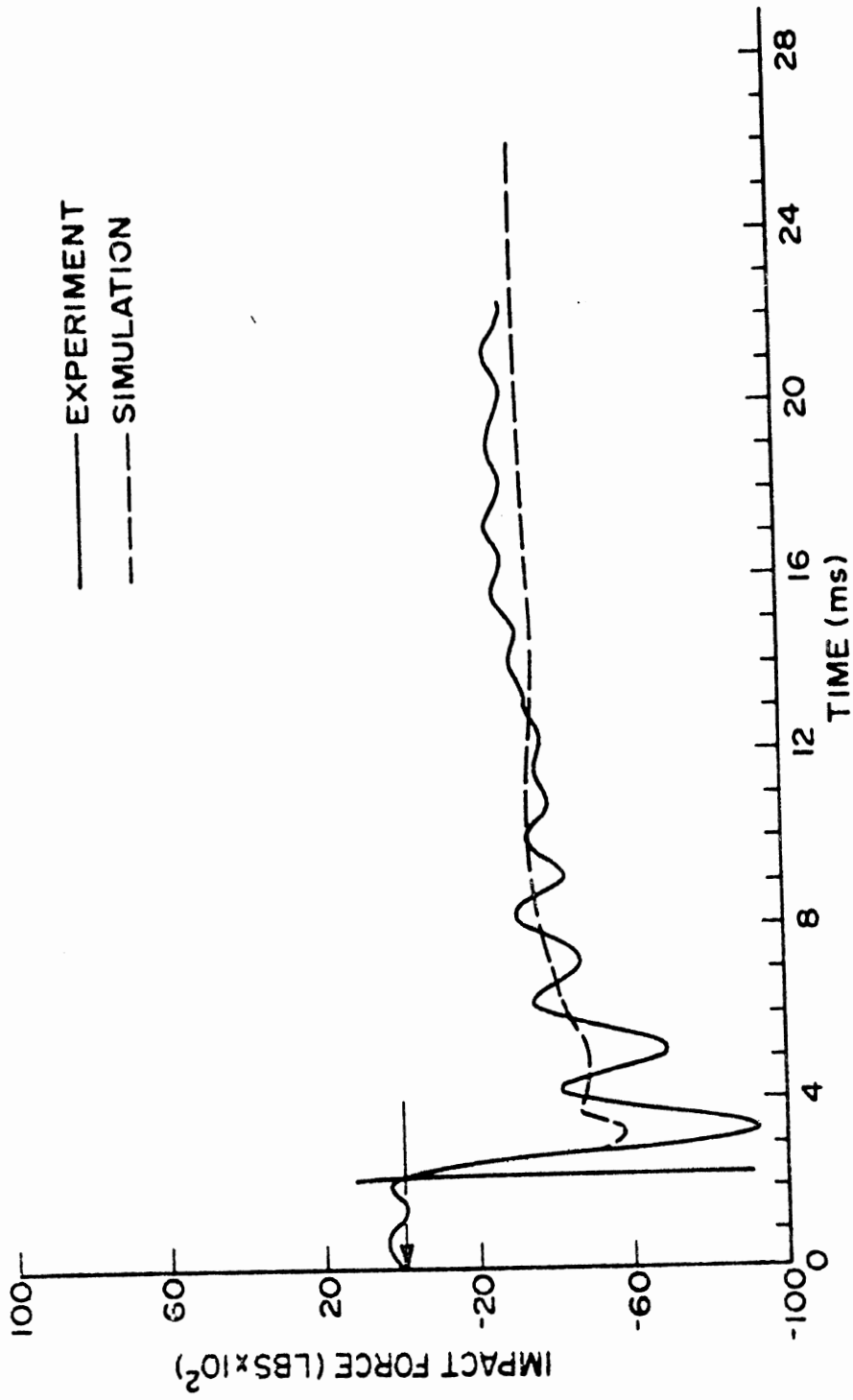


FIG. 17 BARRIER FORCE
SYMMETRIC TEST

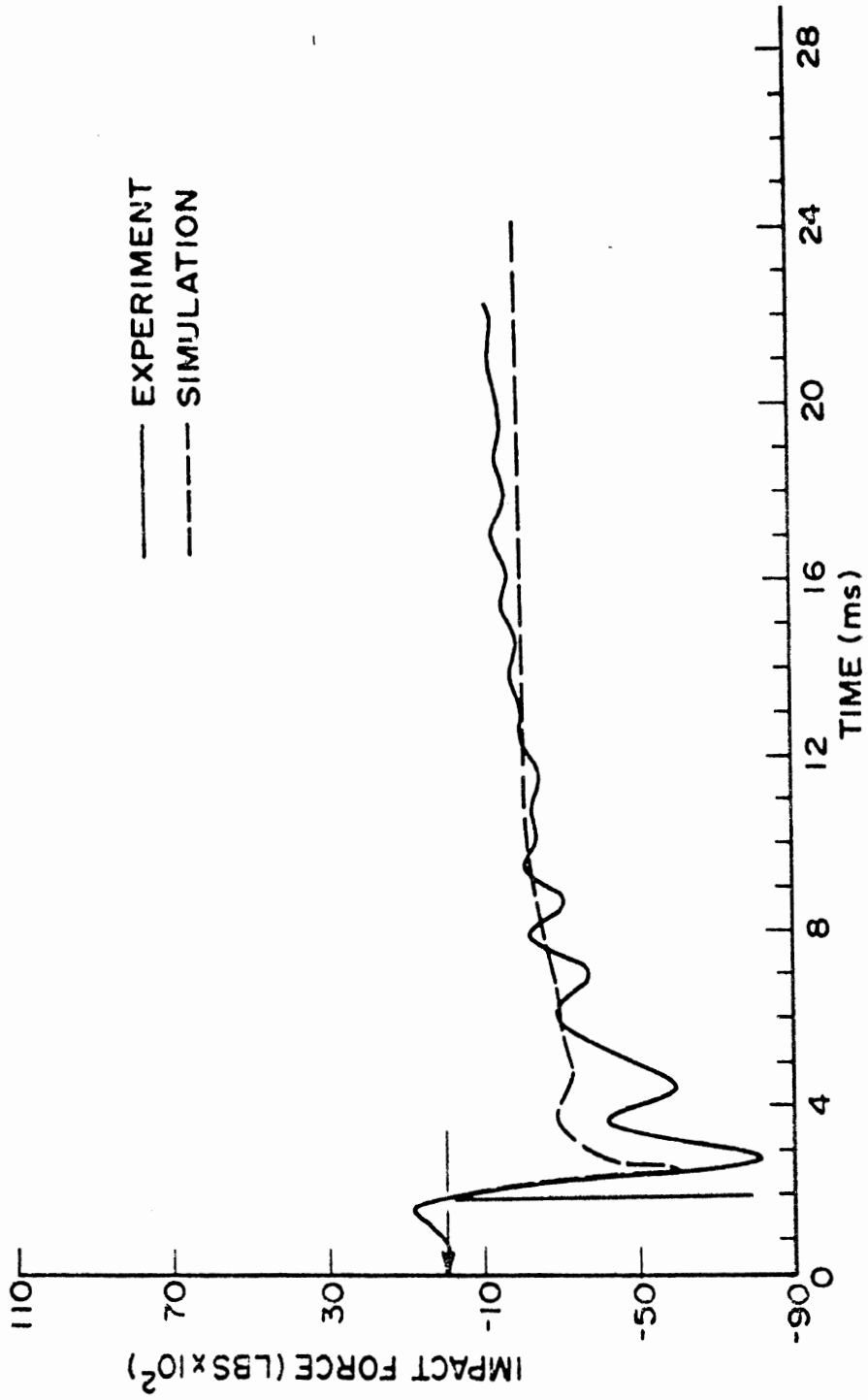


FIG. 18 BARRIER FORCE
UNSYMMETRIC TEST

in Fig. 17. The result for the unsymmetric test in Fig. 18 is for the force component at 45° to the pole. The time origin is shown at the point of initiating digitizing the signal. The time of impact is indicated by the vertical line.

The simulation predictions are shown in the figures as dotted lines. The initial peak force of the prediction is considerably attenuated from the test result, but in both cases it shows good agreement after about 3 ms. In comparing the response it should be noted that the actual pole barrier was mounted to the impact sled by the load cell links. The elastic stiffness of this system was designed to give a response time of less than 1 ms. The exact frequency response of the pole-load cell system is not known, but the observed early oscillations are compatible with the designed response time. This suggests that they are due to the elasticity of the barrier rather than inherent in the structural response.

Acceleration

Experimental and predicted accelerations were compared for two points on the rear mass located one inch from the top and bottom of the plate. Due to angular rotation of the plate the acceleration at the two points is quite different emphasizing the multi-dimensional nature of the response.

Experimental and predicted results for the symmetric impact are shown in Figs. 19 and 20. The corresponding results for the unsymmetric test are given in Figs. 21 and 22. In each case the raw accelerometer signals were filtered by electronic (Kronhite) filters

at three different frequencies (350 Hz, 150 Hz, 60 Hz). The origin of the time axis is the instant of impact. Prior to impact the model is ideally in a state of uniform motion. In reality a dynamic excitation is imposed on the mini-sled from vibrations of the impact sled. Although small compared to the peak accelerations after impact, this noise level is about 10 g (at 350 Hz) at the time of impact.

The dashed curve in each figure is the predicted simulation result. As discussed earlier the simulation employs a variable step size chosen on the basis of error measures associated with the plastic collapse. Typically small steps are required during the active formation of plastic hinges. Once the dynamic collapse mode is established, however, the plastic collapse can be accurately followed with rather large steps. Since frequency resolution is inversely proportional to step size, the simulation results will exhibit a smoothing as time increases. It can be anticipated that during the early stage the time step will be such to approximate the elastic response (since the initial elastic state dictates the hinge formation), but that later elastic oscillations will be suppressed.

The simulation predictions shown in Figs. 19-22 demonstrate these characteristic features. During the first 5 ms of the event, the average step size was 0.05 ms (5×10^{-5} seconds). During the next 20 ms of the event the step size increased incrementally to 1 ms at which size it remained for the last 15 ms of the event. The total number of steps for the 40 ms simulated was 165. Thus the average step size was about 0.24 ms, but the actual step size varied from 0.05 to 1 ms.

Figs. 19-20 for the symmetric test show good agreement between the predicted and experimental results in the sense described above. During the initial stage of the motion, the peak amplitudes of the experimental results filtered at 350 Hz are predicted within the noise level of the signal. As time increases the predicted result is smoothed by the increased time step. That it is accurately predicting the experimental results with the elastic oscillations suppressed is evidenced by the comparison with the test data filtered at lower frequencies.

The results for the unsymmetric test in Figures 21 and 22 show generally similar behavior. Agreement for the top plate acceleration is quite good except that the predicted duration of the event is too short. This is consistent with the collapse prediction and can probably be attributed to the occurrence of fracture in the actual test. The predicted result for the bottom plate acceleration shown in Figure 22 is somewhat less satisfactory. Both the peak and average amplitudes are matched quite well, but the frequency content during the early stage indicates some discrepancy.

4.4 Discussion

In our opinion the comparative results above show reasonable agreement between the simulation predictions and the experimental results. The unsymmetric results are generally less satisfactory, but their interpretation is complicated by the fracture that occurred. It should be noted that there is a second source of error in the unsymmetric simulation. In the test the contact point is not fixed but moves off the initial contacting node along the beam as the

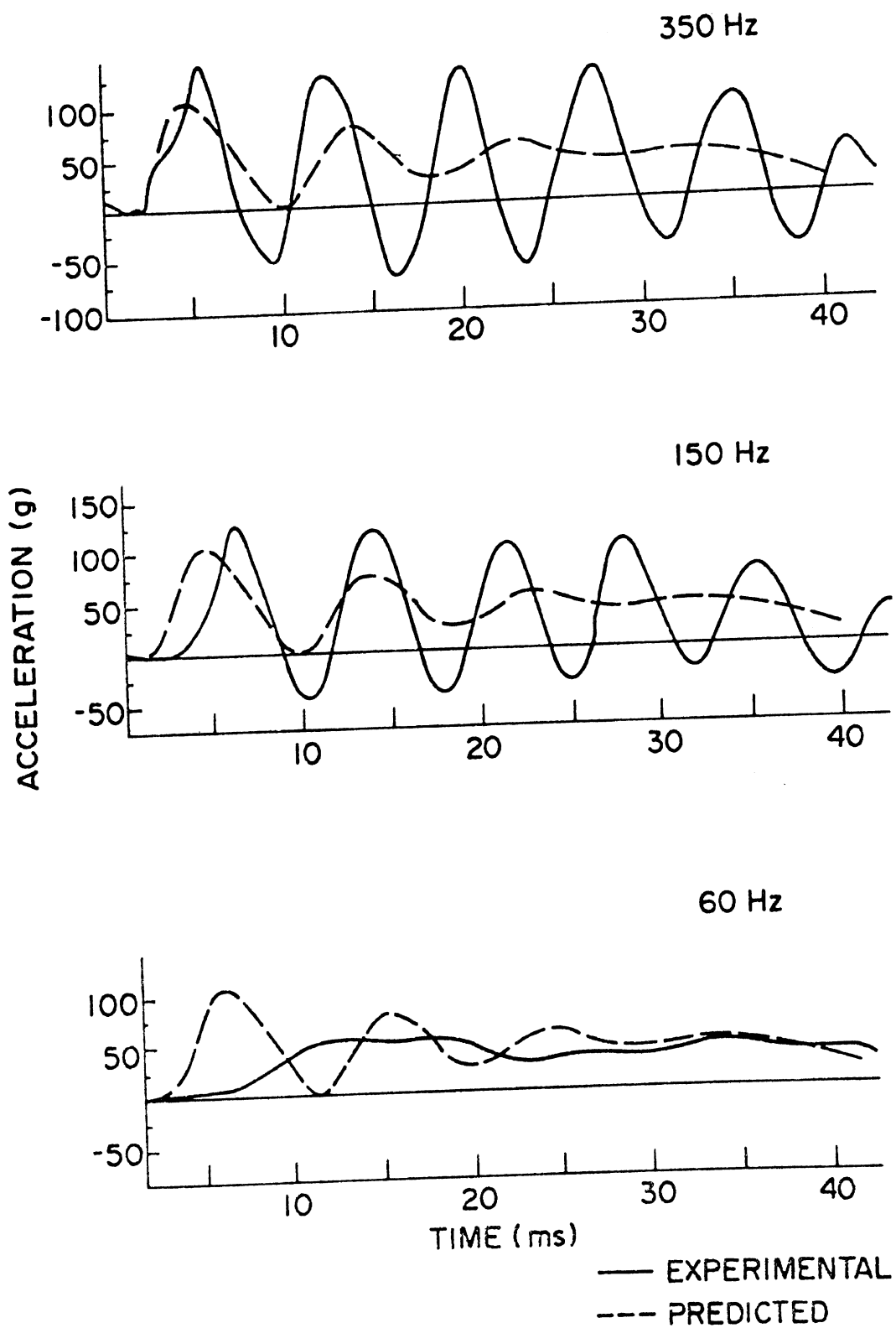


FIG. 19 TOP PLATE ACCELERATION
SYMMETRIC TEST

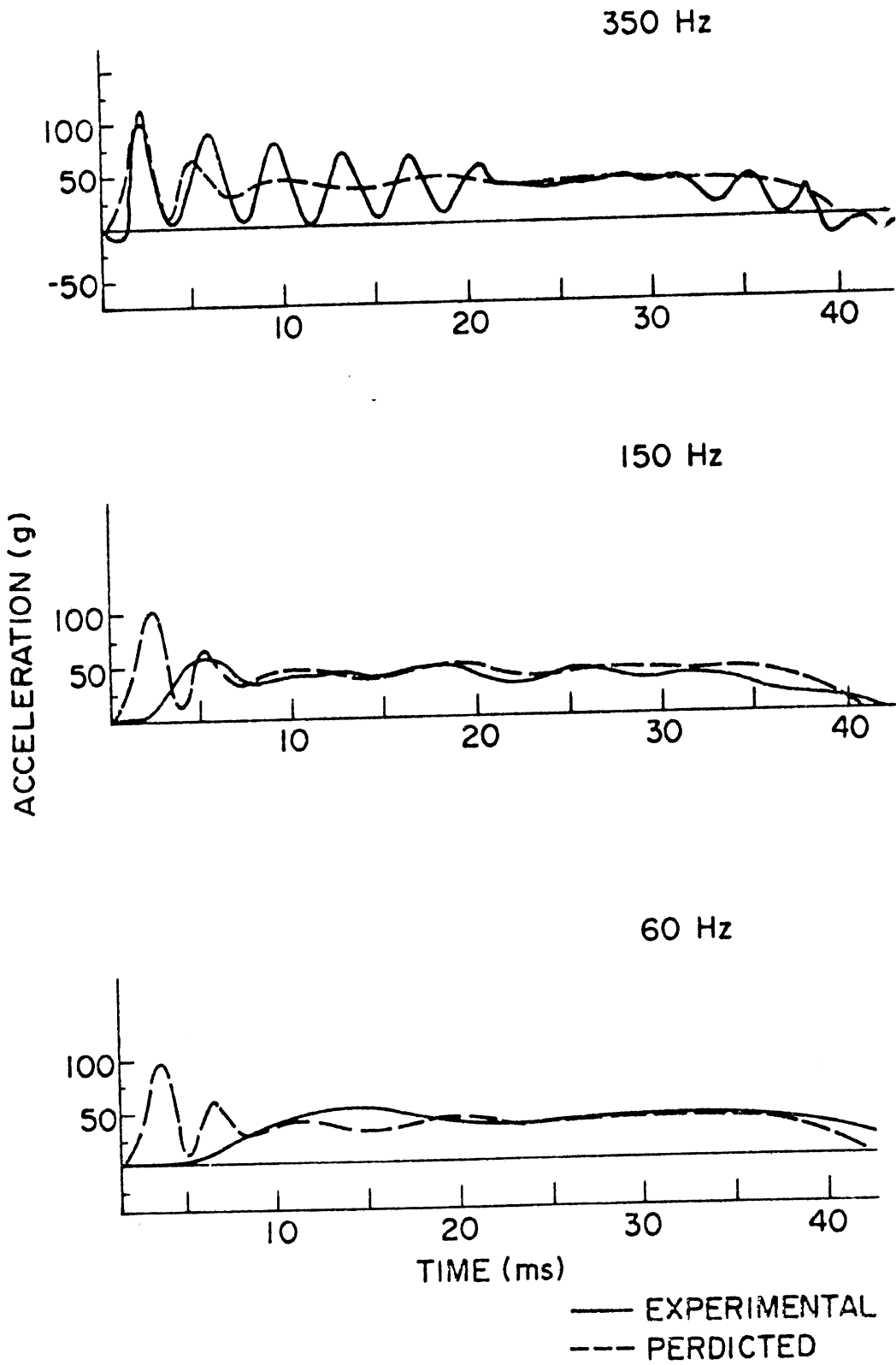


FIG. 20 BOTTOM PLATE ACCELERATION
 SYMMETRIC TEST

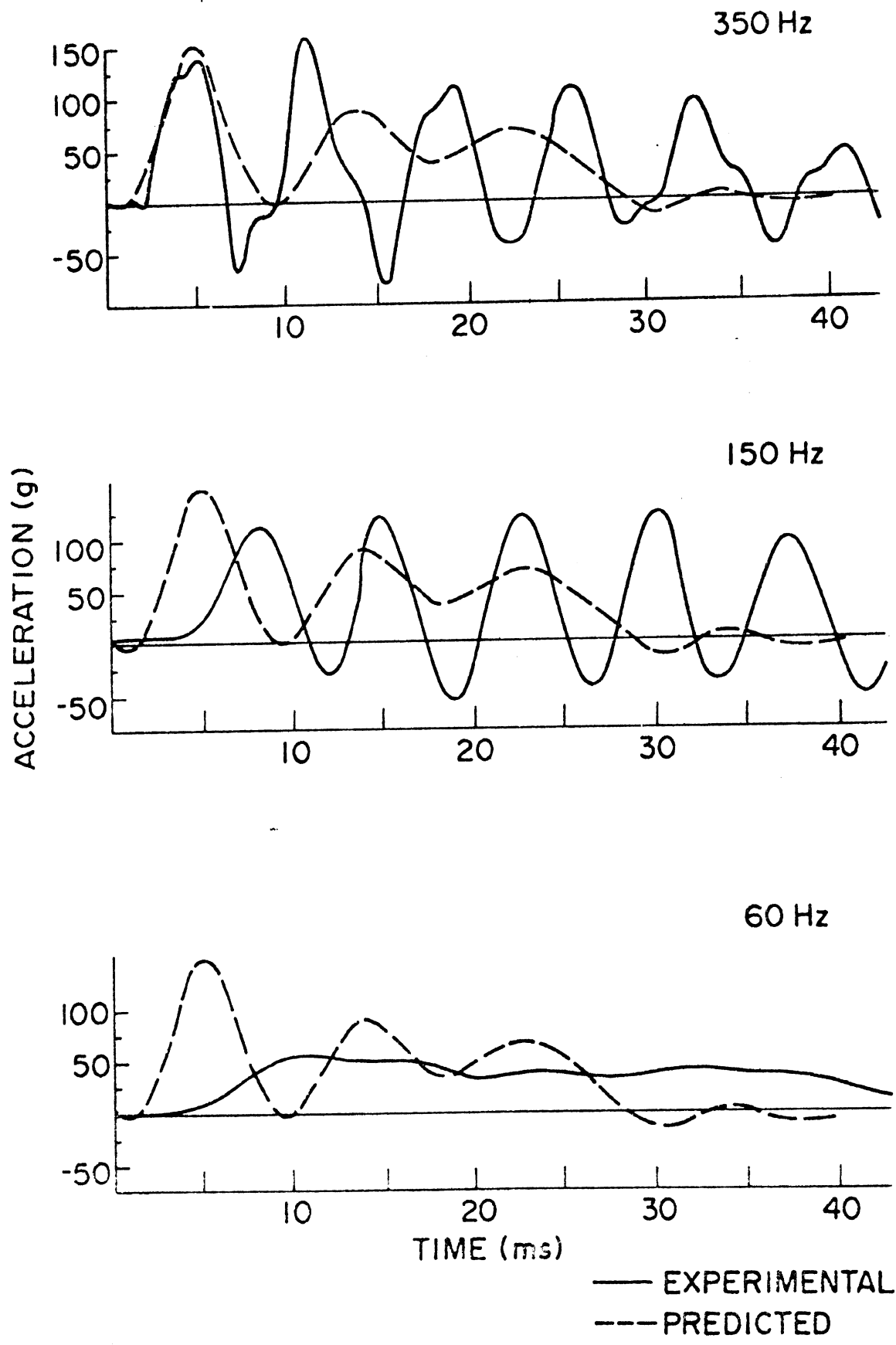


FIG. 21 TOP PLATE ACCELERATION
UNSYMMETRIC TEST

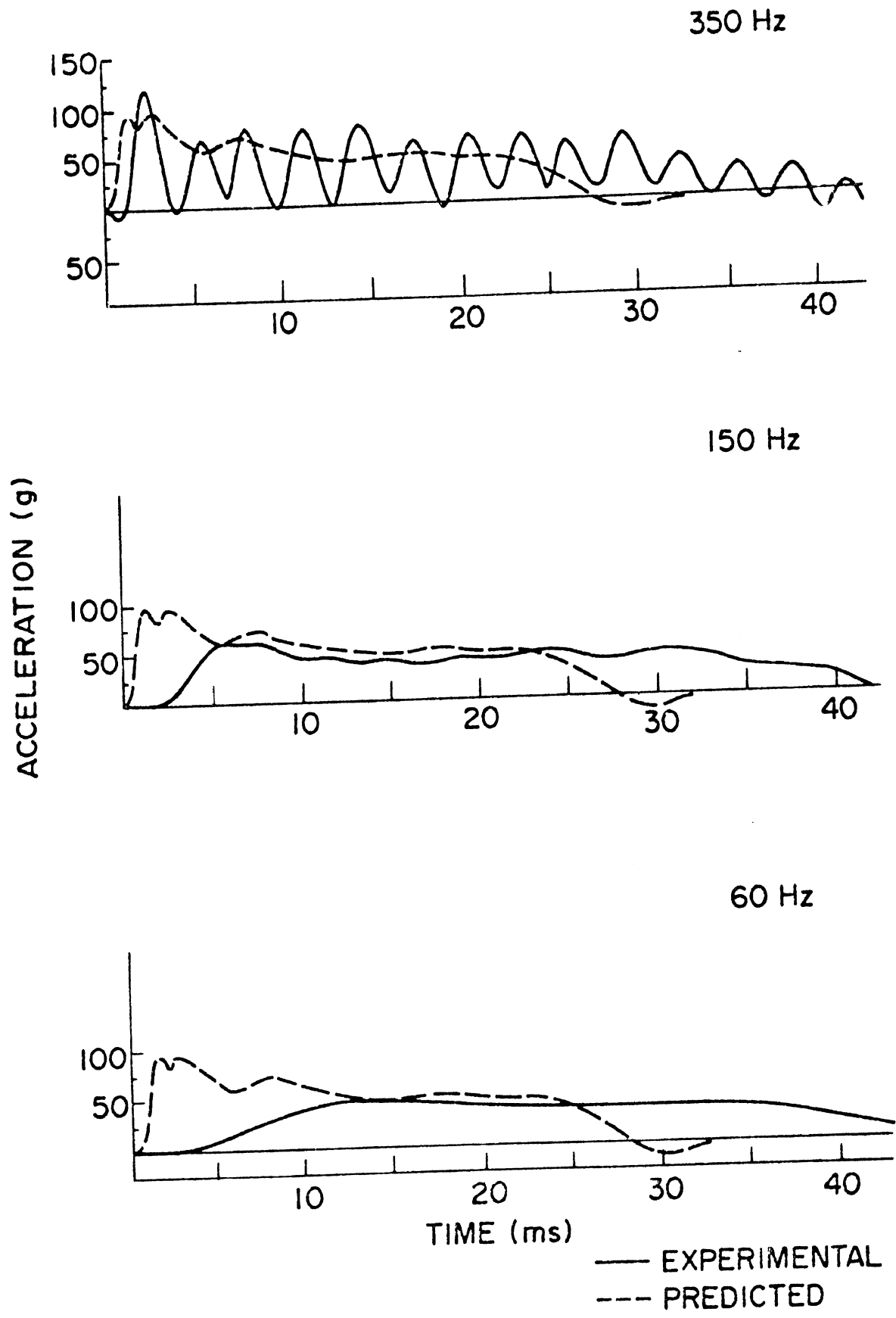


FIG. 22 BOTTOM PLATE ACCELERATION UNSYMMETRIC TEST

deformation increases. The simulation constrains the motion of this node in the direction normal to the pole thus permitting relative motion only in the tangent plane. Moreover the simulation essentially assumes that the barrier force continues to act on the node. These approximations are probably valid if the relative motion is sufficiently small. Unfortunately their quantitative effect can not be assessed from the reported test because of the occurrence of fracture.

The acceleration comparisons also requires some additional comment. In dynamic validation tests there is always the question as to what frequency content should be included in the comparison between simulation and experiment. In one sense the variable step procedure provides the answer in that it retains whatever frequency content is necessary to follow the plastic collapse. If it is accepted that this is the prime factor for structural crashworthiness applications, then the experimental results should be predicted up to this frequency content.

To verify that the smoothed predicted results is a property of the variable step procedure, Fig. 23 shows simulation results for the symmetric bottom plate acceleration. The variable step prediction is compared to results limiting the maximum step size to 0.1 ms and using a constant step size of 0.05 ms. The increased frequency resolution with smaller step size is apparent. Moreover the result using 0.05 ms is in good agreement with the experimental result filtered at 350 Hz shown in Fig. 20 over the entire 15 ms simulated. We conclude that for this step size the simulation has adequate frequency resolution up to 350 Hz.

Simulation computations were carried out on The University of Michigan IBM 370/74 computer. For the symmetric test the crash duration of 40 ms required 165 steps. Total CPU time was 94 seconds.

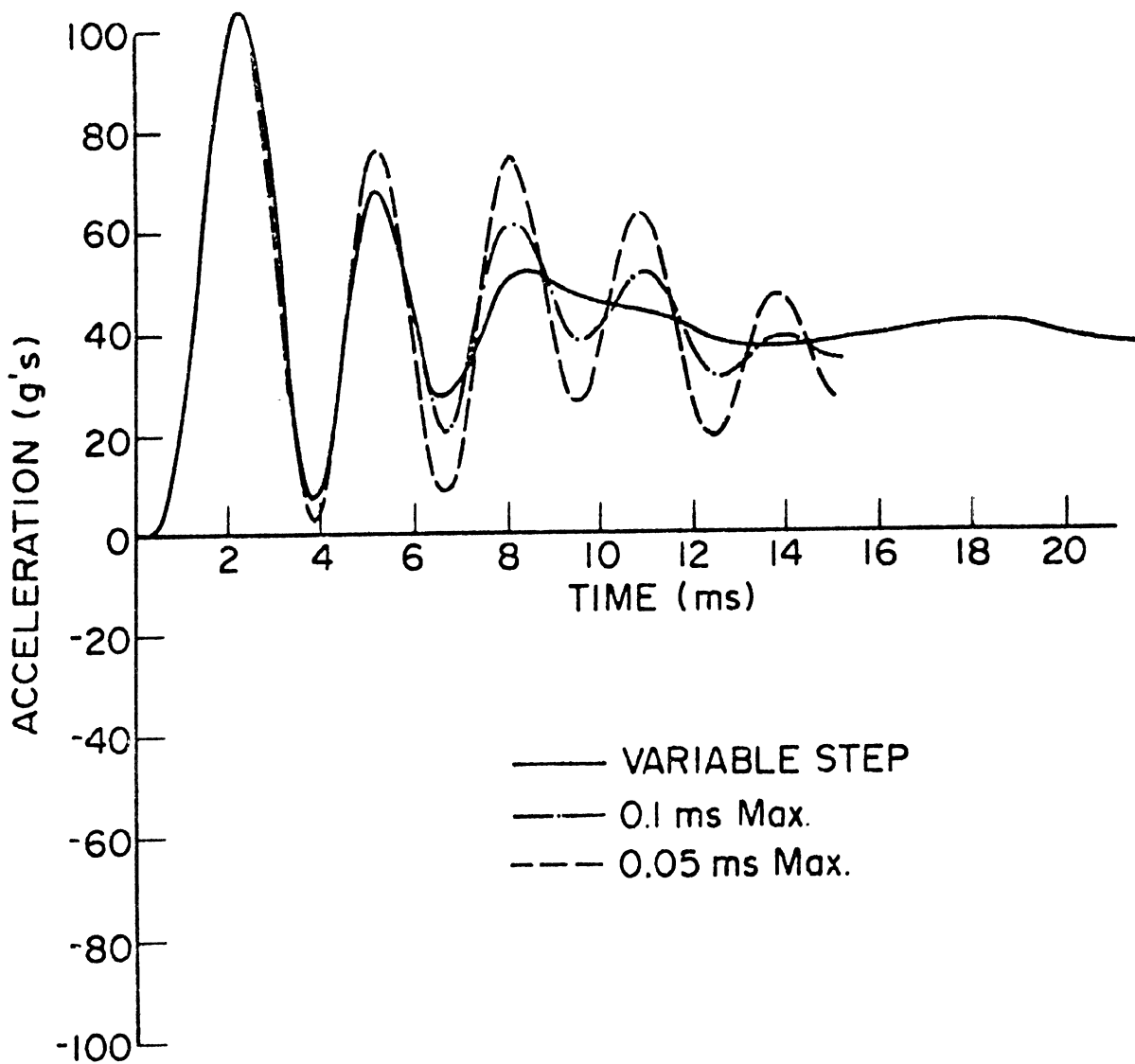


FIG. 23 COMPARISON OF FREQUENCY RESOLUTION FOR DIFFERENT TIME STEPS

5. Modeling Study of Dynamic Frame Test

5.1 Introduction

A modeling study was undertaken to explore the application of UMVCS-1 to an actual vehicle crash event. The event modeled was a barrier test conducted by Dynamic Science*. The test was a frontal impact of a 1968 Plymouth Fury with the forward sheet metal, radiator, grille, and engine all removed. A sketch of the test configuration and a schematic of the stub frame is shown in Fig. 24. Impact velocity was 30 MPH.

Although the structural configuration is relatively uncomplicated, the severe nature of the dynamic response made the simulation difficult. Due to the small inertia of the frame relative to the total vehicle mass, the frame rotated upwards with vertical velocities comparable to the longitudinal speed. Another modeling problem was the bumper supports. Due to rapid plastic buckling, they essentially lost all load carrying capacity within the first 5 ms of the 120 ms crash duration.

5.2 Simulation Model

The actual simulation model employed is shown in Fig. 25. The entire vehicle was treated as a single module consisting of a

* Dynamic Science Final Report, Contract No. DOT-HS-0462486, May, 1974.

frame component representing the stub frame and bumper supports and a rigid body component representing the remainder of the vehicle. Due to symmetry only half the vehicle was considered. The frame component is defined by ten node points with the nodal masses shown in the figure. Except for the bumper support, plastic hinge beam elements were employed between the nodes. Beam properties were computed from cross section dimensions. A Young's modulus of 30×10^6 psi, shear modulus of 12×10^6 psi and a yield stress of 36,000 psi were used for all members. Values of the initial yield and ultimate moments were calculated from beam theory for the cross sections. The other required plastic hinge parameters were obtained from extrapolation of the results reported in Appendix D**. Beam and hinge properties are summarized in Table 3.

The physical behavior of the vehicle in the contact region was modeled by an extensional spring mechanism and imposed constraints on nodes 8 and 10. A variety of kinematic constraints are available in UMVCS-1. In the present case the initial contact period is handled by bringing the contact node (node 10) to rest with a smooth (parabolic) deceleration pulse. After eight inches of relative crush between nodes 8 and 10 it is assumed that node 8 will begin to interact with the barrier through the crushed bumper supports. This interaction is handled by bringing node 8

** The subsequent tests of box and channel sections reported in Vol. 2 indicate that the assumed values are qualitatively correct.

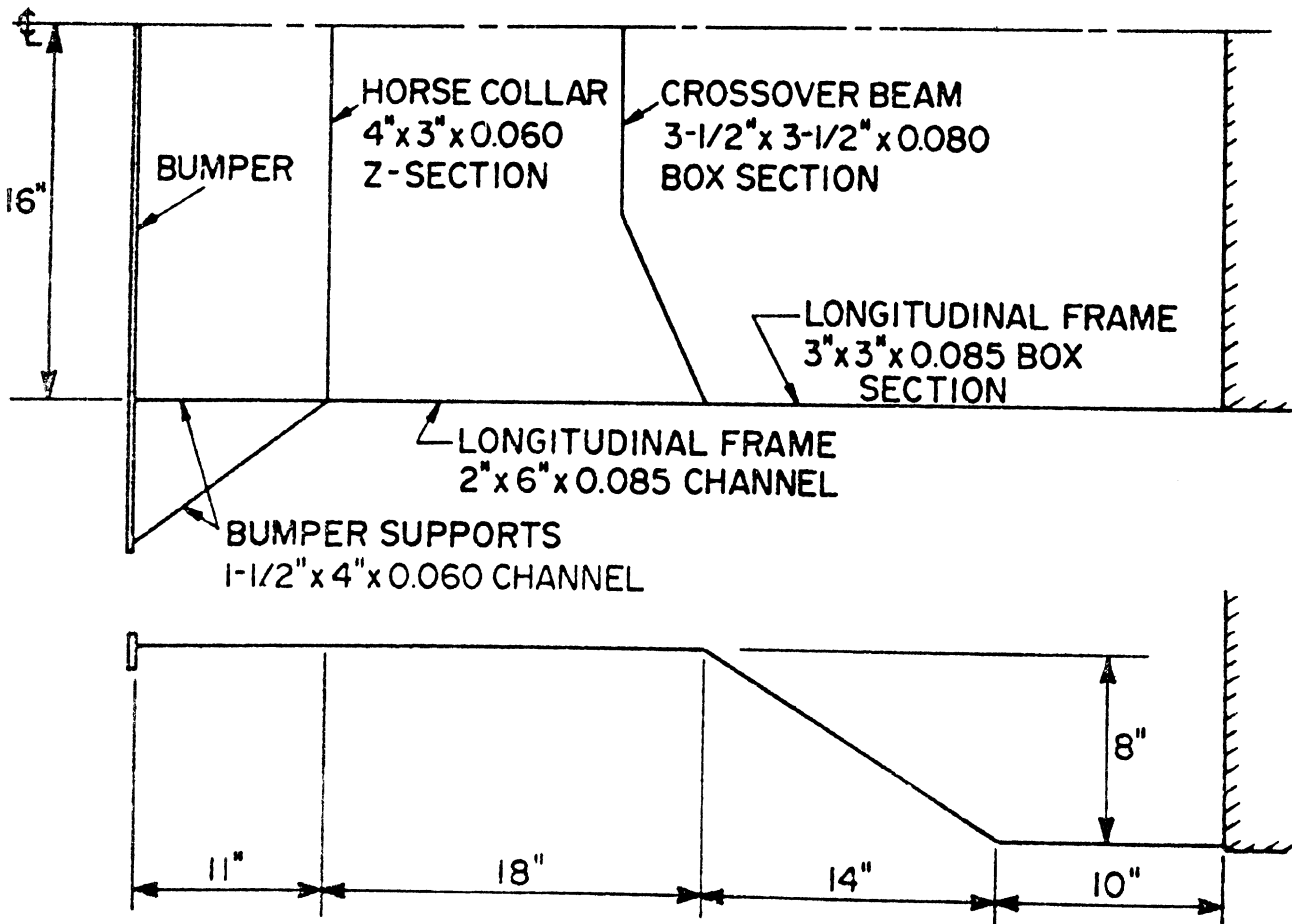
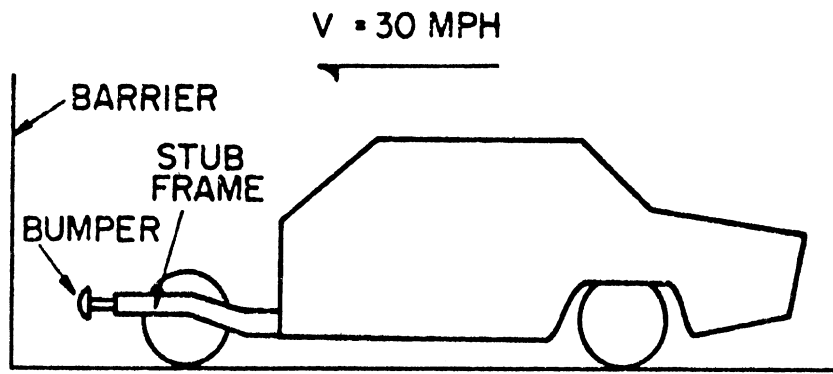


FIG. 24 SCHEMATIC OF DYNAMIC FRAME TEST

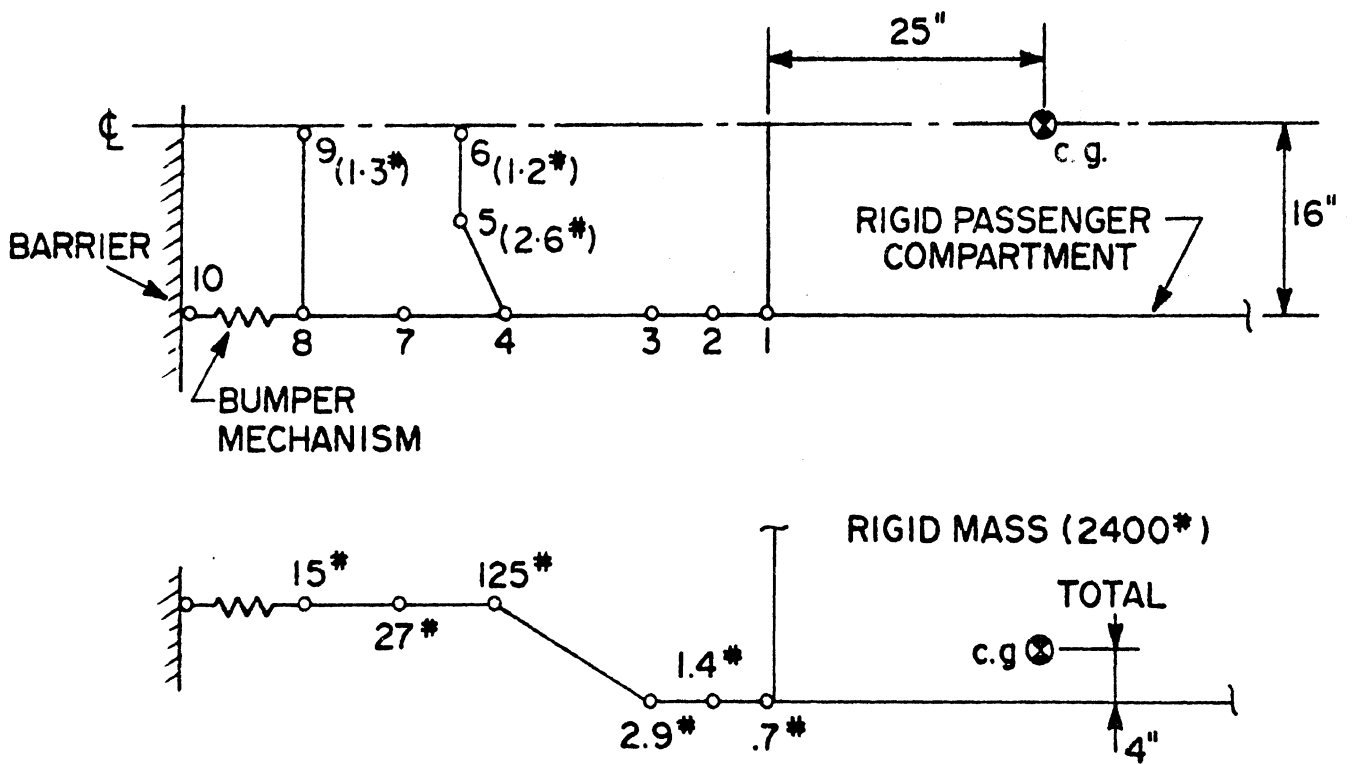


FIG. 25 SIMULATION MODEL

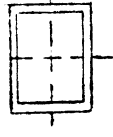
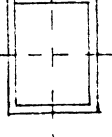
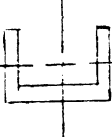
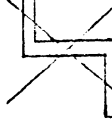
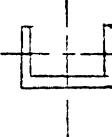
Cross Section Shapes	Section Properties			Hinge Properties							
	I ₁	I ₂	J	A	K ₁	K ₂	θ _m	B	f	M _o	Direction
 3x3x0.085	1.405	1.405	2.11	.991	31.	2.44	.15	.4	1.15	33714.	Bending in 1
					31.	2.44	.15	.4	1.15	33714.	Bending in 2
					-	5.0	0.	.3	1.0	26000.	Torsion
 3.5x3.5x0.08	2.13	2.13	3.2	1.095	32.	2.35	.15	.4	1.15	43913.	Bending in 1
					32.	2.35	.15	.4	1.15	43913.	Bending in 2
					-	5.0	0.	.3	1.0	33685	Torsion
 2x6x0.085	.2895	4.378	2.05x10 ⁻³	.9355	13.56	6.89	.15	.3	1.74	6854.	Bending in 1
					35.0	3.38	.15	.3	1.184	52530.	Bending in 2
					10.0	-	∞	1.0	1.5	4230.	Torsion
 4x3x0.06	.85	.091	5.04x10 ⁻⁴	.5928	7.05	5.14	.15	.3	1.4	13356.	Bending in 1
					11.8	6.34	.15	.3	1.62	4104.	Bending in 2
					10.0	-	∞	1.0	1.5	500.	Torsion
 1.5x4x0.06	.0864	.991	5.04x10 ⁻⁴	.413	28.	3.25	.15	.3	1.758	2700.	Bending in 1
					13.79	6.97	.15	.3	1.171	17834.	Bending in 2
					10.0	-	∞	1.	1.5	151.	Torsion
					1500.	-	∞	1.	1.33	11145.	Axial

TABLE 3. BEAM AND HINGE PROPERTIES

to rest in an additional crush distance of two inches.

During the eight inches of relative crush between nodes 8 and 10 the extensional mechanism was used to model the bumper supports. The force-deformation curve required to specify the mechanism was obtained by using the program to simulate a static crush test of the bumper support system. The computed result is shown by the dashed curve in Fig. 26. The solid curve is the piecewise linear approximation used in the dynamic simulation.

5.3 Comparison of Simulation and Test Results

Comparison between computed and test results for barrier force and acceleration of the passenger compartment c.g. are given in Fig. 27. The c.g. velocity is shown in Fig. 28. The barrier force and passenger compartment velocity show relatively good agreement between prediction and test over the first half of the crash duration. Although unsubstantiated, we believe that the marked increase in barrier force occurring around 70 ms reflects interaction of the front tire and suspension system with the barrier. This interpretation is consistent with the predicted longitudinal displacement of node 4. Thus here we will restrict our discussion to the first 40 ms of the event. Comparison of the velocity and acceleration on this time scale are shown in Figs. 29 and 30 respectively.

It appears that the simulation gives a good prediction of average values, but is less satisfactory in predicting frequency content and peak values. A possible explanation is the validity

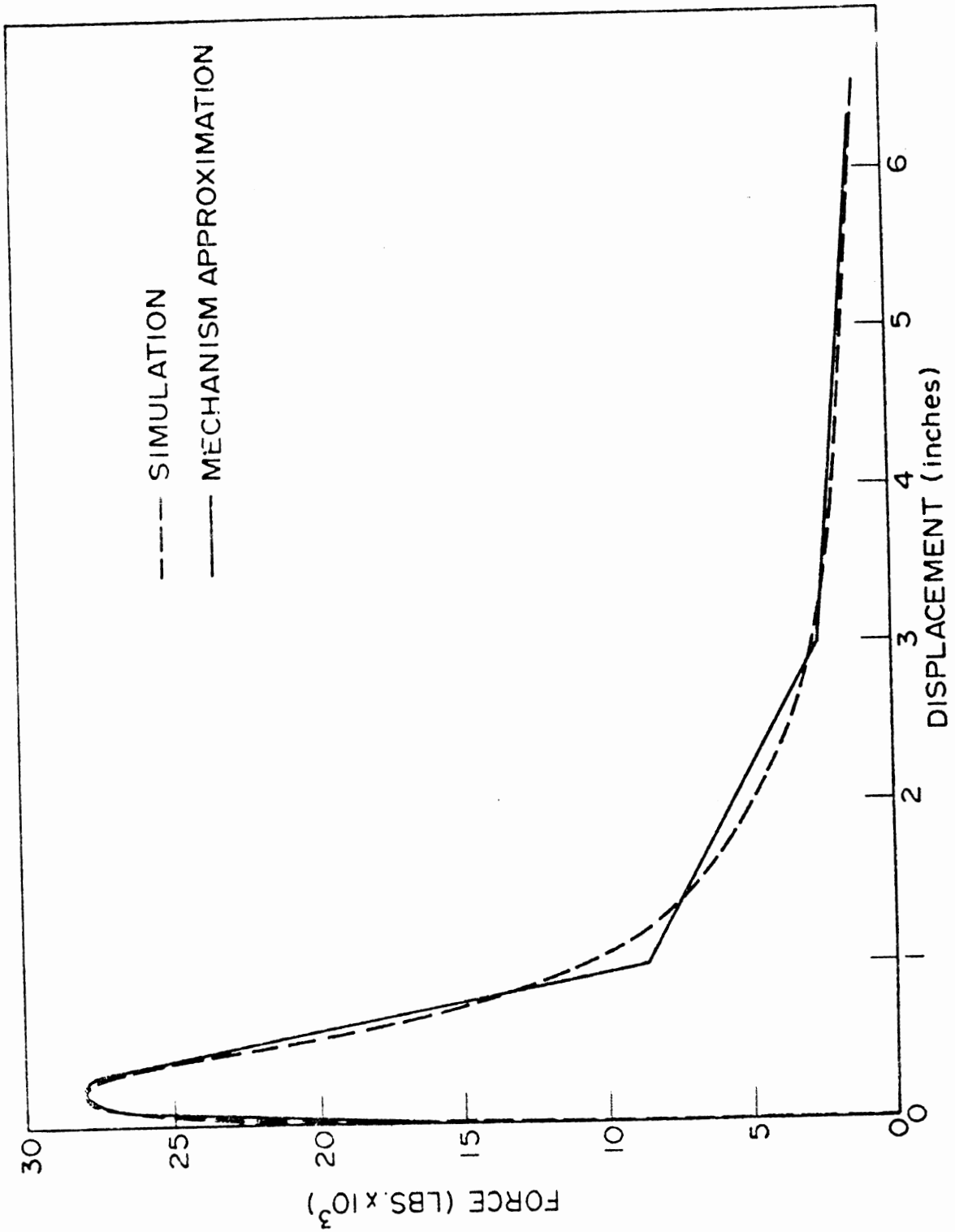


FIG. 26 BUMPER SUPPORT STATIC CRUSH TEST

of treating the passenger compartment as a rigid body. Given the large mass ratio of the compartment to the frame, it is somewhat anomalous to observe positive test acceleration. Thus the 50 Hz oscillation observed in the test acceleration may arise from elastic vibrations of the passenger compartment.

To test this hypothesis a second rigid body component was added to the model at the c.g. of the passenger compartment and connected by an elastic spring to the original rigid body. The mass and spring constant were chosen to give a natural frequency of 50 Hz. This insures, of course, a response at the observed frequency, but the response amplitude will depend upon the other components in the model. The predicted acceleration history is shown in Fig. 31. The agreement is sufficiently good to tentatively conclude that the simulation is predicting the dynamic force deformation characteristics of the vehicle structure.

Computations were carried out on The University of Michigan IBM 370/74 computer. The simulation required 270 time steps for the first 100 ms of the event. Total CPU time was 115 seconds.

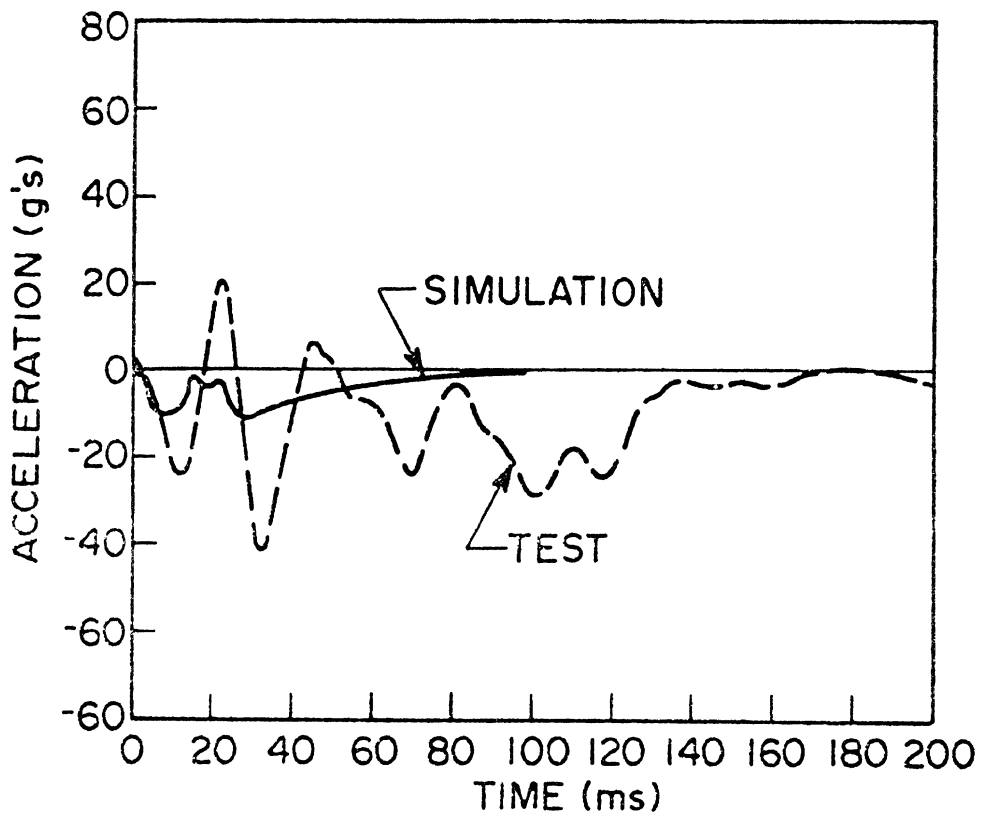
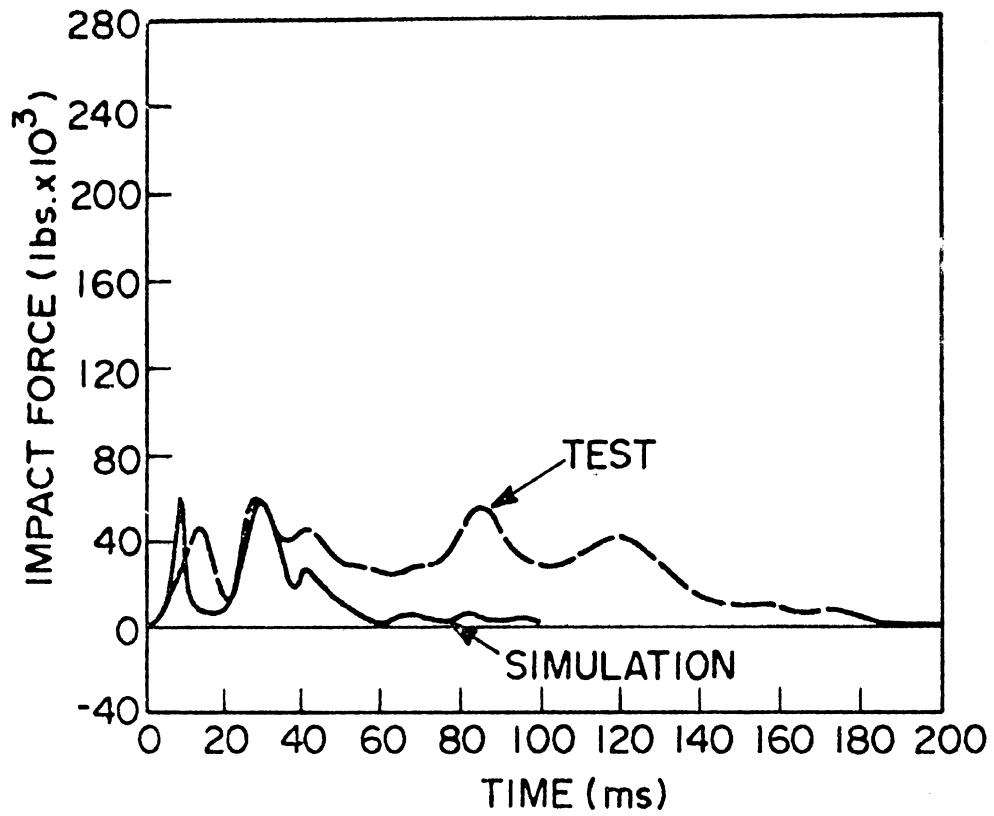


FIG. 27 BARRIER FORCE AND VEHICLE ACCELERATION

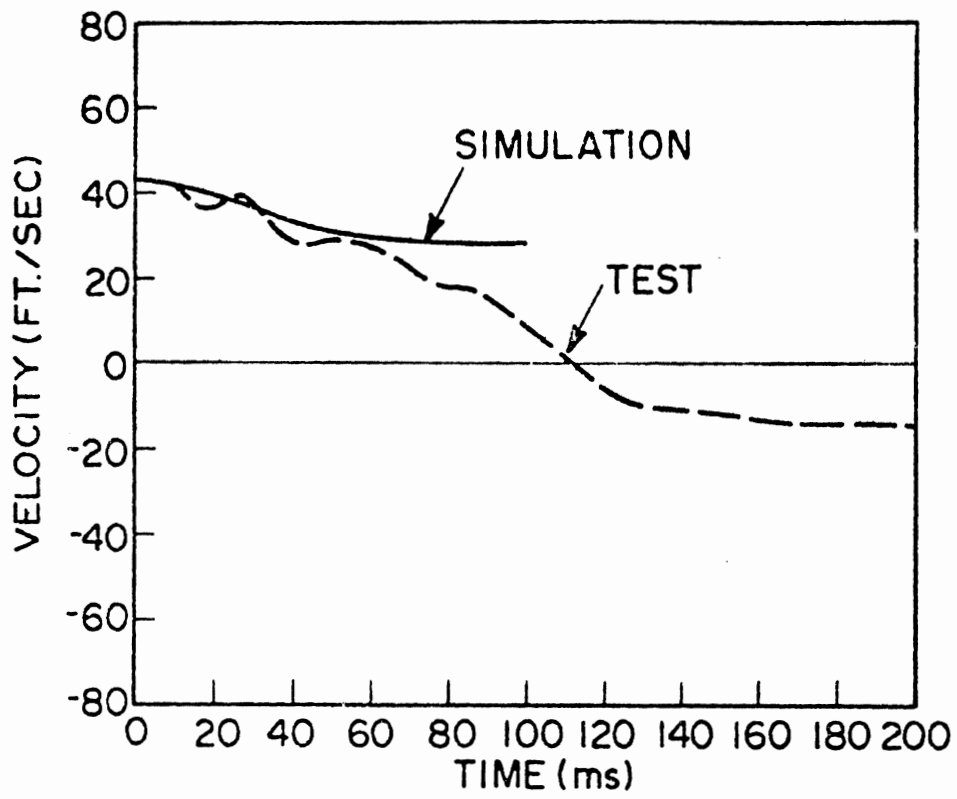


FIG. 28 VEHICLE VELOCITY

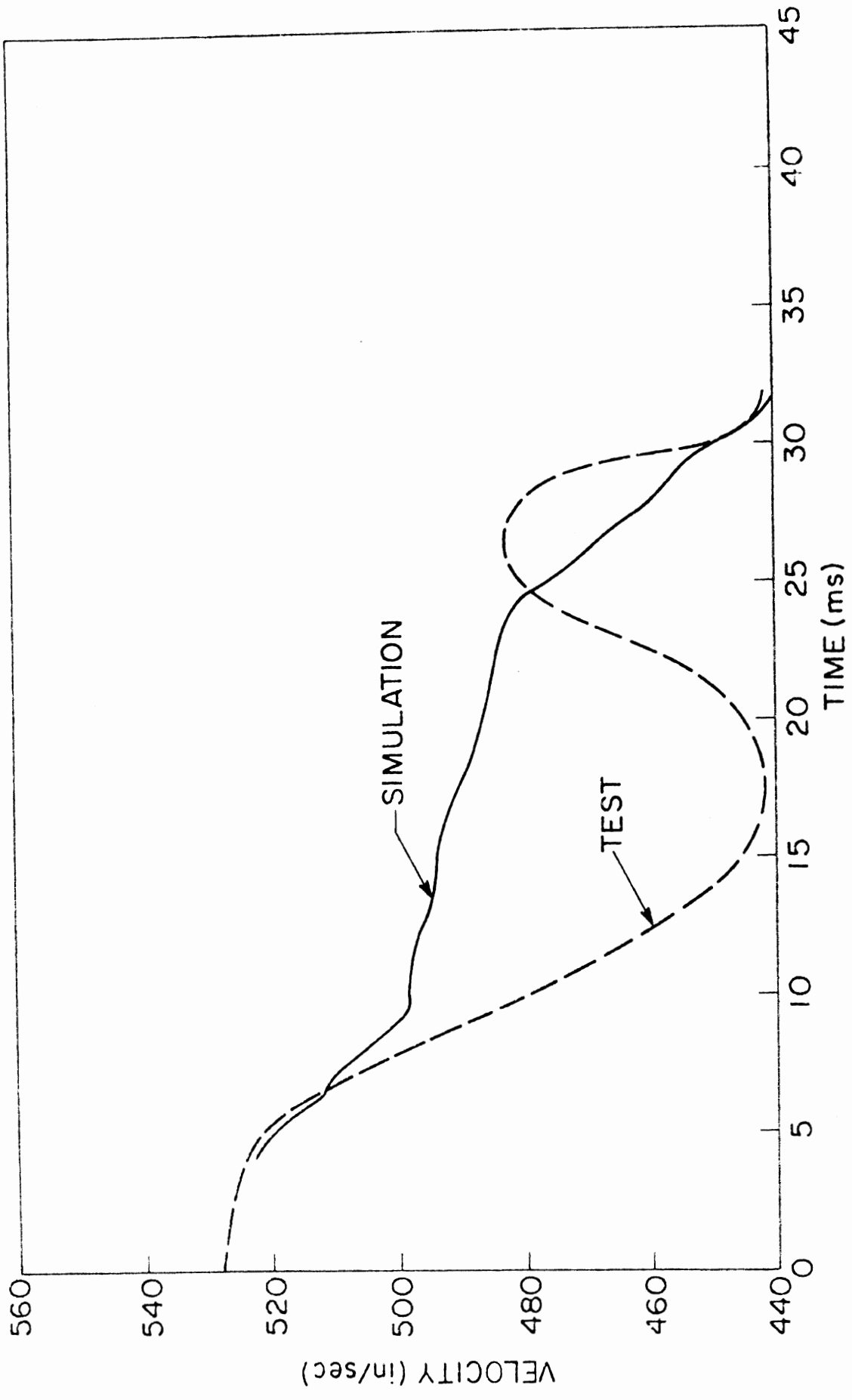


FIG. 29 VEHICLE VELOCITY FOR FIRST 40 MS

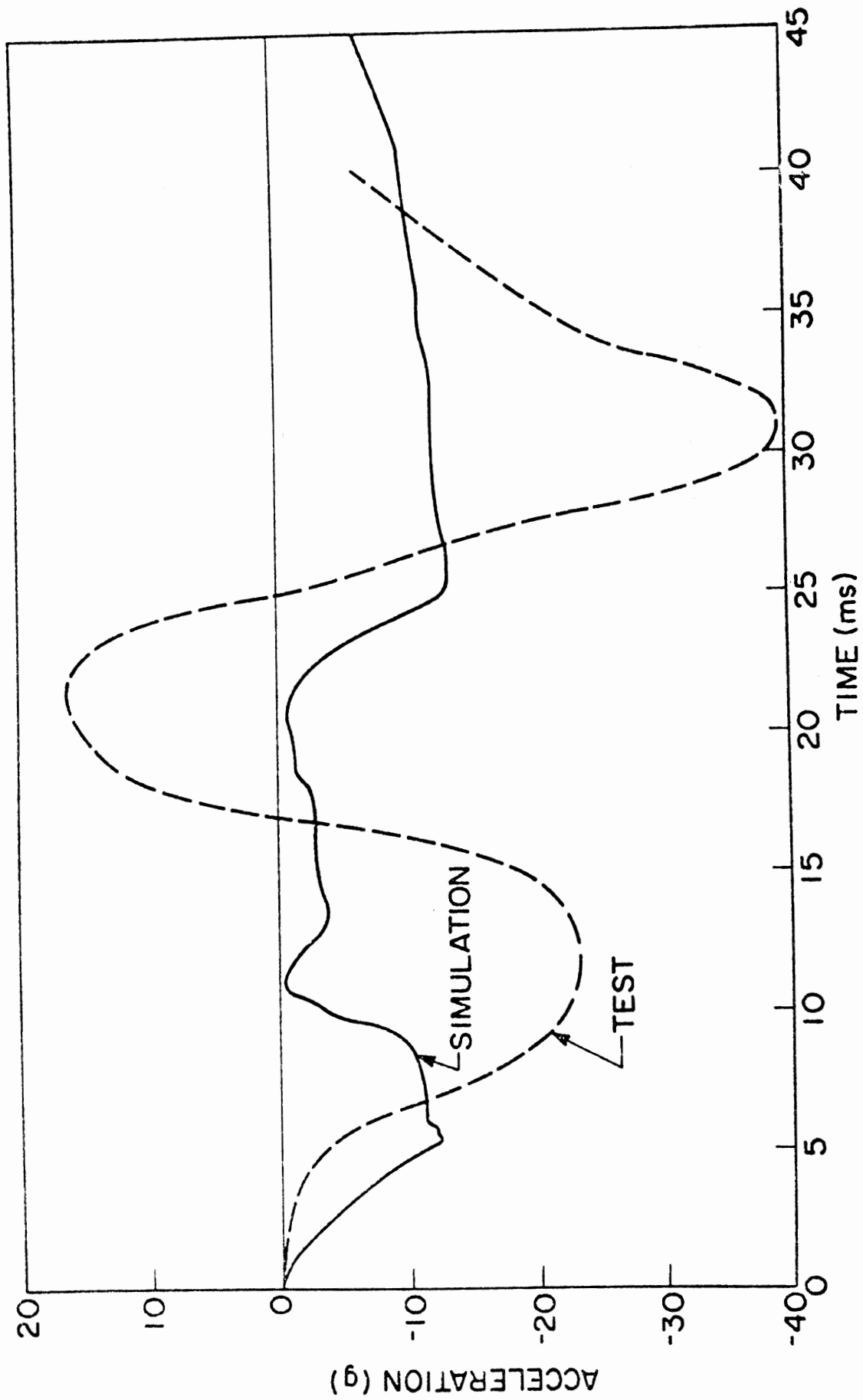


FIG. 30 VEHICLE ACCELERATION FOR FIRST 40 MS

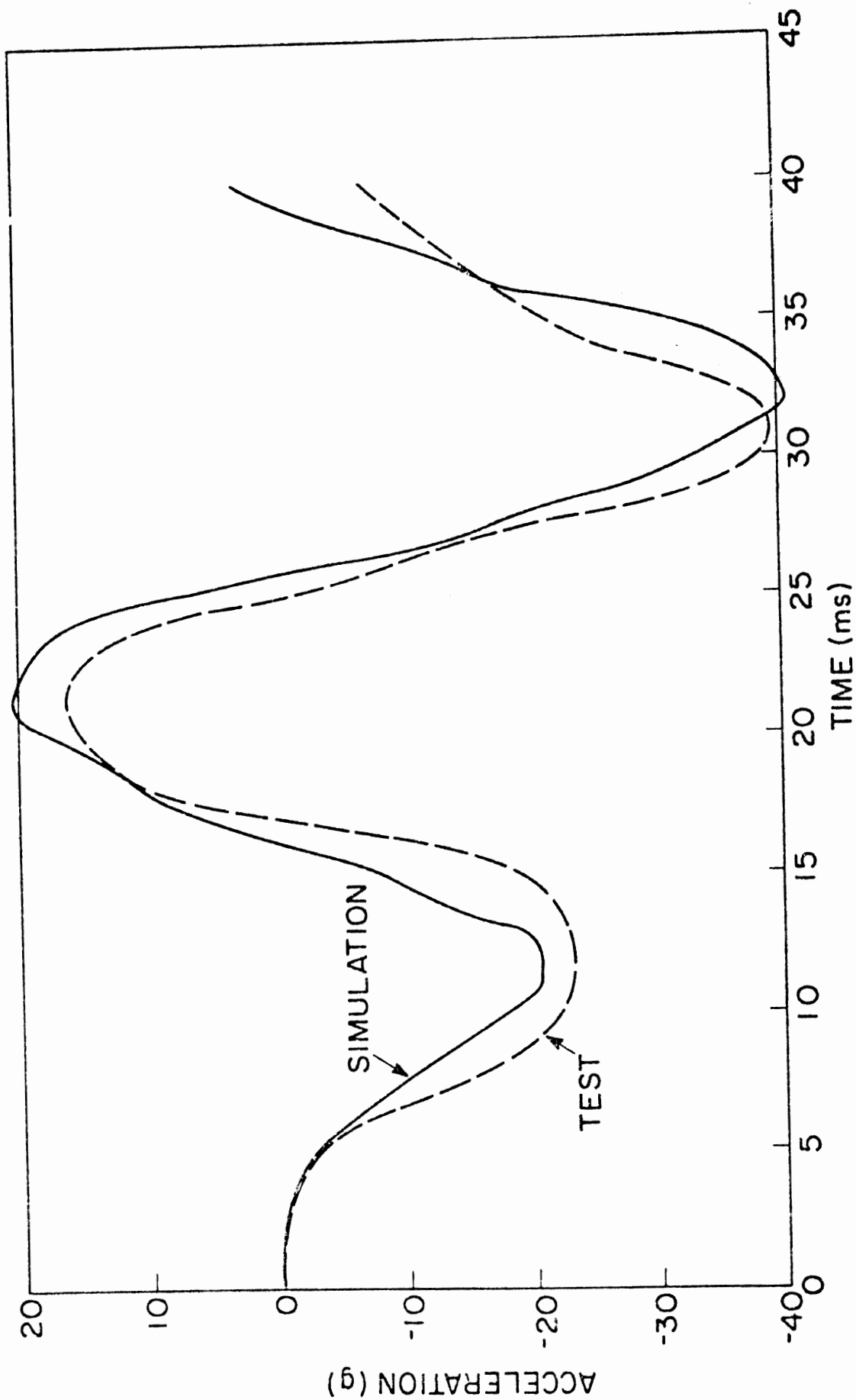


FIG. 31 ACCELERATION WITH ELASTIC COMPONENT

Appendix A

A Structural Theory for the Large Plastic Deformations of Beams

A.1 Introduction

Here we present a structural theory for the static analysis of large plastic deformations of space frames. The frame may consist of an arbitrary number of beam elements that are connected at node points. External loads are assumed concentrated at the nodes. For the frame structures contemplated plastic deformation is generally localized even at large deflections. Thus the present theory assumes that plastic deformation is confined to idealized hinges which may form at any node. The governing equations for a beam element are derived as a relation between generalized force rates and rates of kinematic variables associated with the nodes. It should be noted that the concept of a plastic hinge necessarily introduces discontinuities in the rotation and displacement rates, the discontinuities representing the plastic deformation rates. Thus some care must be taken in introducing appropriate nodal variables.

For the range of deformation contemplated here both open and closed thin wall beams typically exhibit local collapse of the cross section at the hinge. This local deformation significantly affects the overall structural behavior. This local deformation cannot, of course, be computed within the context of a structural theory. In Appendix D, however, it is shown that the reduced load carrying capacity can be accounted for by appropriate modification of the yield function. Constitutive equations for such "generalized plastic hinges" are developed in a later section.

A.2 Notation

We consider an elastic beam element which may form ideal plastic hinges at its end node points. The motion of the beam may consist of elastic deformation, rigid body motion of the node points, and rigid body motion of the beam relative to the node points due to plastic deformation at the hinges. The necessary reference frames for describing this motion are shown in Figure 2. The nodes are represented by point masses to which are fixed reference frames M_i and M_j . Two additional reference frames, denoted F_i and F_j , are fixed to the beam end points. The origin of these frames is at the shear center of the beam cross section; the x_3 axis is tangent to the beam axis and x_1 and x_2 are along the principal axes of the cross section. A subscript "o" denotes the initial position and orientation of the respective frames.

The positions of F_i and F_j with respect to the fixed global system are denoted by \underline{X}^i and \underline{X}^j respectively. Likewise the positions of M_i and M_j are denoted by \underline{Y}^i and \underline{Y}^j . The orientations of the four frames with respect to the global system are specified by the direction cosine matrices LM_i , LM_j , LF_i , LF_j respectively. The components of LF are

$$l_{ij} = \underline{e}_i \cdot \underline{e}_j^F \quad (1)$$

where \underline{e}_i^F and \underline{e}_j are the base vectors of the frame F and the global frame respectively.

In general we will use the notation \underline{v}^i for column matrices whose elements denote vector components. The superscript "i" is

denotes the node associated with the vector and the superscript "F" denotes the frame in which the vector components are expressed. If "F" is the global frame, the superscript will be suppressed.

Associated with each node we introduce the generalized displacement rate

$$\underline{\dot{D}}^i = \begin{bmatrix} \dot{\underline{u}}_i \\ \underline{\dot{\Omega}} \end{bmatrix} \quad (2)$$

where \underline{u} is the nodal displacement and $\underline{\Omega}$ the rotation rate of the node frame. We also introduce a generalized force rate associated with the beam element at the point i as

$$\underline{\dot{R}}^i = \begin{bmatrix} \dot{\underline{F}}_i \\ \underline{\dot{M}}_i \end{bmatrix} \quad (3)$$

where \underline{F}^i is the resultant force and \underline{M}^i the resultant couple acting on the beam at point i. The usual beam theory sign convention is employed.

With this we introduce the generalized displacement rate and force rate vectors for the beam element as

$$\underline{\dot{D}} = \begin{bmatrix} \dot{\underline{D}}^i \\ \dot{\underline{D}}^j \\ \underline{\dot{D}} \end{bmatrix}, \quad \underline{\dot{R}} = \begin{bmatrix} \dot{\underline{R}}^i \\ \dot{\underline{R}}^j \\ \underline{\dot{R}} \end{bmatrix} \quad (4)$$

Our immediate goal is to relate $\underline{\dot{R}}$ to $\underline{\dot{D}}$.

A.3 Kinematics of Deformation

Referring to Fig. A.1 we can visualize the deformation from the initial state to the current configuration as a rigid body motion of the beam frames F_i and F_j plus an elastic deformation. The rigid body motion may be due to both overall rigid body motion of the system and to plastic rotation and extension of the hinges at node i and/or node j.

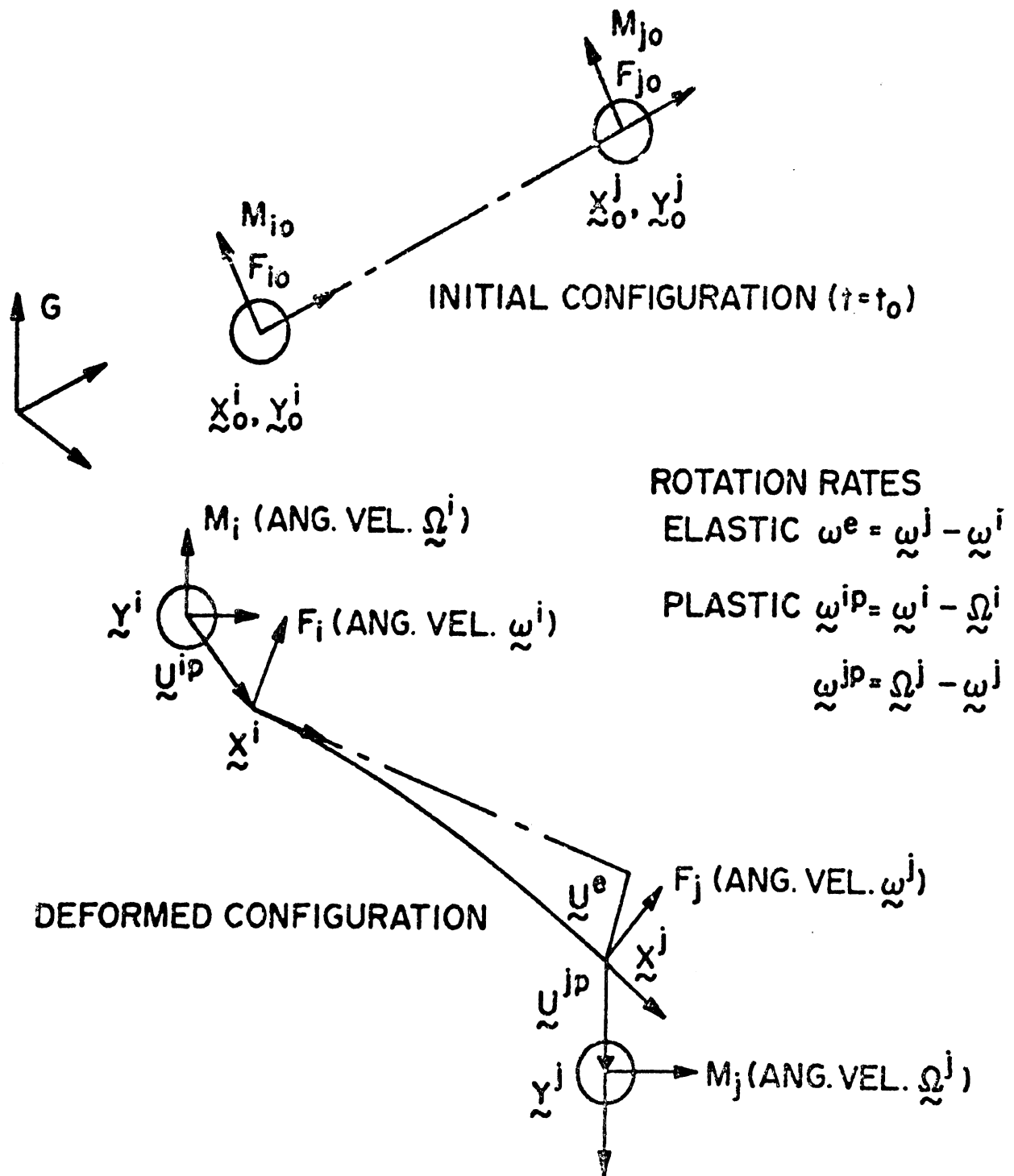


FIG. A.1 KINEMATICS OF DEFORMATION

In the deformed configuration the node frames are at $\underline{Y}^i, \underline{Y}^j$ and the beam frames at $\underline{X}^i, \underline{X}^j$ relative to the global frame.

The origins of beam and mass frames may differ by plastic displacements occurring at the hinges. Thus

$$\begin{aligned}\underline{X}^i &= \underline{Y}^i + \underline{U}^{ip} \\ \underline{X}^j &= \underline{Y}^j - \underline{U}^{jp}\end{aligned}\quad (5)$$

where \underline{U}^{ip} and \underline{U}^{jp} denote the plastic displacements referred to the global frame. Also

$$\underline{X}^j = \underline{X}^i + (LF_i)^T \underline{r} + \underline{U}^e \quad (6)$$

in which the superscript "T" denotes the transpose, \underline{U}^e is the elastic displacement of the end j with respect to the end i, and \underline{r} is the vector

$$\underline{r} = \ell \underline{i} = \ell \begin{bmatrix} 0 \\ 0 \\ 1 \end{bmatrix} \quad (7)$$

where ℓ is the beam length

In the initial configuration

$$\underline{X}_0^i = \underline{Y}_0^i, \quad \underline{X}_0^j = \underline{Y}_0^j \quad (8)$$

$$\underline{X}_0^j = \underline{X}_0^i + (LF_{i0})^T \underline{r}$$

Equations (5) through (8) can be combined to give

$$\underline{u}^j - \underline{u}^i = \left[(LF_i)^T - (LF_{i0})^T \right] \underline{r} + \underline{U}^e + \underline{U}^{ip} + \underline{U}^{jp} \quad (9)$$

where

$$\underline{u}^i = \underline{Y}^i - \underline{Y}_0^i, \quad \underline{u}^j = \underline{Y}^j - \underline{Y}_0^j \quad (10)$$

A rate equation for the node frame displacements is now obtained by differentiating (9). In carrying out the calculations we recall that

$$\dot{\underline{L}}\underline{F} = W(\underline{L}\underline{F}) \quad (11)$$

where W is the skew-symmetric rotation matrix

$$W = \begin{bmatrix} 0 & \omega_3 & -\omega_2 \\ -\omega_3 & 0 & \omega_1 \\ \omega_2 & -\omega_1 & 0 \end{bmatrix} \quad (12)$$

in which F_{ω_k} represent the components of the rotation rate of the F frame with respect to the F frame. With this it can be shown that

$$(\underline{L}\underline{F}_i)^T \underline{\dot{x}} = (\underline{H}\underline{R}) \underline{\omega}^i \quad (13)$$

where the 3×3 matrix $\underline{H}\underline{R}$ is defined in Sec. A.9 and $\underline{\omega}^i$ denotes the rotation rate of the F_i frame.

We also note that the plastic displacements are due to plastic extension of the beam. Thus the extension rate is always directed along the current x_3 axis of the beam frame, i.e.

$$\underline{F}_i \dot{\underline{u}}^{ip} = \dot{\underline{u}}^{ip} \underline{i}, \quad \underline{F}_j \dot{\underline{u}}^{jp} = \dot{\underline{u}}^{jp} \underline{i} \quad (14)$$

where $\dot{\underline{u}}^{ip}$ and $\dot{\underline{u}}^{jp}$ are the scalar axial plastic extension rates.

With this differentiating (9) yields

$$\dot{\underline{u}}^j - \dot{\underline{u}}^i = (\underline{H}\underline{R}) \underline{\omega}^i + (\underline{L}\underline{F}_i)^T \underline{i} \dot{\underline{u}}^{ip} + (\underline{L}\underline{F}_j)^T \underline{i} \dot{\underline{u}}^{jp} + \dot{\underline{u}}^e \quad (15)$$

A second kinematic equation is obtained by recognizing that the F_i and F_j beam frames differ only due to elastic deformation. Thus the beam frame rotation rates are related by

$$\underline{\omega}^j = \underline{\omega}^i + \underline{\omega}^e \quad (16)$$

in which $\underline{\omega}^e$ denotes the elastic rotation rate of the F_j frame relative to the F_i frame.

Finally we wish to express (15) and (16) in terms of the node frame rotation rates. The difference in orientation of the node and beam frames is due to plastic rotation at the hinges. Introducing the plastic rotation rates gives

$$\begin{aligned}\underline{\omega}^i &= \underline{\Omega}^i + \underline{\omega}^{ip} \\ \underline{\omega}^j &= \underline{\Omega}^j - \underline{\omega}^{jp}\end{aligned}\tag{17}$$

where the superscript "p" denotes the hinge rotation rate.

Using (17) to eliminate the beam frame rates in (15) and (16) yields

$$\begin{aligned}\dot{\underline{u}}^j - \dot{\underline{u}}^i - (HR)\underline{\Omega}^i &= (HR)\underline{\omega}^{ip} + (LF_i)^T \underline{i} \dot{U}^{ip} + (LF_j)^T \underline{i} \dot{U}^{jp} + \dot{U}^e \\ \underline{\Omega}^j - \underline{\Omega}^i &= \underline{\omega}^{ip} + \underline{\omega}^{jp} + \underline{\omega}^e\end{aligned}\tag{18}$$

The left hand sides of (18) involve components of the generalized displacement rate $\dot{\underline{D}}$, whereas the right hand sides involve the elastic deformation of the beam and the plastic deformation occurring at the nodes. It remains to relate these deformation quantities to the generalized forces acting on the beam at the node points.

A.4 Equilibrium

Introducing the generalized force defined in (3), the equations of equilibrium can be expressed as

$$F_i \underline{R}^i = (A + U) F_i \underline{R}^j\tag{19}$$

where A is the 6x6 constant matrix

$$A = \begin{bmatrix} I & | & 0 \\ \hline -E & | & I \end{bmatrix} \quad (20)$$

in which I is the 3x3 identity matrix and E is the 3x3 matrix

$$E = \ell \begin{bmatrix} 0 & 1 & 0 \\ -1 & 0 & 0 \\ 0 & 0 & 0 \end{bmatrix} \quad (21)$$

The 6x6 matrix U is a function of the elastic displacements.

It is

$$U = \begin{bmatrix} 0 & | & 0 \\ \hline UE & | & 0 \end{bmatrix} \quad (22)$$

in which

$$UE = \begin{matrix} F_i \\ \left[\begin{array}{ccc} 0 & -U_3 & U_2 \\ U_3 & 0 & -U_1 \\ -U_2 & U_1 & 0 \end{array} \right]^e \end{matrix} \quad (23)$$

We now obtain a rate equation by differentiating (19).

In carrying out this computation we must account for the change in orientation of the F_i frame. This is most conveniently done by expressing (19) in the global system.

We obtain

$$\underline{R}^i = (TF_i)^T (A+U) (TF_i) \underline{R}^j \quad (24)$$

where TF denotes the 6x6 transformation matrix

$$TF = \begin{bmatrix} LF & | & 0 \\ \hline 0 & | & LF \end{bmatrix} \quad (25)$$

It can be shown that

$$(TF_i)^T U (TF_i) = UG \quad (26)$$

where

$$UG = \begin{bmatrix} 0 & | & 0 \\ \hline UEG & | & 0 \end{bmatrix} \quad (27)$$

in which

$$UEG = \begin{bmatrix} 0 & -U_3 & U_2 \\ U_3 & 0 & -U_1 \\ -U_2 & U_1 & 0 \end{bmatrix} e \quad (28)$$

Also it follows from (25) and (11) that

$$\begin{aligned} \dot{TF} &= (TW)(TF) & (29) \\ (TF)^T &= -(TF)^T(TW) \end{aligned}$$

where TW is the 6x6 rotation matrix

$$TW = \begin{bmatrix} W & 0 \\ 0 & W \end{bmatrix} \quad (30)$$

Introducing (26) into (24), differentiating, and using (29) gives after some algebraic manipulation

$$\dot{R}^i = (TF_i)^T A (TF_i) \dot{R}^j + J_1 \dot{\omega}^i + (UG) \dot{R}^j + J_2 \dot{U}^e \quad (31)$$

The 6x3 matrices J_1 and J_2 involve the stress resultants at point j and are given in Sec. A.9. We now eliminate the beam frame rotation rate through (17). With this (31) becomes

$$\begin{aligned} J_1 \dot{\Omega}^i &= - \left[(TF_i)^T A (TF_i) + UG \right] \dot{R}^j + \dot{R}^i \\ &\quad - J_1 \dot{\omega}^{ip} - J_2 \dot{U}^e \end{aligned} \quad (32)$$

A.5 Constitutive Equations for Generalized Plastic Hinges

We must relate the plastic deformation rates in (18) and (32) to the generalized forces acting on the beam. As discussed in the Introduction local collapse of the beam cross section significantly affects the load carrying capacity of the hinge. This detailed behavior cannot, of course, be computed within the context of a structural theory.

Nevertheless it is shown in Appendix D that its effect on the load carrying capacity of the hinge has characteristic features that may be accounted for by the introduction of additional parameters in the generalized yield function. These "hinge parameters" are functions of the accumulated plastic deformation, and in the structural sense may be viewed as constitutive properties of the hinge. Their determination from standardized tests is discussed in Appendix D.

Here we develop appropriate constitutive equations for the i^{th} node. We assume the behavior of the hinge is determined by a scalar generalized yield function

$$f^i(\underline{\xi}^i) = 1 \quad (33)$$

where $\underline{\xi}^i$ are appropriate normalized stress resultants in the local beam coordinates. We assume that the yield function is independent of the transverse shear forces, and let Y_j^i ($j = 1, 2, 3, 4$), denote the last four elements of \underline{F}_{iR} . Thus

$$\xi_j^i = Y_j^i / \alpha_j \quad j = 1, 2, 3, 4 \quad (34)$$

The scaling parameters are considered as a four element vector of "hinge parameters".

We define

$$\sigma_j^0 = \int_0^{t_k} |\kappa_j^i| dt \quad , \quad j = 1, 2, 3, 4 \quad (35)$$

where κ_j^i are the elements of the plastic deformation rate vector

$$\underline{\kappa}^i = \int_{\underline{\omega}} \dot{U}^{ip} F_{i \underline{\omega}}^{ip} \quad (36)$$

Thus θ_j represents the accumulated plastic deformation in extension, biaxial bending, or torsion relative to the local beam boordinates. We now assume

$$\alpha_j = \alpha_j(\theta_j) \quad (37)$$

As shown in Appendix D the four functions (37) are characteristic of a given cross section and may be determined from standardized tests.

In effect $\underline{\alpha}$ changes the shape of the yield function in the physical stress resultant space. Alternatively the components of $\underline{\alpha}$ may be considered as "damage measures" which control the load carrying capacity of the hinge. From this viewpoint the assumption embodied in (37) is that the maximum principal moment, for example, is a function only of the accumulated plastic rotation about the corresponding principal axis. This is obviously a simplifying hypothesis, but appears reasonable during collapse of the cross section. Its validity for reverse plastic deformation is considerably more speculative. For the applications of interest, however, this is seldom an issue, i.e. once the cross section has collapsed we are usually not interested in reverse deformation. Finally it should be noted that the uncoupling of the damage measures inherent in (37) does not imply uncoupling of the stress resultants. In general their current value depends upon the entire deformation history.

To complete the analysis the plastic deformation rate is related to the yield function through a normality condition,* i.e. we postulate

$$\underline{\kappa}^i = \underline{a}^i \lambda^i \quad (38)$$

where λ^i is the scalar magnitude and \underline{a}^i is the normalized gradient

$$\underline{a}^i = \underline{\nabla} f^i / |\underline{\nabla} f^i| \quad (39)$$

in which $\underline{\nabla}$ is the gradient operator in the normalized stress resultant space. The scalar magnitude is determined from the condition

$$\dot{f}^i = 0 \quad (40)$$

It can be shown that (40) leads to

$$\lambda^i = \left[(GR^i) \dot{R}^i + (GB^i) \underline{\Omega}^i \right] \quad (41)$$

* It should be emphasized that this is a strong assumption since the usual stability arguments for normality are not necessarily applicable here.

where

$$\begin{aligned} GR^i &= -D^{-1} (MR) (TF_i)_R \\ GB^i &= -D^{-1} (MR) B^i (LF_i) \end{aligned} \quad (42)$$

in which D is the scalar

$$D = \left[(MR) (0; B^i) + MB \right] \underline{a}^i \quad (43)$$

In (42) the subscript R denotes the last four rows of the transformation matrix (25). The 4x3 matrix B^i depends upon the current generalized forces and is listed in the Appendix for reference. The 1x4 matrices MR and MB are

$$\begin{aligned} MR &= \begin{bmatrix} \frac{\partial f^i}{\partial Y_j^i} \end{bmatrix} \\ MB &= \begin{bmatrix} \frac{\partial f^i}{\partial \alpha_j} & \frac{\partial \alpha_j}{\partial \theta_j} & \text{sgn}(a_j^i) \end{bmatrix}, \quad j = 1, 2, 3, 4 \end{aligned} \quad (44)$$

where a_j^i is the j^{th} element of \underline{a}^i .

Substituting (41) into (38) gives the final result for the plastic deformation rates. It is convenient to partition (38) and express separately the extension rate and the plastic rotation rate in the global frame. Recalling (14) we obtain

$$\begin{aligned} \underline{\dot{U}}^{ip} &= (LF_i)^T \underline{\dot{U}}^{ip} = (EH^i) \underline{\dot{R}}^i + (EHB^i) \underline{\dot{\Omega}}^i \\ \underline{\dot{\omega}}^{ip} &= (HP^i) \underline{\dot{R}}^i + (HPB^i) \underline{\dot{\Omega}}^i \end{aligned} \quad (45)$$

where

$$\begin{aligned} EH^i &= (LF_i)^T \underline{a}_1^i (GR^i) \\ EHB^i &= (LF_i)^T \underline{a}_1^i (GB^i) \\ HP^i &= (LF_i)^T \underline{a}_R^i (GR^i), \quad HPB^i = (LF_i)^T \underline{a}_R^i (GB^i) \end{aligned} \quad (46)$$

in which the subscript R denotes the last three elements of \underline{a}^i .

Analogous relations may be derived for the node j . They may be obtained by replacing i with j in equations (33) through (46) and changing the signs of GR^i , GB^i , and MB in (42) and (43). The sign change occurs because of the kinematic definition of $\underline{\omega}^j$ in (17).

A.6 Elastic Deformation Rate Equations

We also need elastic constitutive relations expressed in rate form. From elastic beam theory we have relative to the current configuration beam frame F_i

$${}^{F_i} \underline{D}^e = (KE^{-1}) {}^{F_i} \underline{R}^j \quad (47)$$

where ${}^{F_i} \underline{D}^e$ is the generalized elastic displacement of the j end relative to the i end and KE^{-1} is the inverse of the elastic stiffness matrix (given for reference in Sec. A.9). A rate equation is obtained by differentiation. As in the equilibrium equations we must account for the rotation of the F_i frame. This introduces the rotation rate $\underline{\omega}^i$ which is eliminated through (17). Equation (45) is then used to eliminate $\underline{\omega}^{ip}$. After considerable algebraic manipulation, the final result expressed in the global frame is

$$\underline{\dot{D}}^e = (KT) \underline{\dot{R}}^j + (KRT) \underline{\dot{R}}^i + (KRTB) \underline{\Omega}^i \quad (48)$$

where

$$\begin{aligned} KT &= (TF_i)^T (KE^{-1}) (TF_i) \\ KRT &= (TF_i)^T (KR) (LF_i) HP^i \\ KRTB &= (TF_i)^T (KR) (LF_i) [I + HPB^i] \end{aligned} \quad (49)$$

in which KR is a 6x3 matrix depending upon the generalized forces and elements of the elastic stiffness matrix. It is given for reference in Sec. A.9.

A.7 Element Stiffness Matrix

Equations (18) and (32) represent twelve equations involving the twelve components of the generalized nodal displacement rate \underline{D} and the generalized force rate \underline{R} . We eliminate the elastic and plastic deformation rates in these equations through (48) and (45) respectively.

We obtain

$$\begin{aligned}
 & -\dot{\underline{u}}^i + \dot{\underline{u}}^j - \left[(\text{HR})(\text{I}+\text{HPB}^i) + \text{EHB}^i + (\text{KRTB})_{\text{U}} \right] \underline{\Omega}^i \\
 & -(\text{EHB}^j) \underline{\Omega}^j = \left[(\text{HR})(\text{HP}^i) + \text{EH}^i + (\text{KRT})_{\text{U}} \right] \dot{\underline{R}}^i \\
 & \quad + \left[\text{EH}^j + (\text{KT})_{\text{U}} \right] \dot{\underline{R}}^j \\
 & - \left[\text{I}+\text{HPB}^i + (\text{KRTB})_{\text{L}} \right] \underline{\Omega}^i + \left[\text{I}-\text{HPB}^j \right] \underline{\Omega}^j \\
 & = \left[\text{HP}^i + (\text{KRT})_{\text{L}} \right] \dot{\underline{R}}^i + \left[\text{HP}^j + (\text{KT})_{\text{L}} \right] \dot{\underline{R}}^j \\
 & \left[\text{J}_1 (\text{I}+\text{HPB}^i) + \text{J}_2 (\text{KRTB})_{\text{U}} \right] \underline{\Omega}^i \\
 & = \left[\text{I}-\text{J}_1 (\text{HP}^i) - \text{J}_2 (\text{KRT})_{\text{U}} \right] \dot{\underline{R}}^i \\
 & - \left[(\text{TF}_i)^T \text{A} (\text{TF}_i) + \text{UG} + \text{J}_2 (\text{KT})_{\text{U}} \right] \dot{\underline{R}}^j
 \end{aligned} \tag{50}$$

The subscripts U and L denote the upper three rows and the lower three rows respectively of the corresponding matrix.

Equations (50) have the matrix form

$$\text{H} \dot{\underline{R}} = \text{B} \dot{\underline{D}} \tag{51}$$

Thus

$$\dot{\underline{R}} = \text{K} \dot{\underline{D}} \tag{52}$$

where the "element stiffness matrix" is

$$\text{K} = \text{H}^{-1} \text{B} \tag{53}$$

A.8 Global Equations

A computer program for computing the large plastic deformation of general frames has been developed based on the above theory. The global frame equations are assembled in the usual way from consideration of equilibrium of the node points (expressed in rate form). External loads are assumed to be applied at the nodes. Displacement boundary conditions including imposed displacements are handled by contraction of the global matrix. The final system of equations has the form

$$(KG) \dot{\underline{U}} = \dot{\underline{F}} \quad (54)$$

where $\dot{\underline{U}}$ is the unknown generalized nodal displacement rate and $\dot{\underline{F}}$ is a known vector of loading and imposed displacement rates.

The analysis has been formulated as rate equations. For numerical solution (54) is expressed in incremental form. We let

$$\Delta \underline{U}_{-k+1} = \underline{U}(t_{k+1}) - \underline{U}(t_k) \quad (55)$$

$$\Delta \underline{F}_{-k+1} = \underline{F}(t_{k+1}) - \underline{F}(t_k)$$

Evaluating (54) at time t_k , replacing the derivatives by forward differences, and using (55) then gives

$$[KG(t_k)] \Delta \underline{U}_{-k+1} = \Delta \underline{F}_{-k+1} \quad (56)$$

After each forward step the matrix KG must be updated. In particular we must update the direction cosine matrices defining the beam reference frames. For this purpose we approximate \dot{LF} by

$$\dot{LF}(t_k) = [LF(t_{k+1}) - LF(t_k)] / \Delta t \quad (57)$$

Also we introduce the incremental rotation vector

$${}^F \underline{\Delta \theta} = {}^F \underline{\omega} \Delta t \quad (58)$$

Introducing (57) into (11), multiplying through by Δt , and using (58) then yields

$$LF(t_{k+1}) = (WB) LF(t_k) \quad (59)$$

where

$$WB = {}^F \begin{bmatrix} 1 & \Delta\theta_3 & -\Delta\theta_2 \\ -\Delta\theta_3 & 1 & \Delta\theta_1 \\ \Delta\theta_2 & -\Delta\theta_1 & 1 \end{bmatrix} \quad (60)$$

The use of the approximation (58) implies that $||\Delta\theta||^2$ is small compared to unity. Basically this requirement is used to determine the step size of the incremental process.

Although the analysis leading to (52) is the fundamental basis of the computer program, there are additional considerations which must be implemented in the program development. The stiffness matrix was derived on the basis that the plastic hinges at the beam nodes are operating. If the hinge is not operating, the plastic contribution can be eliminated by

setting the GR and GB matrices associated with the node to zero.

It is necessary, however, to monitor in the program the operation of the hinges. Initially the GR and GB matrices are set to zero. At the end of each forward integration step, the yield function f is computed at each node. If it is less than unity, the computation proceeds to the next step. If it exceeds unity at some node, the step size is reduced until the yield function is satisfied. At the next step the GR and GB matrices for the appropriate node are included in the computation.

Elastic unloading is included by monitoring the rate of energy dissipation at the hinge. The dissipation rate is

$$d = (\underline{Y})^T \underline{K} \quad (61)$$

At each time step d is computed from (61). If $d > 0$, the computation proceeds to the next step. If $d < 0$, the GR and GB matrices for that node are set to zero before proceeding.

A.9 Summary of Equations

In the following we list for completeness the various matrices arising in the derivation. The 3x3 orientation matrix HR is

$$HR = (LF_i)^T E (LF_i) \quad (A1)$$

where

$$E = \ell \begin{bmatrix} 0 & 1 & 0 \\ -1 & 0 & 0 \\ 0 & 0 & 0 \end{bmatrix} \quad (A2)$$

The 6x3 matrices J_1 and J_2 in the equilibrium equations (31) are

$$J_1 = \begin{bmatrix} 0 \\ \dots \\ JR_1 \end{bmatrix}, \quad J_2 = \begin{bmatrix} 0 \\ \dots \\ JR_2 \end{bmatrix} \quad (A3)$$

where the 3x3 matrices are

$$JR_1 = (LF_i)^T JB (LF_i) \quad (A4)$$

in which

$$JB = \ell \begin{bmatrix} F_i & -R_3 & 0 & 0 \\ 0 & -R_3 & 0 & 0 \\ R_1 & R_2 & 0 & 0 \end{bmatrix}^j \quad (A5)$$

and

$$JR_2 = \begin{bmatrix} 0 & R_3 & -R_2 \\ -R_3 & 0 & R_1 \\ R_2 & -R_1 & 0 \end{bmatrix}^j \quad (A6)$$

The 4x3 matrix B^i appearing in (42) is

$$B^i = \begin{bmatrix} -R_2 & R_1 & 0 \\ 0 & -R_6 & R_5 \\ R_6 & 0 & -R_4 \\ -R_5 & R_4 & 0 \end{bmatrix}^i \quad (A7)$$

The elastic complacance matrix in (47) is

$$KE^{-1} = \begin{bmatrix} k_1 & 0 & 0 & 0 & k_7 & 0 \\ 0 & k_2 & 0 & k_8 & 0 & 0 \\ 0 & 0 & k_3 & 0 & 0 & 0 \\ 0 & k_8 & 0 & k_4 & 0 & 0 \\ k_7 & 0 & 0 & 0 & k_5 & 0 \\ 0 & 0 & 0 & 0 & 0 & k_6 \end{bmatrix} \quad (A8)$$

in which

$$\begin{aligned} k_1 &= \ell^3/3EI_2, \quad k_2 = \ell^3/3EI_1, \quad k_3 = \ell/EA \\ k_4 &= \ell/EI_1, \quad k_5 = \ell/EI_2, \quad k_6 = \ell/GJ \\ k_7 &= \ell^2/2EI_2, \quad k_8 = -\ell^2/2EI_1 \end{aligned} \quad (A9)$$

where E is the elastic modulus, G is the shear modulus, I_1 and I_2 are the principal moments of inertia, A is the cross section area, J is the polar moment of inertia, and ℓ is the

beam length. The 6x3 matrix KR in (49) is

$$\text{KR} = \begin{matrix} & \begin{matrix} \text{F}_i & \text{---} & & & & \text{---} & \text{j} \end{matrix} \\ \begin{matrix} \text{---} \\ \text{---} \\ \text{---} \\ \text{---} \\ \text{---} \\ \text{---} \end{matrix} & \begin{bmatrix} k_7 R_6 & -(k_1 - k_3) R_3 & (k_1 - k_2) R_2 - (k_7 + k_8) R_4 \\ (k_2 - k_3) R_3 & -k_8 R_6 & (k_1 - k_2) R_1 + (k_7 + k_8) R_5 \\ (k_2 - k_3) R_2 + k_8 R_4 & -(k_1 - k_3) R_1 - k_7 R_5 & 0 \\ k_8 R_3 & -(k_4 - k_6) R_6 & -(k_8 + k_7) R_1 + (k_4 - k_5) R_5 \\ (k_5 - k_6) R_6 & -k_7 R_3 & (k_4 - k_5) R_4 + (k_7 + k_8) R_2 \\ (k_5 - k_6) R_5 + k_7 R_1 & -(k_4 - k_6) R_4 - k_8 R_2 & 0 \end{bmatrix} \end{matrix}$$

Appendix B

Incremental Equations for Rigid Body Component

B.1 Introduction

In this Appendix the governing equations for the rigid body mass module are derived. They are, of course, based on the well known equations of rigid body dynamics. For application here, however, there are a number of points that require careful consideration. First of all the equations must be expressed in incremental form to be compatible with the frame components. This is a nontrivial exercise, particularly for the angular momentum equation. Next the equations must hold for external forces and moments applied at arbitrary nodes on the rigid body.

We consider the rigid body with mass m . The center of gravity is at point F with coordinates \tilde{x}^F relative to the global coordinate system. Forces \tilde{F}^i and couples \tilde{M}^i are applied at points $i = 1, 2, \dots, p$ on the mass. The local axes at F are taken to be principal inertial axes.

B.2 Linear Momentum

In vector form the incremental linear momentum equation at time k is

$$m \frac{\Delta \tilde{x}^F}{k+1} = \sum_{i=1}^p \frac{\Delta F^i}{k+1} \quad (1)$$

where

$$\frac{\ddot{\underline{x}}^F}{k+1} = \frac{\ddot{\underline{x}}^F}{k+1} - \frac{\ddot{\underline{x}}^F}{k} \quad (2)$$

$$\frac{\Delta F^i}{k+1} = \frac{F^i}{k+1} - \frac{F^i}{k}$$

We introduce the displacements of the center of mass as

$$\underline{v}^F = \underline{x}^F - \underline{x}^{F0} \quad (3)$$

where \underline{x}^{F0} is the initial value of the position vector. With (3)

the momentum equation (1) may be written as

$$m \text{ I } \frac{\ddot{\underline{v}}^F}{k+1} = \hat{\text{I}} \frac{\Delta F}{k+1} \quad (4)$$

where $\hat{\text{I}}$ is the 3 x 3 matrix

$$\hat{\text{I}} = [\text{I} \quad \text{I} \quad \dots \quad \text{I}]$$

in which I is the 3 x 3 identity matrix. The vector $\underline{\Delta F}$ has 3p elements consisting of the force components applied to the rigid body, i.e.

$$\underline{F} = \begin{bmatrix} \underline{\Delta F}^1 \\ \underline{\Delta F}^2 \\ \underline{\Delta F}^p \end{bmatrix} \quad (6)$$

We next replace the acceleration increment by a variable step backward difference approximation.

From Chapter 2 we have

$$\frac{\ddot{\underline{v}}^F}{k+1} = h_1 \frac{\Delta \underline{v}^F}{k+1} - h_2 \frac{\Delta \underline{v}^F}{k} + h_3 \frac{\Delta \underline{v}^F}{k-1} \quad (7)$$

where

$$\begin{aligned}
 h_1 &= \frac{\Delta t^{-2}}{k+1} \\
 h_2 &= (\Delta t_{k+1} + \Delta t_k) (\Delta t_{k+1} \Delta t_k^2)^{-1} \\
 h_3 &= \Delta t_k^{-1} \Delta t_{k-1}^{-1}
 \end{aligned} \tag{8}$$

Substituting (7) into (4) gives the linear momentum equation in the form.

$$mh_1 \int \frac{\Delta v^F}{k+1} - mh_2 \int \frac{\Delta v^F}{k} + mh_3 \int \frac{\Delta v^F}{k-1} = \hat{I} \frac{\Delta F}{k+1} \tag{9}$$

B.3 Angular Momentum

With respect to the global inertial reference frame, the angular momentum equation is

$$\dot{\underline{H}} = \underline{M}_r \tag{10}$$

where \underline{H} is the angular momentum of the mass and \underline{M}_r is the resultant moment about the center of mass. We also have

$$\underline{H} = L^T ({}^F \underline{H}) \tag{11}$$

where ${}^F \underline{H}$ is the angular momentum expressed in the local body frame and L^T is the transpose of the direction cosine matrix relating the local and global frames.

Differentiating (11) gives

$$\dot{\underline{H}} = L^T ({}^F \dot{\underline{H}}) + \dot{L}^T ({}^F \underline{H}) \tag{12}$$

We have

$$\dot{L}^T = -L^T ({}^F \hat{W}) \tag{13}$$

where

$$\hat{F}_W = \begin{bmatrix} 0 & F_{\omega_3} & -F_{\omega_2} \\ -F_{\omega_3} & 0 & F_{\omega_1} \\ F_{\omega_2} & -F_{\omega_1} & 0 \end{bmatrix} \quad (14)$$

in which F_{ω_i} are the components of the angular velocity vector expressed in the local frame. Using (12) and (13), equation (10)

becomes
$$\dot{F}_H - \hat{F}_W (F_H) = L M_r = F_{M_r} \quad (15)$$

where F_{M_r} is the resultant moment expressed in the local frame. It is

where
$$F_{M_r} = \sum_{i=1}^P F_{M_i} + \sum_{i=1}^P (F_{r_{i/F}} \times F_{F_i}^i) \quad (16)$$

where "X" denotes the vector cross product and $F_{r_{i/F}}$ is the position vector of the point i with respect to the center of mass in the local frame.

We note that

$$F_{r_{i/F}} \times F_{F_i}^i = C_{i/F} \begin{bmatrix} F_x \\ F_y \\ F_z \end{bmatrix}^i \quad (17)$$

where $C_{i/F}$ is the constant matrix

$$C_{i/F} = \begin{bmatrix} 0 & -z_{i/F} & y_{i/F} \\ z_{i/F} & 0 & -x_{i/F} \\ -y_{i/F} & x_{i/F} & 0 \end{bmatrix} \quad (18)$$

In (18) the elements are the coordinates of the ith node with respect to the rigid body frame F.

Thus with (16) and (17), equation (15) becomes

$$\dot{\underline{H}} = \underline{F}_W (\underline{F}_H) = \sum_{i=1}^P \underline{M}^i + \sum_{i=1}^P C_{i/F} \underline{F}_F^i \quad (19)$$

The frame F is oriented along the principal axes and is fixed to the body. Thus

$$\underline{F}_H = \text{II} \underline{F}_\omega = \text{II} \underline{L} \underline{\omega} \quad (20)$$

where II is the inertia tensor

$$\text{II} = \begin{bmatrix} I_{xx} & 0 & 0 \\ 0 & I_{yy} & 0 \\ 0 & 0 & I_{zz} \end{bmatrix} \quad (21)$$

Differentiating (20) gives

$$\dot{\underline{H}} = \text{II} (\underline{L}\dot{\underline{\omega}} + \dot{\underline{L}}\underline{\omega}) = \text{II} \underline{L}\dot{\underline{\omega}} \quad (22)$$

since it may be shown that

$$\dot{\underline{L}}\underline{\omega} = 0 \quad (23)$$

Substituting (22) into (19) and expressing the result in the global frame gives the angular momentum equation

$$\underline{L}^T \text{II} \underline{L} \dot{\underline{\omega}} + \dot{\underline{L}}^T \text{II} \underline{L} \underline{\omega} = \sum_{i=1}^P \underline{M}^i + \sum_{i=1}^P \underline{L}^T C_{i/F} \underline{L}_F^i \quad (24)$$

We obtain the necessary incremental equation by differentiating (24). Writing the result at time k and introducing the global rotation increment

$$\frac{\Delta \Omega^F}{k+1} = \frac{\underline{\omega}}{k} \Delta t_{k+1} \quad (25)$$

gives the incremental equation

$$\begin{aligned}
 & [L^T \text{ II } L]_k \frac{\Delta \ddot{\Omega}^F}{k+1} + [L^T \text{ II } \dot{L} + 2L^T \text{ II } L]_k \frac{\Delta \dot{\Omega}^F}{k+1} \\
 & + [L^T \text{ II } L - \sum_{i=1}^P L^T (F_{F^i}^{\wedge} C_{i/F}) L]_k \frac{\Delta \Omega^F}{k+1} \\
 & = \sum_{i=1}^P [L^T C_{i/F} L]_k \frac{\Delta F^i}{k+1} + \sum_{i=1}^P \frac{\Delta M^i}{k+1}
 \end{aligned} \tag{26}$$

In (26) the matrices $F_{F^i}^{\wedge}$ are

$$F_{F^i}^{\wedge} = \begin{bmatrix} 0 & -F_{F^i}^z & F_{F^i}^y \\ F_{F^i}^z & 0 & -F_{F^i}^x \\ F_{F^i}^y & F_{F^i}^x & 0 \end{bmatrix} \tag{27}$$

The derivatives in (26) must now be expressed by backward difference approximations. For this purpose we introduce the notation

$$\begin{aligned}
 \hat{\alpha}_k &= [L^T \text{ II } L]_k = L_k^T \text{ II } L_k \\
 \hat{\beta}_k &= [L^T \text{ II } \dot{L} + 2L^T \text{ II } L]_k
 \end{aligned} \tag{28}$$

$$\begin{aligned}
 & = \Delta t^{-1} [3L_k^T \text{ II } L_k - L_k^T \text{ II } L_{k-1} - 2L_{k-1}^T \text{ II } L_k] \\
 \hat{\gamma}_k &= [L^T \text{ II } L - \sum_{i=1}^P L^T (F_{F^i}^{\wedge} C_{i/F}) L]_k \\
 & = h_4 L_k^T \text{ II } L_k - h_5 L_{k-1}^T \text{ II } L_k + h_6 L_{k-2}^T \text{ II } L_k \\
 & - \sum_{i=1}^P [L_k^T (F_{F^i}^{\wedge} C_{i/F}) L_k]
 \end{aligned}$$

in which

$$\begin{aligned}
 h_4 &= \Delta t_k^{-2} \\
 h_5 &= (\Delta t_{k-1} + \Delta t_k) (\Delta t_k^2 \Delta t_{k-1})^{-1} \\
 h_6 &= (\Delta t_k \Delta t_{k-1})^{-1}
 \end{aligned} \tag{29}$$

Introducing (28) into (26) and using the acceleration approximation (7) gives the incremental angular momentum equations as

$$\begin{aligned}
 [h_1 \hat{\alpha}_k + \Delta t_{k+1}^{-1} \hat{\beta}_k + \hat{\gamma}_k] \underline{\Delta \Omega}_{k+1}^F - [h_2 \hat{\alpha}_k + \Delta t_k^{-1} \hat{\beta}_k] \underline{\Delta \Omega}_k^F \\
 + h_3 \hat{\alpha}_k \underline{\Delta \Omega}_{k-1}^F = \sum_{i=1}^P \underline{\Delta M}_{k+1}^i + \sum_{i=1}^P \alpha_{i/k} \underline{\Delta F}_{k+1}^i
 \end{aligned} \tag{30}$$

in which

$$\alpha_{i/k} = L_k^T C_{i/F} L_k \tag{31}$$

B.4 Incremental Equations of Motion

The governing equations for a rigid body mass are obtained by combining (9) and (30). To express the result in matrix form we introduce the following notation:

$$\begin{aligned}
 \underline{\Delta D}_{k+1}^F &= \begin{bmatrix} \underline{\Delta v}_{k+1}^F \\ \underline{\Delta \Omega}_{k+1}^F \end{bmatrix} & (6 \times 1) \\
 \underline{\Delta R}_{k+1} &= \begin{bmatrix} \underline{\Delta F}_{k+1}^1 \\ \underline{\Delta M}_{k+1}^1 \\ \vdots \\ \underline{\Delta F}_{k+1}^P \\ \underline{\Delta M}_{k+1}^P \end{bmatrix} & (6p \times 1)
 \end{aligned} \tag{32}$$

$$A_k = \begin{bmatrix} mh_1 I & & 0 \\ \hline & h_1 \hat{\alpha}_k + \Delta t_{k+1}^{-1} \hat{\beta}_k & \\ 0 & & +\gamma_k \end{bmatrix} \quad (6 \times 6)$$

$$B_k = \begin{bmatrix} mh_2 I & & 0 \\ \hline & & \\ 0 & & h_2 \hat{\alpha}_k + \Delta t_k^{-1} \hat{\beta}_k \end{bmatrix} \quad (6 \times 6)$$

$$C_k = \begin{bmatrix} mh_3 I & & 0 \\ \hline & & \\ 0 & & h_3 \hat{\alpha}_k \end{bmatrix} \quad (6 \times 6)$$

$$E_k = \begin{bmatrix} I & 0 & I & \dots & I & 0 \\ \hline \alpha_{1/k} & I & \alpha_{2/k} & \dots & \alpha_{p/k} & I \end{bmatrix} \quad (6 \times 6p)$$

With this the equations of motion are

$$A_k \frac{\Delta D^F}{k+1} = B_k \frac{\Delta D^F}{k} - C_k \frac{\Delta D^F}{k-1} + E_k \frac{\Delta R^F}{k+1} \quad (33)$$

Appendix C

Mechanism Stiffness Matrices

C.1 Introduction

The generalized force at a mechanism end attached to the j th node is

$$\underset{\sim}{R}^j = \begin{bmatrix} \underset{\sim}{F}^j \\ \underset{\sim}{M}^j \end{bmatrix} \quad (1)$$

where $\underset{\sim}{F}^j$ is the transmitted force vector and $\underset{\sim}{M}^j$ the transmitted couple. The generalized displacement rate is

$$\underset{\sim}{D}^j = \begin{bmatrix} \dot{\underset{\sim}{U}}^j \\ \dot{\underset{\sim}{\Omega}}^j \end{bmatrix} \quad (2)$$

where $\underset{\sim}{U}^j$ is the nodal displacements and $\underset{\sim}{\Omega}^j$ is the angular velocity of the node. Here we briefly outline the derivation of the incremental mechanism stiffness matrix KE defined by

$$\begin{bmatrix} \dot{\underset{\sim}{R}}^i \\ \dot{\underset{\sim}{R}}^j \end{bmatrix} = KE \begin{bmatrix} \dot{\underset{\sim}{D}}^i \\ \dot{\underset{\sim}{D}}^j \end{bmatrix} \quad (3)$$

C.2 Extensional Spring

At each instant the force transmitted is

$$\underset{\sim}{F}^j = f(s) \underset{\sim}{e}_3 \quad (4)$$

where $\underset{\sim}{e}_3$ is a unit vector directed along the connector axis from the i th to the j th node and s is the current distance between

nodes. The function f is an arbitrary function of s . The unit vector \underline{e}_3 is

$$\underline{e}_3 = (\underline{x}^j - \underline{x}^i)/s \quad (5)$$

where x denotes the nodal coordinates. The sought relation is obtained by differentiating (4) with respect to time. We note that

$$\dot{\underline{e}}_3 = (\dot{\underline{x}}^j - \dot{\underline{x}}^i)/s - \underline{e}_3(s/s) \quad (6)$$

where

$$\dot{s} = \underline{e}^T (\dot{\underline{x}}^j - \dot{\underline{x}}^i) \quad (7)$$

Also we have

$$\dot{\underline{x}}^i = \dot{\underline{U}}^i, \quad \dot{\underline{x}}^j = \dot{\underline{U}}^j \quad (8)$$

Thus differentiating (4) gives

$$\dot{\underline{F}}^j = S (\dot{\underline{U}}^j - \dot{\underline{U}}^i) \quad (9)$$

where S is the 3x3 matrix

$$S = (f/s) I + (f' - f/s) \underline{e}_3 \underline{e}_3^T \quad (10)$$

where f' denotes df/ds and I is the 3x3 identity matrix.

It follows that

$$KE = \begin{bmatrix} S & 0 & -S & 0 \\ 0 & 0 & 0 & 0 \\ -S & 0 & S & 0 \\ 0 & 0 & 0 & 0 \end{bmatrix} \quad (11)$$

C.3 Torsional Spring

A torsional spring transmits a couple directed along the current connector axis. The rate of rotation of node j relative

to node i about the connector axis is

$$\dot{\alpha} = \underline{e}_3^T (\underline{\Omega}^j - \underline{\Omega}^i) \quad (12)$$

where \underline{e}_3 is given by (5).

We define the "angle of twist" at time t as

$$\alpha = \int_0^t \dot{\alpha} dt \quad (13)$$

We assume that

$$\underline{M}^j = T(\alpha) \underline{e}_3 \quad (14)$$

Differentiating (14) and using (6) - (8) gives

$$\dot{\underline{M}}^j = KTW(\underline{\Omega}^j - \underline{\Omega}^i) + KTX(\dot{\underline{U}}^j - \dot{\underline{U}}^i) \quad (15)$$

where

$$KTW = T' \underline{e}_3 \underline{e}_3^T, \quad KTX = (T/s) \mathbf{I} - \underline{e}_3 \underline{e}_3^T \quad (16)$$

in which T' denotes dT/d α .

It follows that

$$KE = \begin{bmatrix} 0 & 0 & 0 & 0 \\ KTX & KTW & -KTX & -KTW \\ 0 & 0 & 0 & 0 \\ -KTX & -KTW & KTX & KTW \end{bmatrix} \quad (17)$$

C.4 Bending Connector

As above \underline{e}_3 denotes a unit vector along the connector axis. For the bending connector we introduce two orthogonal unit vectors in the plane normal to this axis. Their initial orientation is specified. The unit vector \underline{e}_3 changes its orientation due to the relative motion of the nodes at the end points of the

connector. It is assumed that e_1 and e_2 change orientation due to angular velocity about their current position. Thus in vector notation

$$\dot{\underline{e}}_i = \underline{\alpha} \times \underline{e}_i, \quad i = 1, 2, 3 \quad (18)$$

where $\underline{\alpha}$ is the angular velocity vector

$$\underline{\alpha} = \alpha_1 \underline{e}_1 + \alpha_2 \underline{e}_2 \quad (19)$$

It follows that

$$\begin{aligned} \dot{\underline{e}}_1 &= -\alpha_2 \underline{e}_3, & \dot{\underline{e}}_2 &= \alpha_1 \underline{e}_3 \\ \dot{\underline{e}}_3 &= -\alpha_1 \underline{e}_2 + \alpha_2 \underline{e}_1 \end{aligned} \quad (20)$$

From (6), (7) and (20) we have

$$\begin{aligned} \alpha_1 &= -s^{-1} (\dot{\underline{x}}^j - \dot{\underline{x}}^i) \cdot \underline{e}_2 \\ \alpha_2 &= s^{-1} (\dot{\underline{x}}^j - \dot{\underline{x}}^i) \cdot \underline{e}_1 \end{aligned} \quad (21)$$

It is convenient to express these results in a matrix format.

Eqs. (21) may be rewritten as

$$\begin{aligned} \alpha_1 &= -s^{-1} \underline{e}_2^T (\dot{\underline{x}}^j - \dot{\underline{x}}^i) \\ \alpha_2 &= s^{-1} \underline{e}_1^T (\dot{\underline{x}}^j - \dot{\underline{x}}^i) \end{aligned} \quad (22)$$

The bending connector is characterized by bending resistance arising from relative rotation of the nodes about the connector axis. The relative rates of rotation about \underline{e}_1 and \underline{e}_2 are

$$\dot{\theta}_k = \underline{e}_k^T (\underline{\Omega}^j - \underline{\Omega}^i), \quad k = 1, 2 \quad (23)$$

The quantities $\dot{\theta}_k$ can be thought of as the rate of "winding up" a

coil spring about the e_k axis. The total "angle of wind" is

$$\theta_k = \int_0^t \dot{\theta}_k dt \quad (24)$$

The couple transmitted by the bending connector is

$$\tilde{M}^j = M_1(\theta_1) \tilde{e}_1 + M_2(\theta_2) \tilde{e}_2 \quad (25)$$

Differentiating (25) and using (20), (22), (23) gives

$$\begin{aligned} \dot{\tilde{M}}^j &= KBW(\tilde{\Omega}^j - \tilde{\Omega}^i) \\ &+ KBX(\tilde{U}^j - \tilde{U}^i) \end{aligned} \quad (26)$$

where

$$\begin{aligned} KBW &= \sum_{k=1}^2 M'_k \tilde{e}_k \tilde{e}_k^T \\ KBX &= -s^{-1} \tilde{e}_3 \sum_{k=1}^2 M_k \tilde{e}_k^T \end{aligned} \quad (27)$$

in which the prime indicates differentiation with respect to the argument θ_k .

It follows that

$$KE = \begin{bmatrix} 0 & 0 & 0 & 0 \\ KBX & KBW & -KBX & -KBW \\ 0 & 0 & 0 & 0 \\ -KBX & -KBW & KBX & KBW \end{bmatrix} \quad (28)$$

C.5 Shear Connector

For the shear connector unit vectors are introduced in the same manner as the bending connector. The shear connector is characterized by shear resistance arising from the relative

change of orientation of the nodes relative to the connector coordinate frame. Such changes in orientation may arise from both relative displacements of the nodes and the angular velocity of the nodes. In general part of each angular velocity vector is associated with the bending spring response and part with the shear response. The appropriate decomposition is

$$\begin{aligned}\underline{\omega}_B &= \frac{1}{2} (\underline{\Omega}^j - \underline{\Omega}^i) , \\ \underline{\omega}_S &= \frac{1}{2} (\underline{\Omega}^j + \underline{\Omega}^i)\end{aligned}\quad (29)$$

where $\underline{\omega}_B$ and $\underline{\omega}_S$ denote the angular velocity associated with bending and shear respectively. Thus we introduce shear "strain rates" as

$$\begin{aligned}\dot{\gamma}_1 &= \alpha_2 - \frac{1}{2} \underline{e}_2^T (\underline{\Omega}^j + \underline{\Omega}^i) \\ \dot{\gamma}_2 &= \alpha_1 + \frac{1}{2} \underline{e}_1^T (\underline{\Omega}^j + \underline{\Omega}^i)\end{aligned}\quad (30)$$

The accumulated shear strain is

$$\gamma_k = \int_0^t \dot{\gamma}_k dt \quad (31)$$

The force vector transmitted by the shear connector is

$$\underline{F}^j = F_1(\gamma_1) \underline{e}_1 + F_2(\gamma_2) \underline{e}_2 \quad (32)$$

In this case equilibrium requires couples at the nodes in addition to the force requirement $\underline{F}^i = -\underline{F}^j$. The moment equation in vector notation is

$$\underline{M}^i + \underline{M}^j + s \underline{e}_3 \times \underline{F}^j = 0 \quad (33)$$

If s becomes very small, the shear connector (combined with the extensional spring) should reduce to a pin, i.e. $\tilde{M}^i = \tilde{M}^j = 0$. From (33), however, only their sum approaches zero as $s \rightarrow 0$. The difficulty is removed by recognizing that general couples \tilde{M}^i and \tilde{M}^j can be viewed as pure bending and shear; an appropriate decomposition shows that the couples associated with shear satisfy

$$\tilde{M}^i = \tilde{M}^j \quad (34)$$

Thus (33) becomes

$$\tilde{M}^i = \tilde{M}^j = -\frac{1}{2} s (\underline{e}_3 \times \underline{F}^j) \quad (35)$$

Differentiating (32) and (35) and using (20), (22), (30) gives

$$\begin{aligned} \dot{\tilde{F}}^j &= K S X (\dot{\tilde{x}}^j - \dot{\tilde{x}}^i) \\ &\quad + K S W (\dot{\tilde{\Omega}}^j + \dot{\tilde{\Omega}}^i) \\ \dot{\tilde{M}}^j &= K M X (\dot{\tilde{x}}^j - \dot{\tilde{x}}^i) \\ &\quad + K M W (\dot{\tilde{\Omega}}^j + \dot{\tilde{\Omega}}^i) \end{aligned} \quad (36)$$

where

$$\begin{aligned} K S X &= s^{-1} \left[F_1' \underline{e}_1 \underline{e}_1^T + F_2' \underline{e}_2 \underline{e}_2^T \right. \\ &\quad \left. - \underline{e}_3 (F_1 \underline{e}_1^T + F_2 \underline{e}_2^T) \right] \\ K S W &= \frac{1}{2} \left[F_2' \underline{e}_2 \underline{e}_1^T - F_1' \underline{e}_1 \underline{e}_2^T \right] \\ K M X &= \frac{1}{2} \left[(F_1 \underline{e}_2 - F_2 \underline{e}_1) \underline{e}_3^T \right. \\ &\quad \left. + (F_1' \underline{e}_2 + F_2' \underline{e}_3) \underline{e}_1^T - (F_2' \underline{e}_1 + F_1' \underline{e}_3) \underline{e}_2^T \right] \\ K M W &= \frac{1}{4} s (F_1' \underline{e}_2 \underline{e}_2^T + F_2' \underline{e}_1 \underline{e}_1^T) \end{aligned} \quad (37)$$

It follows that

$$KE = \begin{bmatrix} K_{SX} & -K_{SW} & -K_{SX} & -K_{SW} \\ -K_{MX} & K_{MW} & K_{MX} & K_{MW} \\ -K_{SX} & K_{SW} & K_{SX} & K_{SW} \\ -K_{MX} & K_{MW} & K_{MX} & K_{MW} \end{bmatrix}$$

C.6 Connection to Rigid Body Nodes

If the connector is attached to a rigid body node, Eq. (3) must be modified. Rigid body nodes do not have independent degrees of freedom. Thus the kinematic variables on the right hand side of (3) must be expressed in terms of the rigid body variables by an appropriate transformation. In rate form we have

$$\dot{\tilde{U}}^j = \dot{\tilde{U}}^R - \alpha_{j/k} \tilde{\Omega}^R \quad (39)$$

where the superscript R denotes quantities associated with the rigid body center of gravity and

$$\alpha_{j/k} = L^T C_{j/k} L \quad (40)$$

in which L is the direction cosine matrix of the rigid body coordinates with respect to the global coordinates and

$$C_{j/k} = \begin{bmatrix} 0 & -Z_{j/k} & Y_{j/k} \\ Z_{j/k} & 0 & -X_{j/k} \\ -Y_{j/k} & X_{j/k} & 0 \end{bmatrix} \quad (41)$$

In (41) the elements are the coordinates of the jth rigid body node with respect to the rigid body coordinate frame.

It follows that

$$\dot{\underline{D}}^j = T \dot{\underline{D}}^R \quad (42)$$

where T is the 6 x 6 transformation matrix

$$T = \begin{bmatrix} I & -\alpha_{j/k} \\ 0 & I \end{bmatrix} \quad (43)$$

C.7 Superposition of Mechanisms

Above we have derived incremental stiffness matrices for four types of mechanisms. It should be noted that in incremental form the generalized force rate is linearly related to the generalized displacement rate. Thus a mechanism which transmits a general force and couple may be obtained by superposition of the above four mechanisms. It follows that the force-deformation characteristics of this general mechanism are specified by the six arbitrary functions

$$\begin{aligned} f &= f(s) \\ F_k &= F_k(\gamma_k) \quad k = 1, 2 \\ T &= T(\alpha) \\ M_k &= M_k(\theta_k) \quad k = 1, 2 \end{aligned} \quad (44)$$

where s is the current distance between nodes, γ_k is defined by (31), α is defined by (13), and θ_k is defined by (24).

Appendix D

Plastic Hinge Tests

D.1 Experimental Hinge Tests

An experimental program was designed to study the behavior of plastic hinges subjected to large rotations. In addition to developing a test methodology, the program obtained the necessary hinge data for the static and dynamic validation tests discussed earlier. The necessary data is defined by the constitutive theory proposed in Appendix A. We briefly summarize the pertinent equations. Detailed discussion is given in Appendix A.

We assume the behavior of the hinge is determined by a scalar generalized yield function

$$f(\underline{\xi}) = 1 \quad (1)$$

where

$$\xi_j = Y_j / \alpha_j \quad j = 1, 2, 3, 4 \quad (2)$$

in which the four elements of \underline{Y} denote the current values of the axial force, bending moments about the principal axes, and torque respectively. (For convenience the dependence of f on transverse shear is neglected). Thus, the components of $\underline{\xi}$ are normalized stress resultants in local beam coordinates. The scaling parameters α_j are considered as constitutive properties of the hinge whose value depends upon the history of plastic deformation. In particular we assume

$$\alpha_j = \alpha_j (\theta_j) \quad j = 1, 2, 3, 4 \quad (3)$$

where the scalars θ_j denote the accumulated plastic deformation in extension, biaxial bending, and torsion respectively. Precise definitions of θ_j are given in Appendix A.

The experimental task is thus to determine the parameters α_j . With the assumption embodied in (3), it is sufficient to conduct tests in extension, pure bending, and torsion. A number of factors must be considered in the design of the experiments. These include:

1. The beam cross section must be supported at points of loading and reaction to prevent local crushing due to extraneous stress concentrations.
2. The test must be displacement controlled so that the specimen does not collapse in the "softening" region of the load-displacement curve.

3. The loading fixture must apply a constant direction load over the entire large deformation range.
4. Specimens must be designed to insure a gage length which is characteristic of hinge formation. Preliminary tests in unconstrained specimens suggest that twice the beam thickness is an appropriate characteristic length.

All tests were done using displacement controlled, static test machines. The torsion and tensile specimens required no special treatment or unusual fixtures. The experimental problem of maintaining a pure bending moment on a specimen throughout a large deformation test is more difficult. The specimen is mounted between two rigid end blocks which are attached to a four point support fixture creating a pure couple about an axis in the specimen.* Care must be taken to insure the hinge forms in the center of the specimen to maintain the necessary symmetry.

All specimens were 1 inch square tubing with 0.075 inch walls. The material was low carbon, automotive grade steel, 1040. Overall specimen lengths varied in each test, but in every case internal "plugs" were used to support the cross section at points of loading. These plugs extended to the hinge site, leaving only a 2 inch gage length free to deform. For the bending test the plugs were contoured at the hinge location to provide a gradual transition from full to no wall support. Without this precaution the hinge is likely

* A more detailed discussion of the pure bending test is given in Vol. 2.

form near the plug end. The torsion and tension specimens employed a rounded end insert more appropriate to a hinge with an axis of symmetry along the longitudinal axis.

D.2 Test Results

The tensile test of the tube is shown in Fig. D.1 in the form of a stress-strain diagram. Strain is measured over a two inch gage length in the unsupported wall region of the test specimen. Although the test is essentially a uniaxial stress-strain test, the choice of gage length permits the results

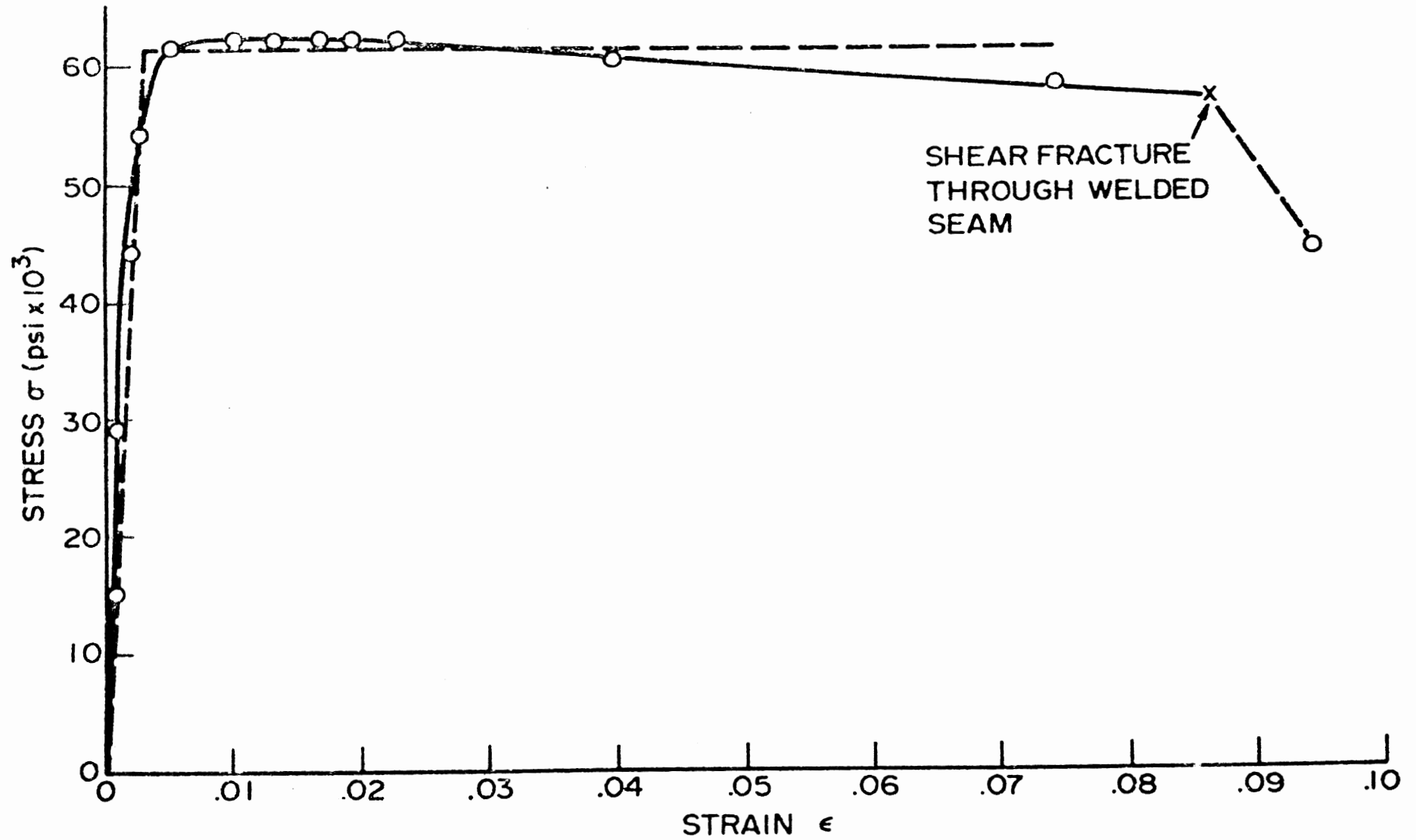


FIG. D.1 TENSILE TEST FOR
1" x 1" x 0.075" TUBING

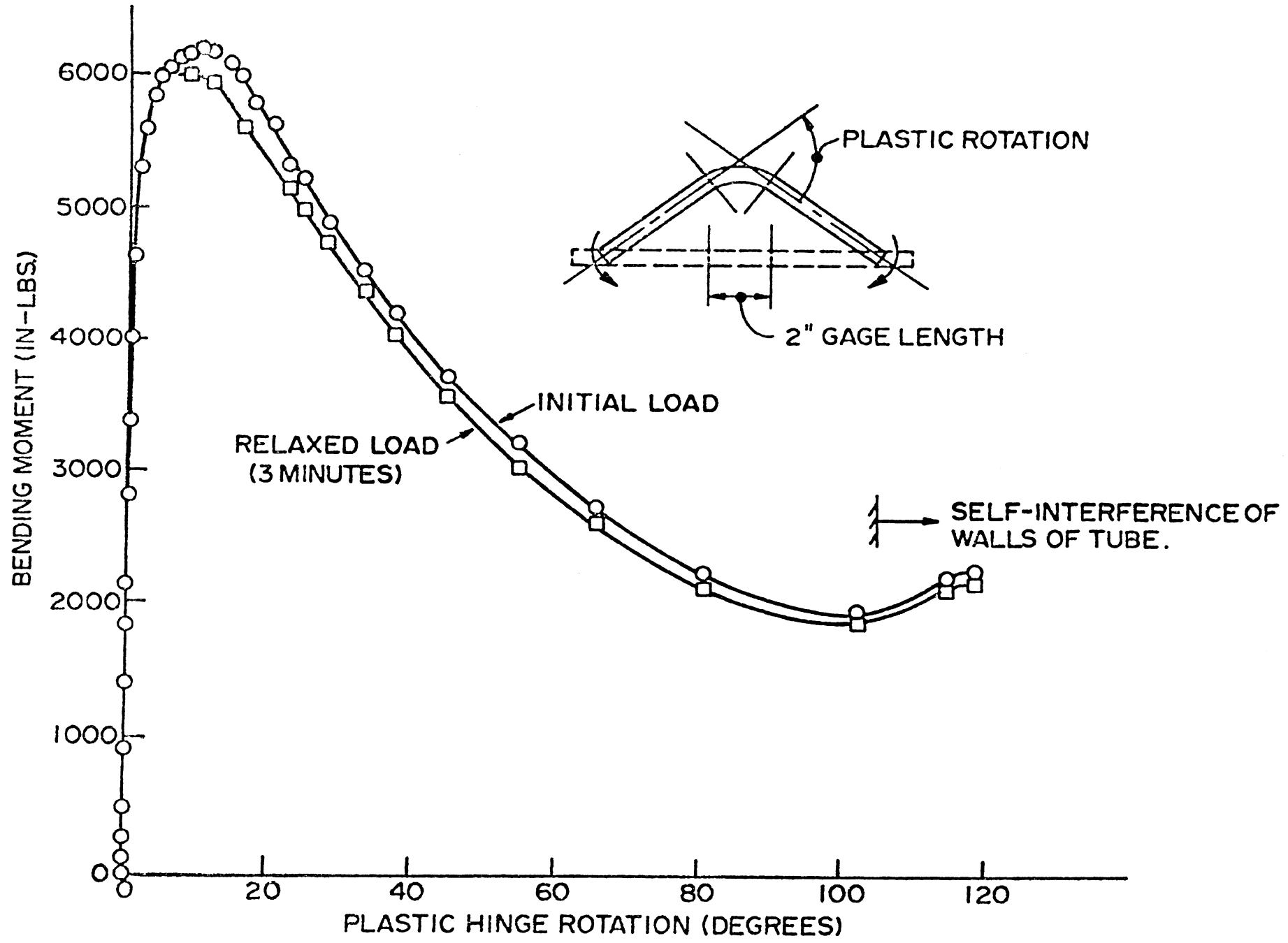


FIG. D.2 PLASTIC HINGE ROTATION-
PURE BENDING

to be interpreted as a hinge test for the axial stress resultant. The results can be modeled rather well as elastic-perfectly plastic with a yield stress of 61,500 psi. Although for small strains (below 5×10^{-4}), the slope of the elastic curve is nearly 30×10^6 psi, a better fit of the data over the assumed linear range is a Young's Modulus of 20×10^6 psi. The elastic-perfectly plastic approximation is shown by dashed lines in the Figure. At large strains (above 0.04) a waviness in the wall surface occurred. The tube failed by a shear fracture through the welded seam.

Results for the pure bending test are given in Fig.D.2. The welded seam was located on the compressive side. Elastic action of the support and specimen has been numerically removed from the data. Thus the abscissa denotes plastic hinge rotation over the gage length. A stress relaxation phenomenon was observed at constant displacement. Separate curves are given for "instantaneous" bending moment at time of incremental loading and bending moment after 3 minutes relaxation. The latter curve can be taken as a close approximation to static values.

In contrast to the axial test, the reduction in the moment carrying capacity of the hinge with increasing rotation is dramatic. The associated development of the local deformation during hinge formation is shown in Fig. D.3. This curve may be of some value for future detailed analysis of the hinge site.

Results for a pure torsion hinge are shown in Fig. D.4. Again, the elastic rotation has been removed from the data so that only plastic rotation over the 2 inch gage length is given. The hinge in this case is a spiral pattern with pronounced folding of the walls into the star pattern shown. As in the bending test a load relaxation is observed.

The torsion test could be run to very large rotations. In tests of unconfined specimens, yielding occurs over the entire unsupported length. Once the hinge forms, however, it is confined to a relatively short length on the order of the dimensions of the cross section. To eliminate the effect of overall yielding from the hinge data, inserts were used to confine the gage length to the characteristic length observed in unsupported specimens.

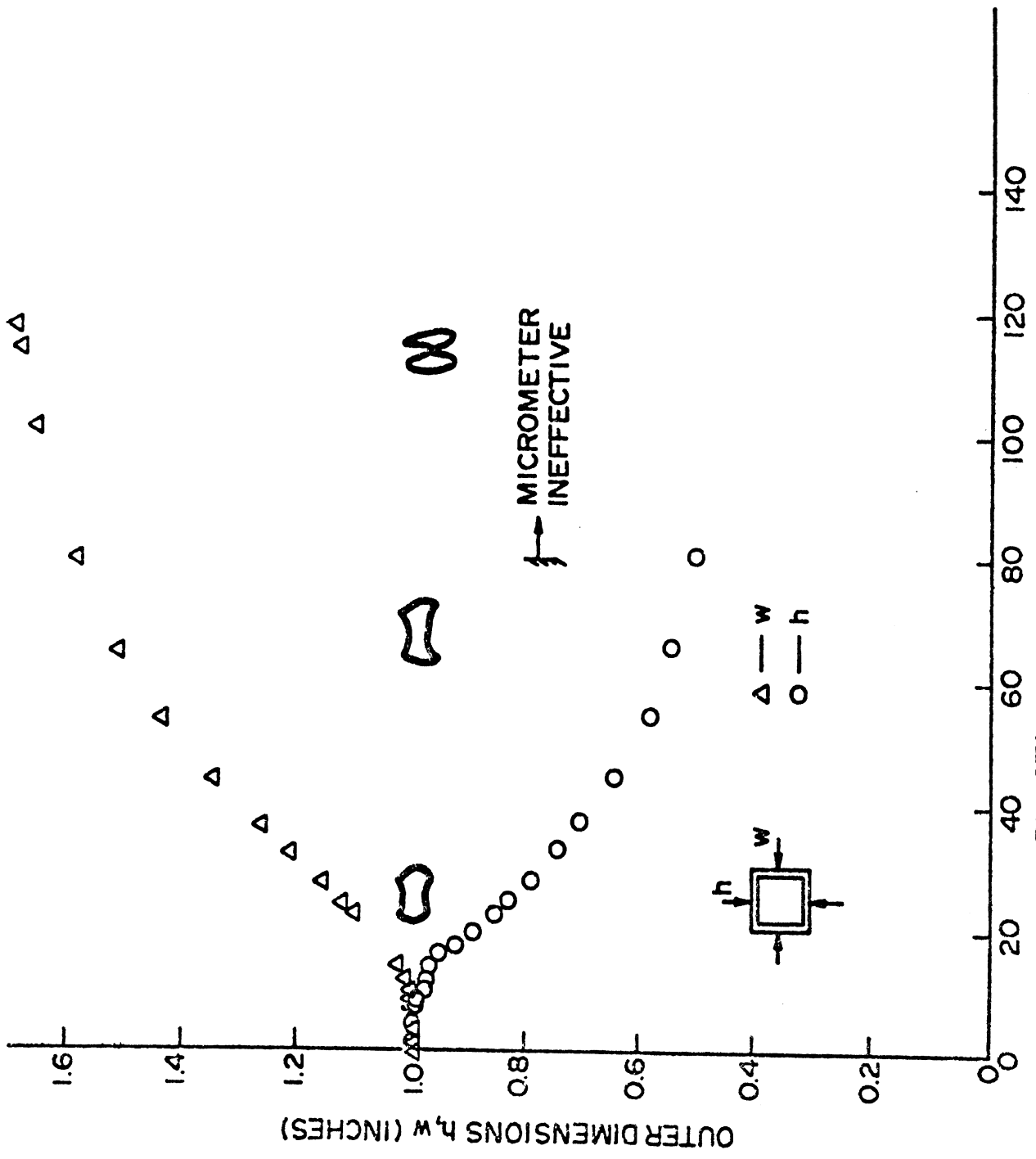


FIG. D.3 HINGE DEFORMATION - PURE BENDING

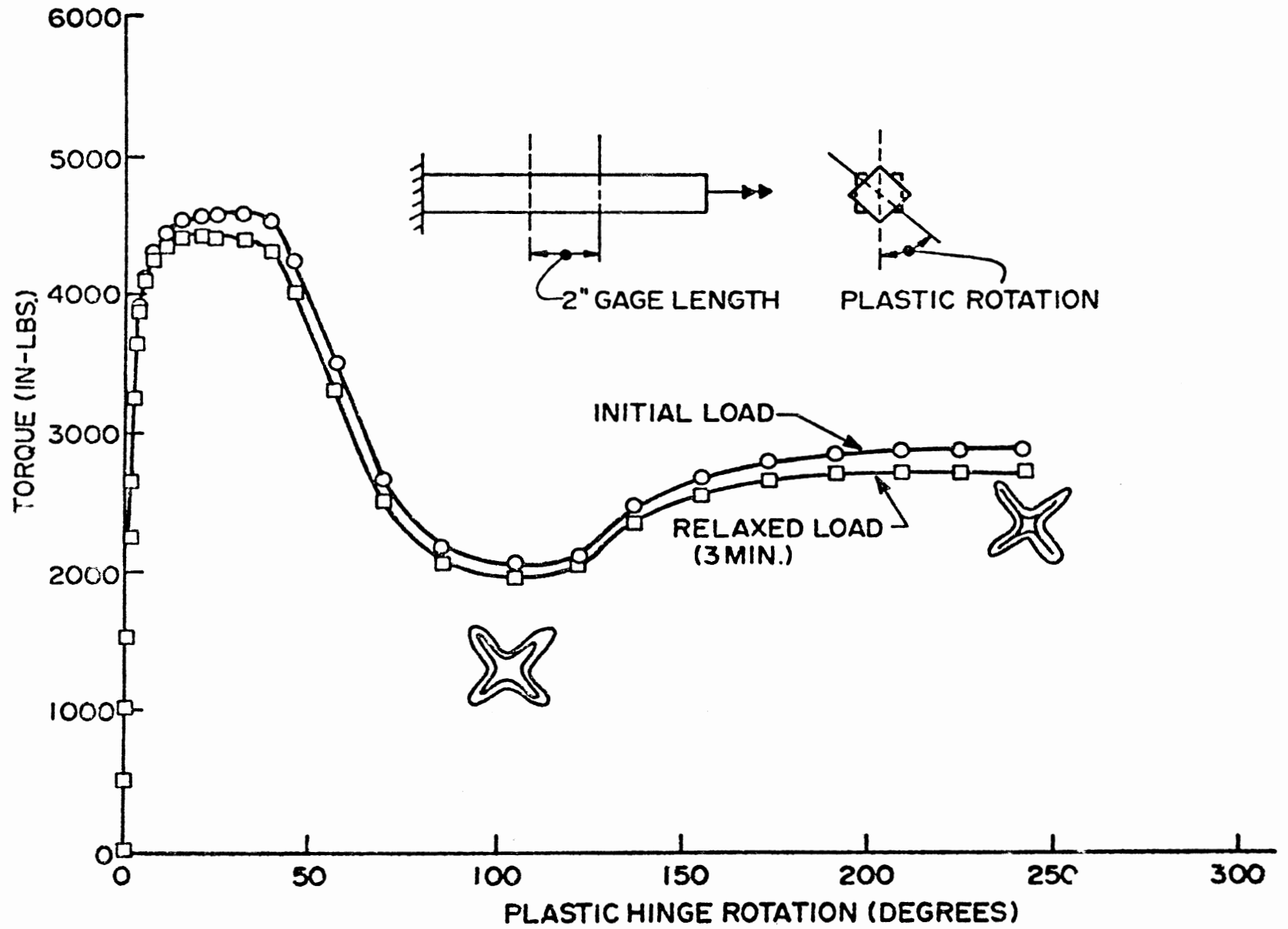


FIG. D.4 PLASTIC HINGE ROTATION-TORSION

D.3 Hinge Constitutive Parameters

To use the above data to determine the constitutive parameters α_j , it is necessary to specify the yield function f . In the present study we choose f as the hyper-ellipse

$$f = \sum_{j=1}^4 \xi_j^2 = 1 \quad (4)$$

With (4) and (3) it follows that the dependence of α_j on the plastic deformation measures are given directly by the above test results.

It remains to fit the data in a form convenient for computational purposes. The characteristic shape observed in the bending and torsion tests can be approximated by an exponential function of the form

$$\alpha = M \left\{ a_i + b_i \left[1 + k_i(\theta - \theta_m) \right] \exp \left[-k_i(\theta - \theta_m) \right] \right\} \quad (5)$$

where θ is the accumulated plastic rotation and θ_m is the value of θ corresponding to the maximum value of α . For $\theta < \theta_m$, $i = 1$ and

$$\begin{aligned} a_1 &= (1 - fy) / (1 - y) \\ b_1 &= (f - 1) / (1 - y) \end{aligned} \quad (6)$$

$$y = (1 - k_1 \theta_m) \exp (k_1 \theta_m) \quad (7)$$

For $\theta > \theta_m$, $i = 2$ and

$$a_2 = \beta \quad , \quad b_2 = f - \beta \quad (8)$$

Equation (5) is a function of six parameters which may be used to fit the test results. Four of the parameters have simple physical interpretations and may essentially be determined by inspection; they are

M = maximum elastic moment

f = ratio of maximum value of α to M

β = ratio of the asymptotic value of α
for large θ to M

θ_m = value of θ at maximum value of α .

The remaining two parameters may be considered as hardening and softening rates for the cross section. They may be obtained by minimizing the error between (6) and the test results in the two ranges $\theta < \theta_m$, $\theta > \theta_m$.

As shown in Fig. D.1 the plastic behavior in axial extension may be modeled as perfectly plastic with a yield stress σ_y of 61,500 psi. Thus the parameter α_1 is a constant which is obtained from (5) by setting

$$M = A\sigma_y, \quad \theta_m = 0, \quad f = \beta = 1 \quad (9)$$

where A is the area of the cross section.

HINGE PARAMETERS	EXTENSION α_1	BENDING α_2, α_3	TORSION α_4
M	17,000 lbs.	4,500 in-lbs.	3,500 in-lbs.
f	1	1.34	1.27
β	1	0.40	0.54
θ_m	0	0.073	0.244
k_1	-	31.9	43.1
k_2	-	6.20	7.13

TABLE D.1 HINGE PARAMETERS FOR SQUARE TUBING

The specific numerical values obtained for the tubular beam specimen tested here are summarized in Table D.1. The data shown is for a fit to the static (relaxed) curves in Figures D.2 and D.4. Comparison between the test results and computed values using equation (5) is shown in Fig. D.5 for bending and Fig. D.6 for torsion.

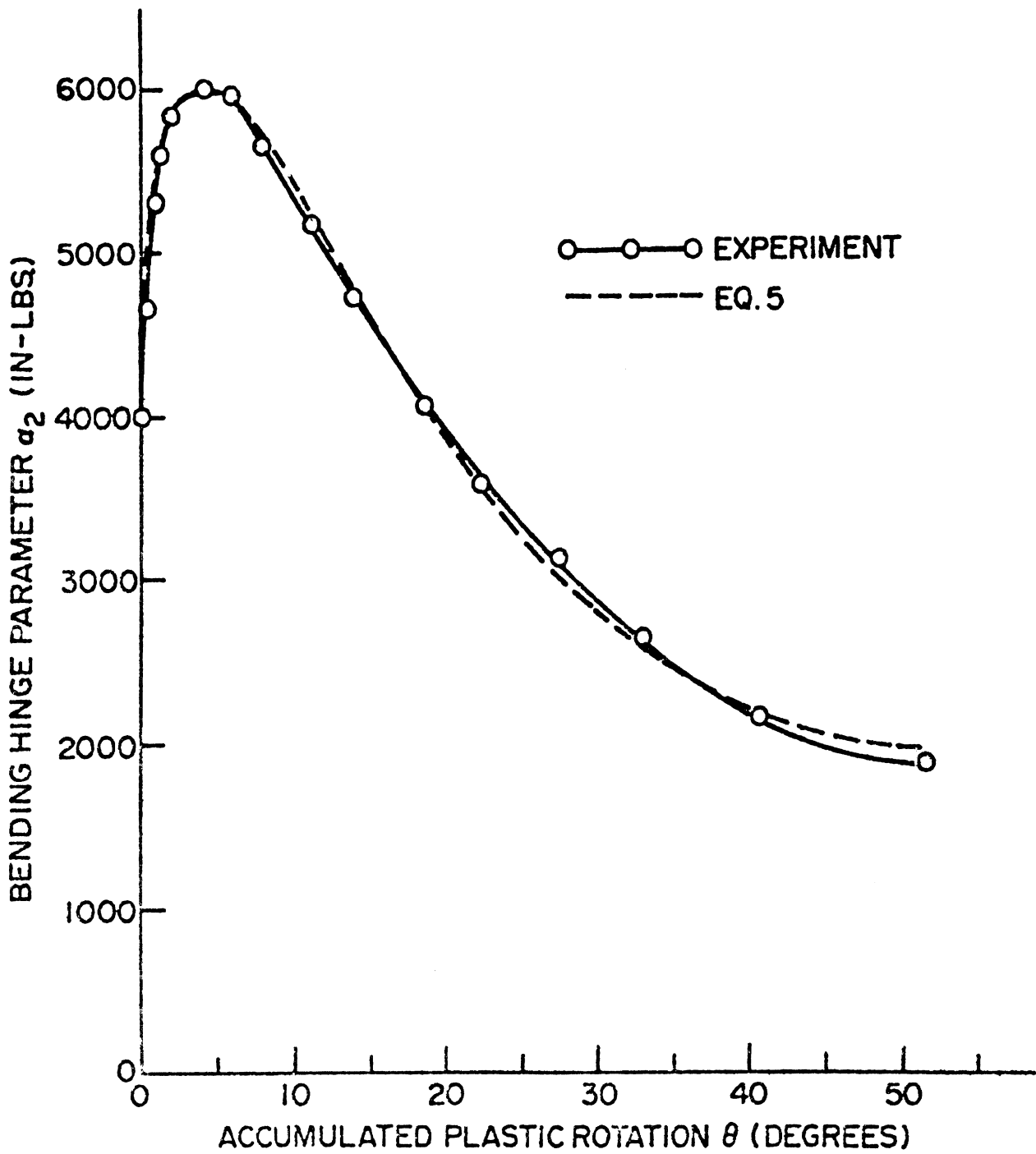


FIG. D.5 COMPUTED AND EXPERIMENTAL PLASTIC HINGE ROTATION IN BENDING

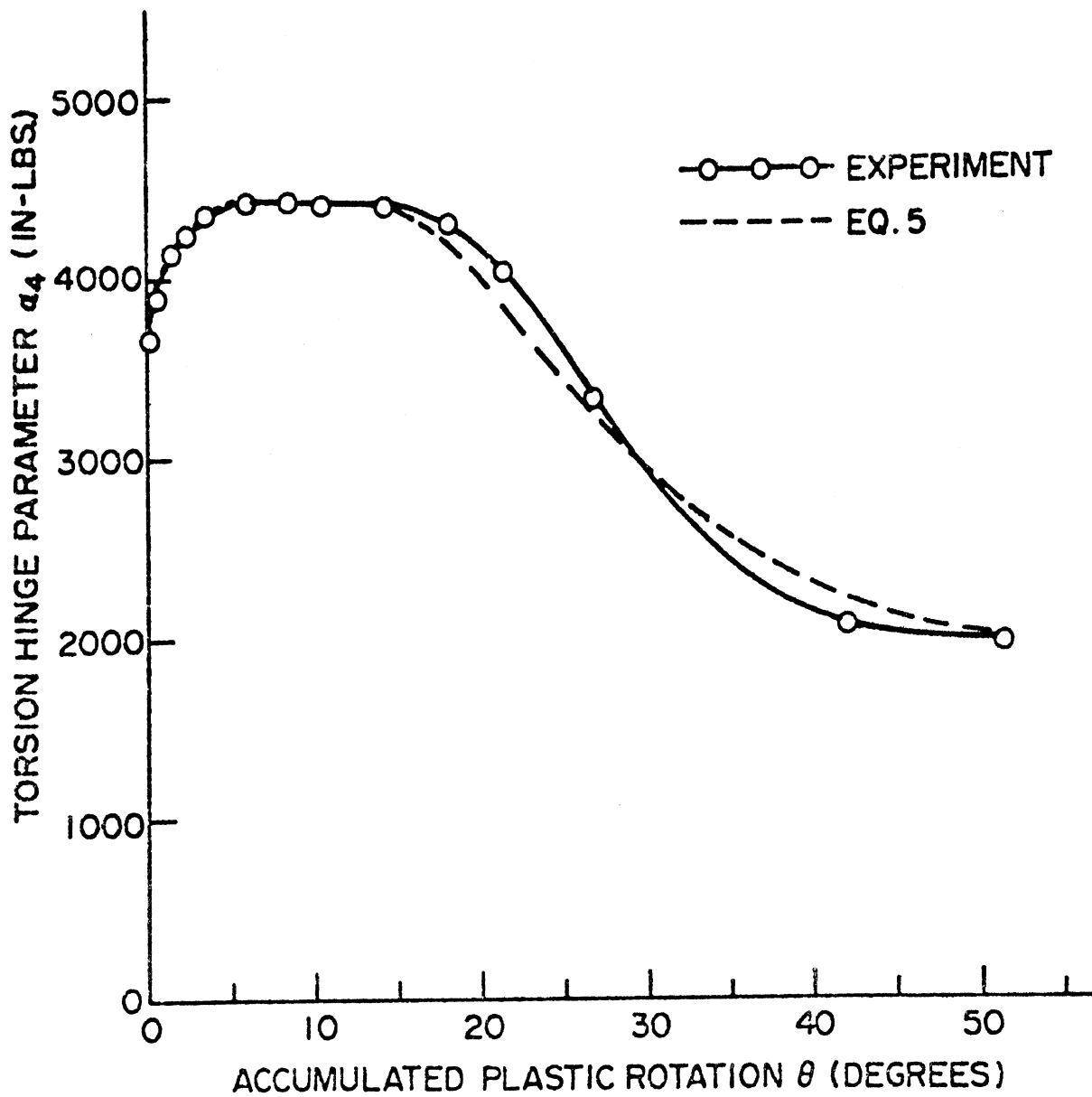


FIG. D.6 COMPUTED AND EXPERIMENTAL
PLASTIC HINGE ROTATION
IN TORSION